ICE IN SPACE:
AN EXPERIMENTAL AND
THEORETICAL INVESTIGATION

NASA Contract NAS8-30566

INTERIM REPORT
MR 8 '78

ICE IN SPACE:

AN EXPERIMENTAL AND THEORETICAL INVESTIGATION

Prepared for

George C. Marshall Space Flight Center

By:

Harvey Patashnick,   George Rupprecht,
Research Associate   Consultant
Dudley Observatory   7150 E. Berry Avenue
Albany, New York 12205   Englewood, Colorado 80110

Approved By:

Curtis L. Hemenway, Director
Dudley Observatory

FOREWORD

This report was prepared by Dudley Observatory
under contract NAS8-30566, "Ice Particle Sublimation in Space",
for the George C. Marshall Space Flight Center of the National
Aeronautics and Space Administration under the technical cognizance
of Dr. Nicholas C. Costes of the Space Sciences Laboratory of MSFC.

CONTENTS

CONTENTS (Continued)

1.   SCOPE

1.1 _Purpose_ - The behavior of ice and ice particles in space
is of considerable astrophysical interest. There are many places where
ice is believed to exist in the universe. It is thought that ice exists
on circumstellar grains (Ref. 1), interstellar grains and the particles
in the rings of Saturn, but the most prominent example is probably that of
comets. The hypothesis of the existence of ice in comets is attributed to
Whipple (Ref. 2) in his well known icy conglomerate model. Further
experimental and theoretical work has been pursued by Delsemme (Ref. 3) who
has indicated that water ice controls the vaporization rate of comets and
has developed a mechanism by introducing clathrates which presumably
results in the ejection of ice grains into the coma of comets.

It is the purpose of this report to provide basic knowledge on the
behavior of ice and ice particles under a wide variety of conditions
including those of interplanetary space. This information and, in
particular, the lifetime of ice particles as a function of solar distance
is an absolute requirement for a proper interpretation of photometric
profiles in comets. Because fundamental properties of ice and ice particles
are developed in this report, the applicability of this information extends
beyond the realm of comets into any area where volatile particles exist,
be it in space or in the earth's atmosphere.

1.2 _Scope_ - The present investigation is centered around the
sublimation of ice and how this sublimation depends upon the surface

temperature, the radiation field, the complex index of refraction, and the size of ice particles. An internal energy source for comets is proposed and low temperature, low pressure depositions were conducted in an initial investigation to demonstrate the possible role of amorphous ice as the energy source for comet activity. Theoretical as well as experimental investigations have been pursued and the results have been applied to a number of situations of fundamental interest both in space and in the atmosphere.

1.3 <u>Summary</u> - A) The sublimation rate of ice in a non-equilibrium situation cannot be described in terms of simple kinetic theory for all temperatures. The actual sublimation rate as a function of surface temperature has never been successfully explored over the total temperature range. In this study a complete experimental determination has been conducted which shows close agreement with calculations based on simple kinetic theory at low temperatures and increasing deviations at higher temperatures resulting in a reduction of almost two orders of magnitude close to the melting point of ice (Ref. 4). This result enhances the possibility of liquid water occurring on comets at greater distances from the sun than previously expected.

B) As a consequence of the interaction between the radiation field and the size dependent absorption and emission properties of ice particles, a size dependence of the sublimation rate results. A sublimation minimum was found at a particular particle size independent of solar

distance (Ref. 5). The position of the minimum in respect to particle size depends upon the spectral distribution of the radiation field and the effective complex index of refraction which is impurity dependent. The magnitude of the sublimation rate as a function of particle size and the sharpness of the sublimation rate minimum depends upon the solar distance and the impurity concentration. Through the use of this information, the life history of a particle or a particle distribution can be determined (Ref. 6).

C)   A mechanism using the properties of amorphous ice is suggested which explains comet outbursts and may also be influential in the ejection of ice particles by the comet nucleus (Ref. 7). Depositions of water ice and water ice with ammonia were conducted at low temperature and pressure and have demonstrated a clear energy release upon warming.

D)   Utilizing the physical insight on the behavior of ice particles in space, which resulted from this work, an application to the behavior of cirrus ice particles has been pursued (Ref. 8). One of the keys in the understanding of long-lived cirrus ice particles is the evaporation coefficient which was studied under this contract for pure ice. The modification of this quantity by artifical means may have significant potential for weather modification.

2.   APPLICABLE DOCUMENTS

The present contract is a further development of research which was initiated under Contract NAS8-24000. Therefore a great deal of

background information is contained in the Technical Report ED-2002-
1654 of March 30, 1973 under the title "Sublimation of Ice Particles in
Space" (Ref. 9). Information contained in this previous report will only
be repeated in abreviated form to the extend that the present report
becomes self contained and intelligible to the reader. For a description
of operations, procedures, experimental techniques and a detailed
description of the instrumentation, the reader is referred to the above
mentioned report.

3. TECHNICAL DISCUSSION

3.1 Theory - In this report, ice particles of various sizes are
studied at different locations within the solar system. Only two energy
exchange mechanisms are considered, the radiative energy transfer and
the energy dissipation through sublimation. Therefore, the energy balance
can be described in the form:

$$P_s + P_a + P_r + P_{st} = 0 \tag{1}$$

with the convention that power delivered to the particle is positive.
In equation (1) P_s is the power lost by sublimation ($P_s < 0$), P_a pertains
to the power absorbed by the particle from the radiation field ($P_a > 0$).
P_r is the power radiated ($P_r < 0$), and P_{st} is the power stored in the
particle. In a quasi-steady state condition, P_{st} can be neglected.
Specifically

$$P_s = -HA\phi \tag{2}$$

where H is the heat of sublimation for ice, A is the surface area of

the ice particle and $\dot{\phi}$ is the sublimation rate which in turn can be expressed in the form:

$$\dot{\phi} = \lambda(T_s) \, \dot{\phi}_{th}(T_s) \qquad (3)$$

The evaporation coefficient, $\lambda(T_s)$, has been investigated in the course of this work and will be discussed later. $\dot{\phi}_{th}(T_s)$ is the theoretical sublimation rate defined as:

$$\dot{\phi}_{th}(T_s) = P(T_s) \, (\frac{m}{2\pi kT_s})^{\frac{1}{2}} \qquad (4)$$

where $P(T_s)$ is the equilibrium vapor pressure at the surface temperature T_s, m is the mass of a water molecule and k is the Boltzmann constant.

Under the influence of solar radiation with the spectral distribution $S(\lambda)$ and, for simplicity's sake, an additional uniform black body radiation $F(\lambda, T_w)$ characterized by the temperature of the surroundings T_w, the absorbed power, P_a, for a spherical ice particle at the solar distance R in A. U. becomes

$$P_a = A \int_0^\infty \left[S(\lambda)/4R^2 + F(\lambda, T_w) \right] Q(\lambda, r, n^*) \, d\lambda . \qquad (5)$$

Q represents the absorption efficiency at wavelength λ for a particle of radius, r, and complex index of refraction, n*. When the surface temperature of the particle is T_s, one can write the radiated power, P_r, as

$$P_r = -A \int_0^\infty F(\lambda, T_s) Q(\lambda, r, n^*) \, d\lambda. \qquad (6)$$

Accordingly, equation (1) can be written in the form

$$H \alpha(T_s) \, P(T_s) \, (\frac{m}{2\pi kT_s})^{\frac{1}{2}} = \int_0^\infty \left[\frac{S(\lambda)}{4R^2} + F(\lambda, T_w) - F(\lambda, T_s) \right] Q(\lambda, r, n^*) \, d\lambda . \qquad (7)$$

Since $\alpha(T_s)$ is known from experiment (see 3.2.3.1), and since $Q(\lambda, r, n^*)$ can be obtained by using scattering theory with the appropriate optical properties, equation (7) can be viewed as an equation for the determination

of the surface temperature, T_s.

It is obvious from equation (7) that the surface temperature is a function of the solar distance, R, the radius of the particle, r, and its complex index of refraction, n*:

$$T_s = T_s (R,r,n*). \qquad (8)$$

Consequently, according to equation (3), the sublimation rate, ϕ, is also a function of the parameters R, r, and n*:

$$\phi = \phi (R,r,n*). \qquad (9)$$

3.2 **Experiments** - The essence of the present work is wrapped up in the formulation represented by equations (8) and (9). They show clearly the critical parameters which determine the sublimation rate of ice particles in space, namely the distance from the sun, the particle radius and the complex index of refraction. In the previous section the basic theory has been presented, but how well does this mathematical development apply to real particles?

While theoretical results are generated by a computer, the applicability of the theory to the real world can only be tested by measurements under carefully controlled conditions. These measurements have been carried out with the unique instrumentation described below.

3.2.1 **Instrumentation** - In order to study the behavior of ice particles in a space environment one must develop instrumentation capable of space simulation and sublimation rate measurements. While a high sensitivity for the measurements is required, a minimum of interference of the equipment with the energy balance of a particle with its surroundings should be achieved.

3.2.1.1 <u>General Description of the Mechanical Configuration of the Measuring Apparatus</u> - Sublimation rate measurements on individual ice particles were conducted using an oscillating fiber microbalance (Ref. 10). A thorough description is given in the report referenced in Section 2, therefore only a brief description will be given here. Mass changes on ice spheres, which are suspended at the end of a thin quartz fiber, are detected by monitoring the mechanical oscillations of the loaded fiber. This oscillating system is mounted inside a temperature controlled copper cylinder which in turn is located in a vacuum chamber. Vacuum windows provide for optical access to the sample including the ability to provide for solar simulation by an external 1 kilowatt xenon arc lamp. The intensity of the adiation at the sample can be varied by adjusting the distance between the lamp and the sample. The vacuum system provides a vacuum better than 10^{-5} torr; therefore, heat transfer by gas conduction is negligible.

3.2.1.2 <u>Electronic Configuration</u> - The fiber is maintained in oscillation by a photo-optical feedback system which optically detects the oscillation of the fiber through the use of a magnified shadow of the fiber on a phototransistor. The signal from the phototransistor is amplified and returned to a gold coating on the fiber. A mechanical force is exerted on the fiber through the interaction of the oscillating charge on the gold coating with an electrostatic field. A period-averaging frequency counter measures the oscillation frequency and is coupled through an interface to a paper tape punch which provides a record of the time dependence of the

fiber frequency which is then ready for data reduction by a computer.

3.2.1.3 <u>Solar Simulation Calibration</u> - Since the sublimation rate depends upon both the spectral absorption properties of the particle and the spectral distribution of the radiation field, the xenon arc lamp which was used for solar simulation purposes had to be calibrated carefully. The spectral distribution curves supplied by the manufacturer are not sufficient because the emphasis is mainly with the radiation from the arc. For this particular experiment, however, no imaging of the arc was employed and consequently radiation from the electrodes and the quartz envelope of the lamp also contribute to the radiation field at the sample. This extra radiation becomes significant because of the strong absorption of ice in the infrared. In order to obtain a viable comparison between theory and experiment with this lamp a careful calibration had to be carried out. The xenon arc lamp does not represent a good simulation of the energy spectrum of the sun. Consequently the sublimation rates obtained with the use of this lamp cannot be directly applied to the sublimation rate of a particle under solar radiation. However, since the theoretical calculations can take into account any spectral distribution, an agreement between theory and experiment in the case of the xenon lamp radiation indicates that reliable results can also be expected with computations involving a solar spectral distribution.

The simulation lamp is a one kilowatt Hanovia xenon arc lamp operating at 42 amp. in a water and air-cooled housing. The calibration was accomplished through the use of wide band glass filters and interference

filters. A radiometer manufactured and calibrated by the Eppley Corporation was placed at the sample location. The radiometer is exceptionally linear over a wide range of photon fluxes. Ratios of fluxes with and without filters were measured. The transmission characteristics of the interference filters were measured with infrared spectrometers. With the use of this information, the energy spectrum of the xenon arc lamp at the location of the sample was calculated. It should be mentioned that the light from the xenon arc lamp passes through a crystalline quartz plate and an ultraviolet grade sapphire vacuum window. Thus the results which are shown in Table 1 represents the fraction of the total power per wavelength interval $(0.1 \mu m)$ at the sample. Also shown are the fractions of solar flux per wavelength interval. The relation between the solar flux and the flux from the xenon arc lamp is demonstrated by their ratio also shown in the Table and in Figure 1. For simplicity the solar flux is approximated by a black body radiation of $5900^{\circ}K$.

3.2.2 Experimental Approach - In an effort to develop a model which describes the sublimation properties of ice particles in the solar system, several parameters which cannot be obtained theoretically must be explored by experiment. For the purposes of this study water ice has been selected for experimental exploration. This is due to a number of reasons. First, there are strong indications that water ice exists in space and is a major component of comets. Secondly, the optical and physical properties of water ice are well known. Although aspects of the present study can be extended to other ices, the relatively low vapor pressure of water ice

TABLE 1

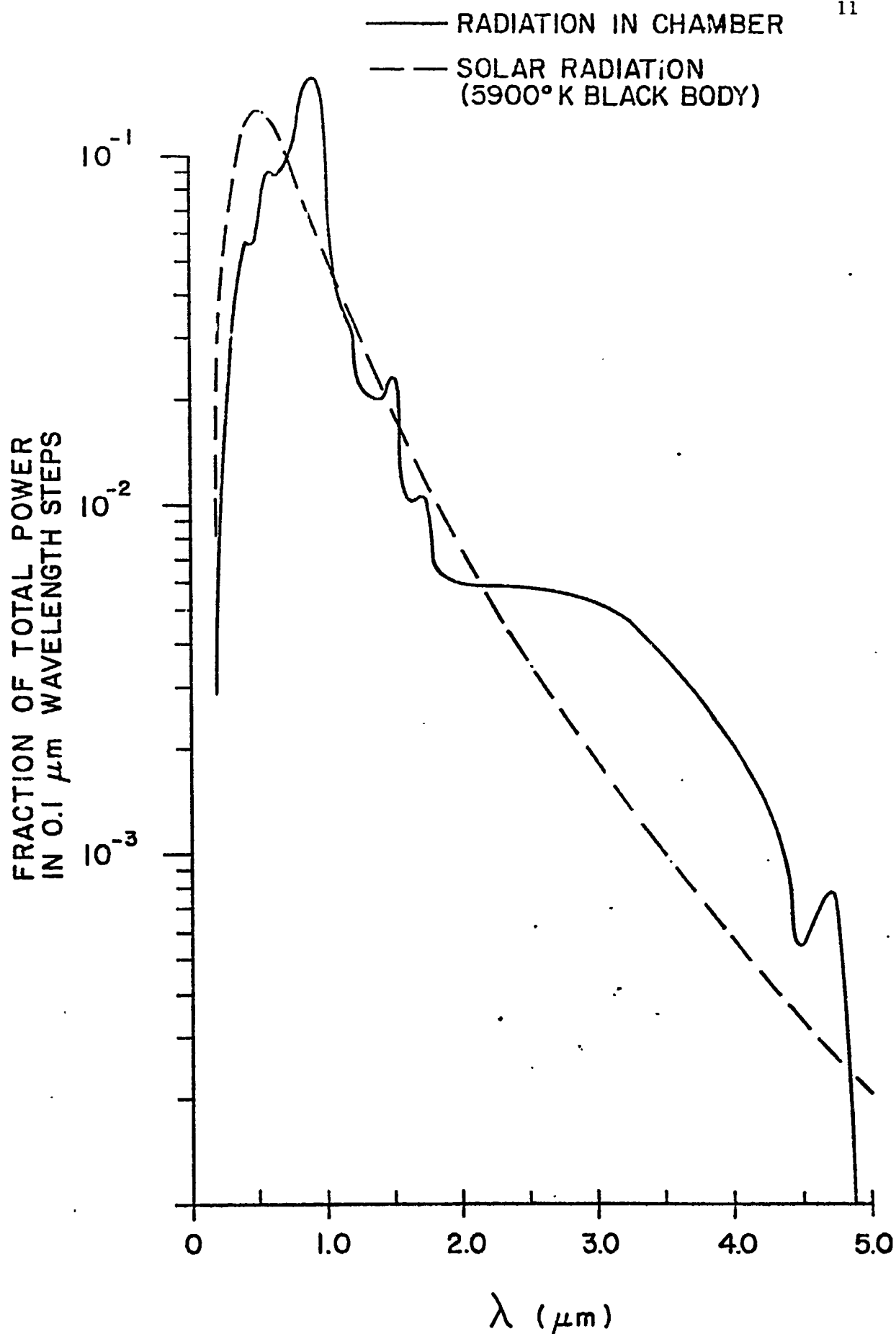| (μm)	Xenon Arc Lamp Flux $\dfrac{\text{P in } 0.1\,\mu\text{m interval}}{\text{P total}}$	Solar Flux (5900°K black body) $\dfrac{\text{P in } 0.1\,\mu\text{m interval}}{\text{P total}}$	$\dfrac{\text{Xenon Arc Lamp Flux}}{\text{Solar Flux}}$
0.2	0.0029	0.00868	0.334
0.3	0.0263	0.0666	0.395
0.4	0.0566	0.121	0.468
0.5	0.0663	0.135	0.491
0.6	0.0898	0.123	0.730
0.7	0.0946	0.103	0.918
0.8	0.139	0.0833	1.66
0.9	0.155	0.0662	2.34
1.0	0.0995	0.0524	1.90
1.1	0.0400	0.0416	0.962
1.2	0.0295	0.0332	0.889
1.3	0.0206	0.0267	0.772
1.4	0.0202	0.0217	0.931
1.5	0.0230	0.0177	1.30
1.6	0.0106	0.0146	0.726
1.7	0.0107	0.0121	0.884
1.8	0.0066	0.0101	0.653
1.9	0.0062	0.0085	0.729
2.0	0.0060	0.0073	0.822
2.1	0.0059	0.0061	0.967
2.2	0.0059	0.0052	1.14
2.3	0.0057	0.0045	1.27
2.4	0.0057	0.0039	1.46
2.5	0.0057	0.0034	1.68
2.6	0.0056	0.0030	1.87
2.7	0.0055	0.0026	2.12
2.8	0.0054	0.0023	2.35
2.9	0.0054	0.0020	2.70
3.0	0.0052	0.0018	2.89
3.1	0.0051	0.0016	3.2
3.2	0.0047	0.0014	3.4
3.3	0.0043	0.0013	3.3
3.4	0.0040	0.0012	3.3
3.5	0.0036	0.0011	3.3
3.6	0.0033	0.0009	3.7
3.7	0.0029	0.0009	3.2
3.8	0.0026	0.0008	3.3
3.9	0.0023	0.0007	3.3
4.0	0.0020	0.0006	3.3
4.1	0.0018	0.0006	3.0
4.2	0.0015	0.0005	3.0
4.3	0.0012	0.0005	2.4
4.4	0.00086	0.0004	2.2
4.5	0.00055	0.0004	1.4
4.6	0.00066	0.0003	2.2
4.7	0.00078	0.0003	2.6
4.8	0.00042	0.0002	2.1
4.9	0.00006	0.0002	0.3
5.0	0.00003	0.0001	0.3
	1.00	1.00	

Figure 1
Comparison of Radiation in Chamber to Solar Radiation

helps to reduce the experimental difficulties.

Although water ice is probably one of the most widely studied substances, basic information on the sublimation rate of ice into vacuum is not known except for low temperatures. Since the insight into the behavior of ice in space is the objective of this study, considerable experimental effort was devoted to the determination of the sublimation rate as a function of the surface temperature of ice. The description of this behavior is expressed through the evaporation coefficient, $\alpha(T_s)$, which is defined as the ratio of the actual sublimation rate at a given surface temperature, T_s, to the sublimation rate calculated from kinetic gas theory.

Another important objective is to understand the behavior of ice particles as a function of distance from the sun. In order to predict this behavior the interaction of the ice particle with the radiation field must be known. For this purpose the sublimation rates of individual ice particles were studied, while the particles were exposed to a simulated space environment including solar simulation.

In the theoretical treatment, and in particular in the computation of the absorption efficiency, only certain types of particles are amenable to treatment. These include particles of homogenious material or concentrically layered particles. But for real world applications one must allow for the existence of inhomogeneities. Although the theoretical calculations for such "dirty" ice grains are for all practical purposes beyond reach, an experimental means will be introduced below, the essence

of which involves the introduction of an effective complex index of refraction as a function of wavelength. Initial experiments with pure ice spheres are important to establish a base line against which the effects of impurities can be assessed.

Finally, since ice in space is probably generated by a low pressure, low temperature deposition process, a pilot investigation into the energy release of the resulting ices was carried out. (Since the deposition experiments were prompted by a new theory for comet activity which was also an outgrowth of this study, and since a significant modification of the experimental apparatus was necessary, a separate discussion of this subject will be presented in Section 3.4).

3.2.3 Experimental Results

3.2.3.1 The Evaporation Coefficient - Ice sublimating in space is in a non-equilibrium situation which results in deviations of the sublimation rate expected from equilibrium vapor pressure considerations. The correction factor is represented by a quantity defined as the evaporation coefficient.

3.2.3.1.1 Introduction - The studies presently available in the literature concerning the evaporation coefficient of ice display large discrepancies and do not clearly demonstrate the temperature dependence of this quantity over an extended temperature range. A summary of previous results is provided by Davy and Somorjai (Ref. 11). Besides obvious disagreement between the results of different experimenters, there exists a gap in the temperature range between -10 and -45°C where no results are available.

Because of the apparent lack of reliable data, an attempt was made to measure the evaporation coefficient and its temperature dependence in this range. To this end, an experimental determination of the sublimation rate as a function of the surface temperature of the ice has been conducted. The use of the oscillating fiber microbalance offered an opportunity to measure the evaporation coefficient with the presently available experimental setup. The experiment was carried out in two steps.

Step 1. A water droplet is suspended at the end of the quartz fiber. The loaded fiber is placed into the vacuum chamber which is then slowly evacuated. The lowering of the gas pressure and the resulting increase of the evaporation rate provides for an efficient cooling of the water droplet which becomes supercooled. At some point, the water droplet freezes. This freezing has a profound consequence. The latent heat of fusion is released, and the droplet comes to a uniform temperature of zero degrees centigrade. During this time the quartz fiber has been maintained in oscillation. As the droplet freezes, a dramatic increase of the sublimation rate can be noted by the rapid frequency change of the oscillating fiber. After the energy supplied by the latent heat is used up through sublimation, the ice particle cools rapidly and asymptotically reaches a quasi-steady state sublimation rate. Since the fiber is maintained in oscillation continually, the result is a measurement of the sublimation rate of the ice particle as a function of time during the freezing event and the subsequent cooling period.

Step 2. A water droplet is suspended at the end of a fine thermocouple.

Now the identical treatment as described in Step 1 is applied to this

configuration. The vacuum chamber is slowly evacuated and the supercooling

of the droplet is apparent from the thermocouple reading. As in the case

above, the supercooled droplet freezes and the thermocouple indicates that

the temperature of the droplet jumps to zero degrees centigrade. After the

latent heat is expended the temperature of the ice particle drops and

finally reaches a steady state value. The rate of cooling at different

locations in the ice particle is measured by the position of the thermocouple

junction which can be at the surface or in the interior of the ice particle.

Through this approach it is possible to determine the surface temperature

as a function of time.

If the results of Step 1 and Step 2 are combined for ice particles

of the same size, frozen under identical conditions of wall temperature

and low pressure, one can obtain the sublimation rate as a function of

surface temperature. The ratio between the experimentally observed and the

theoretically expected sublimation rates yields the evaporation coefficient

as a function of temperature. In the next section the experimental results

will be presented and the experimental details will be discussed.

3.2.3.1.2 Development of Experimental Procedures

3.2.3.1.2.1 Particle Fragmentation - Although the steps described in

the previous section seem straightforward, the actual execution of the

experiments leads to difficulties and also insights that were not expected

at the outset.

Implicit in the method mentioned above is the necessity for an

ambient pressure in the molecular flow region so that the net return
flux of water molecules to the subliming surface is negligible. It is
therefore essential that the water droplets do not freeze before this
pressure regime is reached.

At first when the suspended water droplets were introduced into
the chamber and slowly decompressed, the drops would invariably freeze
at about 5 torr (approximately the triple point). Upon freezing the
resulting particles would also fragment usually into two hemispherical
sections, one of which would stay attached to the fiber. These runs were
totally useless for sublimation rate measurements, since the pressure at
freezing was still considerably higher than could be tolerated. Also the
remaining fragment still on the fiber did not have the simple geometry
which assures symmetry and reliable experimental results. A typical
fragmented particle can be seen in Figure 2 which was obtained through a
motion picture series with stroboscopic light illumination. The photograph
shows an event of a secondary fragment ejected from the center of the
remaining hemisphere.

After repeated attempts to achieve supercooling and freezing without
fragmentation at low pressures, it was necessary to determine the causes
for premature nucleation. One suspected cause for nucleation was the
release of dissolved gases in the droplet as it cooled. The presence of
even tiny air bubbles in the water could act as nucleation centers and
prevent supercooling. To reduce this possibility the doubly distilled
water used for the experiment was boiled immediately before fiber loading.

Figure 2 - Ejection of Ice Fragment Resulting from Droplet
Freezing (50X)

Indeed this measure significantly improved the situation. After the
introduction of this treatment most of the droplets could be supercooled, and
the majority of the droplets made of freshly boiled water which froze
below 5 torr did not fragment.

3.2.3.1.2.2 Sublimation Runs - It was expected that all sublimation
runs would exhibit a clearly predictable behavior. At low pressures the
functional dependence of the sublimation rate on time should only vary
with two parameters, droplet size and wall temperature. A sublimation run
is shown in Figure 3. The ordinate shows the sublimation rate in
$(g\ cm^{-2}sec^{-1})$, plotted as a function of time in (sec.). This curve is
for an ice particle size with a radius $r = 335\ \mu m$ as measured immediately
after freezing. The shroud temperature was $273^{\circ}K$ and the pressure was
below 5×10^{-5}torr. The starting time is of course arbitrary. Between $t_o = o$
and $t_1 = 2$ sec the data were taken while the waterdrop was in a supercooled
state. In this situation the data are somewhat noisy. This noise is
caused by the wobbling motion of the supercooled droplet which interferes
with the periodic motion of the fiber and leads to frequency uncertainties.
This problem disappears as soon as the droplet solidified. Upon freezing,
at $t_2 = 2$ sec the sublimation rate suddenly rises by orders of magnitude
since the ice particle dissipates the freed latent heat mainly by sublimation.
After having reached a maximum, the sublimation rate declines as a
consequence of the decreasing surface temperature of the ice particle and
eventually reaches a steady state condition. It may be pointed out that
the energy household during the cooling period after freezing goes through

Figure 3
Sublimation vs. Time During Freezing

$R = 335 \ \mu m$
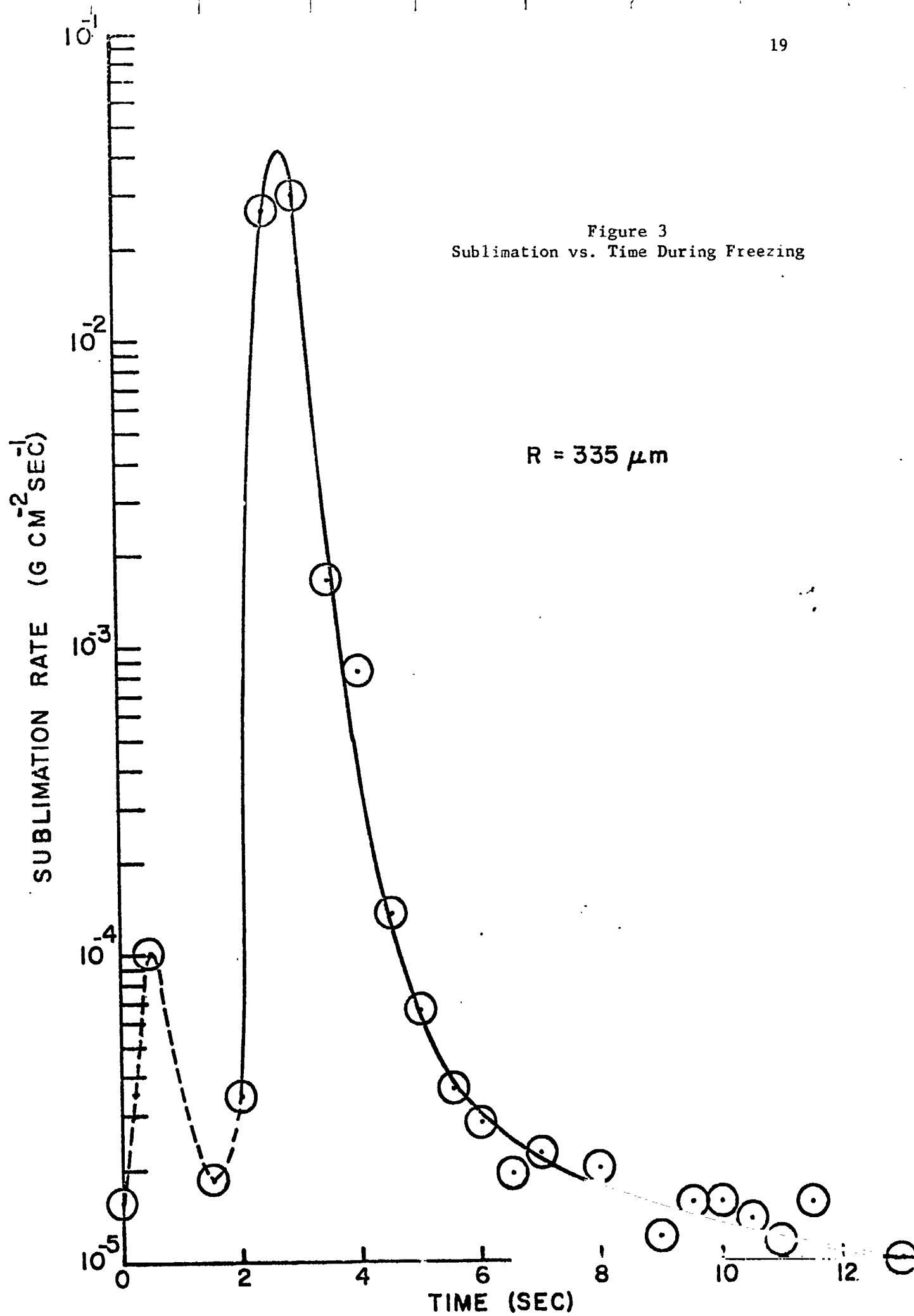
entirely different stages. The major energy contribution at freezing

and shortly thereafter is the result of the release of the latent heat

of fusion. After this energy source is dissipated the interior of the

ice particle will supply the ice surface with energy by thermal diffusion.

During freezing and in the early stages after freezing, influences due to

other energy sources can be neglected. Such a neglection is no longer

possible, however, as the sublimation rate progresses towards the steady

state condition. There the energy supplied to the ice particle by radiation

from the surrounding walls becomes dominant. Also one must take into

account the energy supplied through the quartz fiber which suspends the ice

particle. This influence can be minimized, however, by using fibers whose

diameter is small compared to the diameter of the ice particle. (For more

detail on this topic see Ref. 9).

From these considerations, it is apparent that there are two pieces

of information which can be extracted from these sublimation curves which

are invariant to a wide range of external conditions. The first is the

sublimation peak which should be representative of the sublimation rate

at zero degrees centigrade. The second pertains to the decline of the

sublimation rate shortly after freezing. The invariance of the sublimation

peak can be understood because under no circumstances can there be any

other temperature but zero degrees centigrade at the moment of freezing.

The invariance of the initial decline of the sublimation rate can be

understood because in this case the heat transfer problem for the heat

transport from the interior of the ice particle to the surface can be

considered as a one dimensional problem. Since the sublimation rate is normalized in respect to the surface area, the sublimation rate is independent of the particle size and therefore also invariant. As the temperature gradients extend further into the interior of the ice particle however, the size of the ice particle and with it the stored heat energy becomes a rate determining factor.

In Figure 3 a sublimation run was shown where the sublimation rate is given as a function of time. The freezing event of the supercooled waterdrop expresses itself in a sudden rise of the sublimation rate to a maximum followed immediately by a characteristic drop. There were numerous instances, however, where the sublimation behavior immediately after freezing was completely different. Examples of some of these typical runs are shown in Figures 4 and 5. Here it becomes apparent that contrary to our expectation, two sublimation maxima appear. In any particular run, only two maxima have ever been observed. The maximum time separation between peaks is about 10 seconds, while the minimum separation is not certain due to the constraints imposed by the time resolution of the sublimation rate measurement. At first it was very difficult to account for this type of behavior. Our first working hypothesis was that a mass ejection during freezing is responsible for one of the peaks.

3.2.3.1.2.3 <u>Motion Pictures of the Freezing Process</u> - In order to gain a better insight into the processes involved, motion pictures of droplets were taken during freezing. In Figure 6, sequences of motion picture frames are shown which were taken with a frame rate of 16 frames/sec.

Figure 4
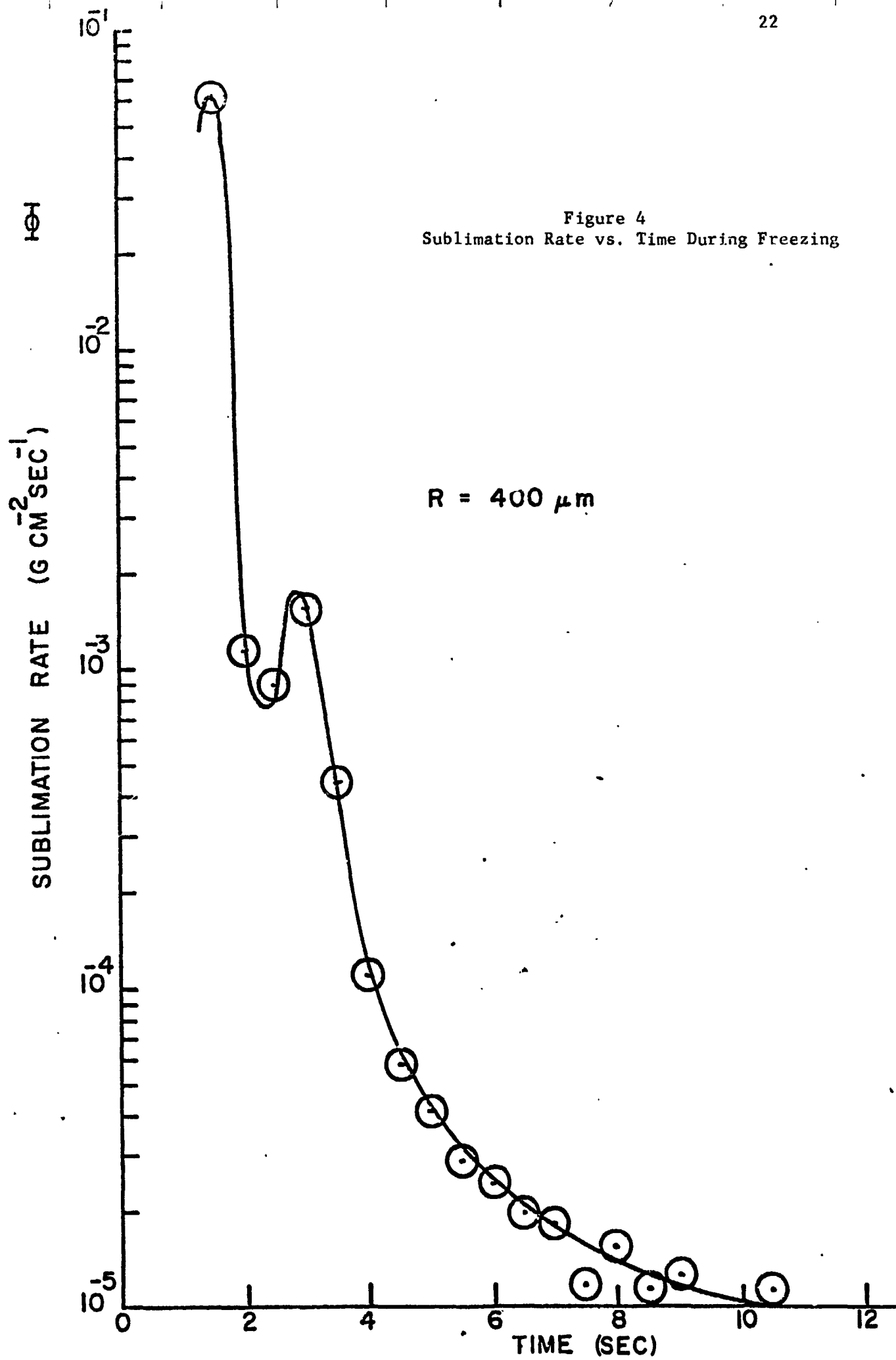Sublimation Rate vs. Time During Freezing

R = 400 μm

Figure 5
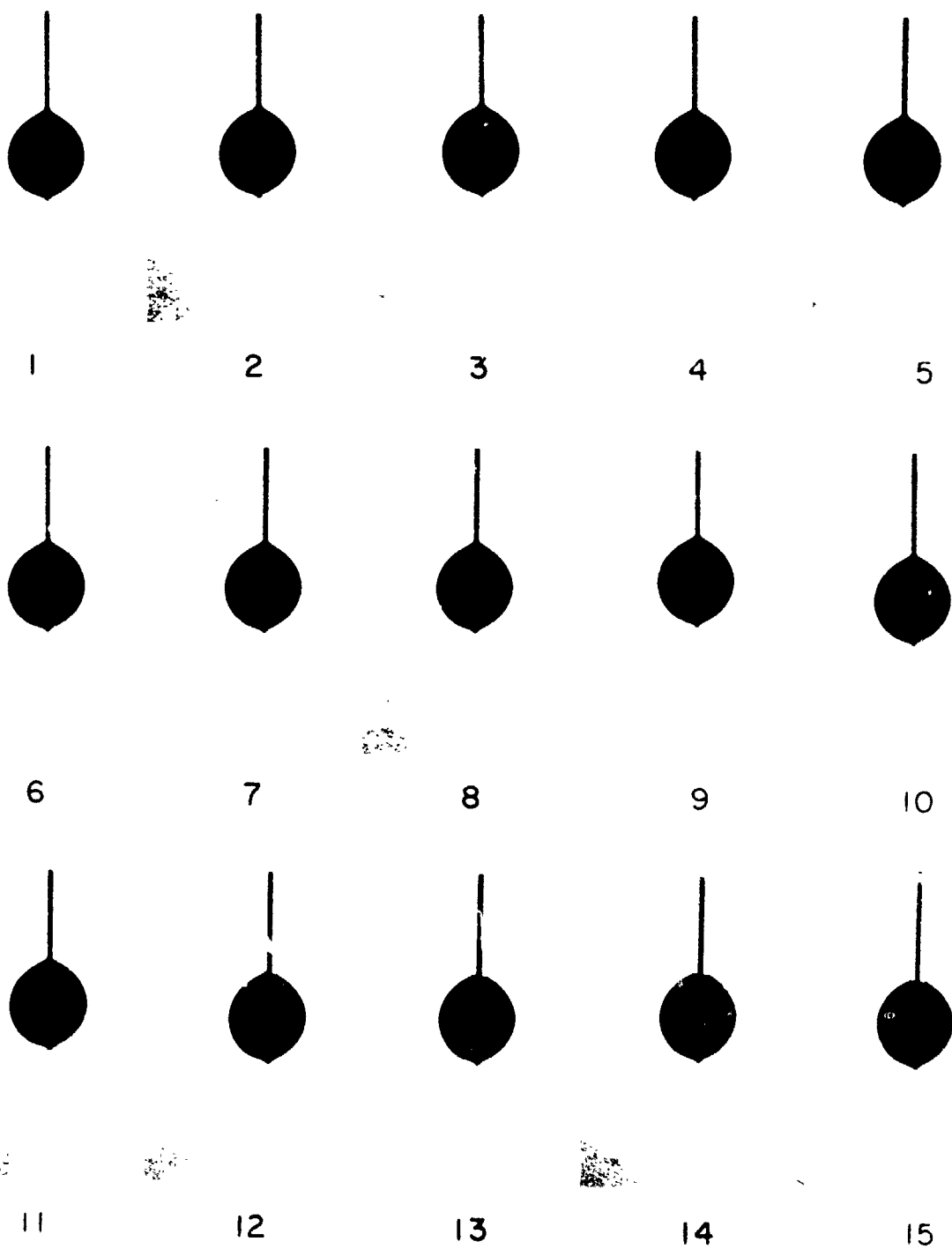Sublimation Rate vs. Time
During Freezing

$R = 375 \mu m$
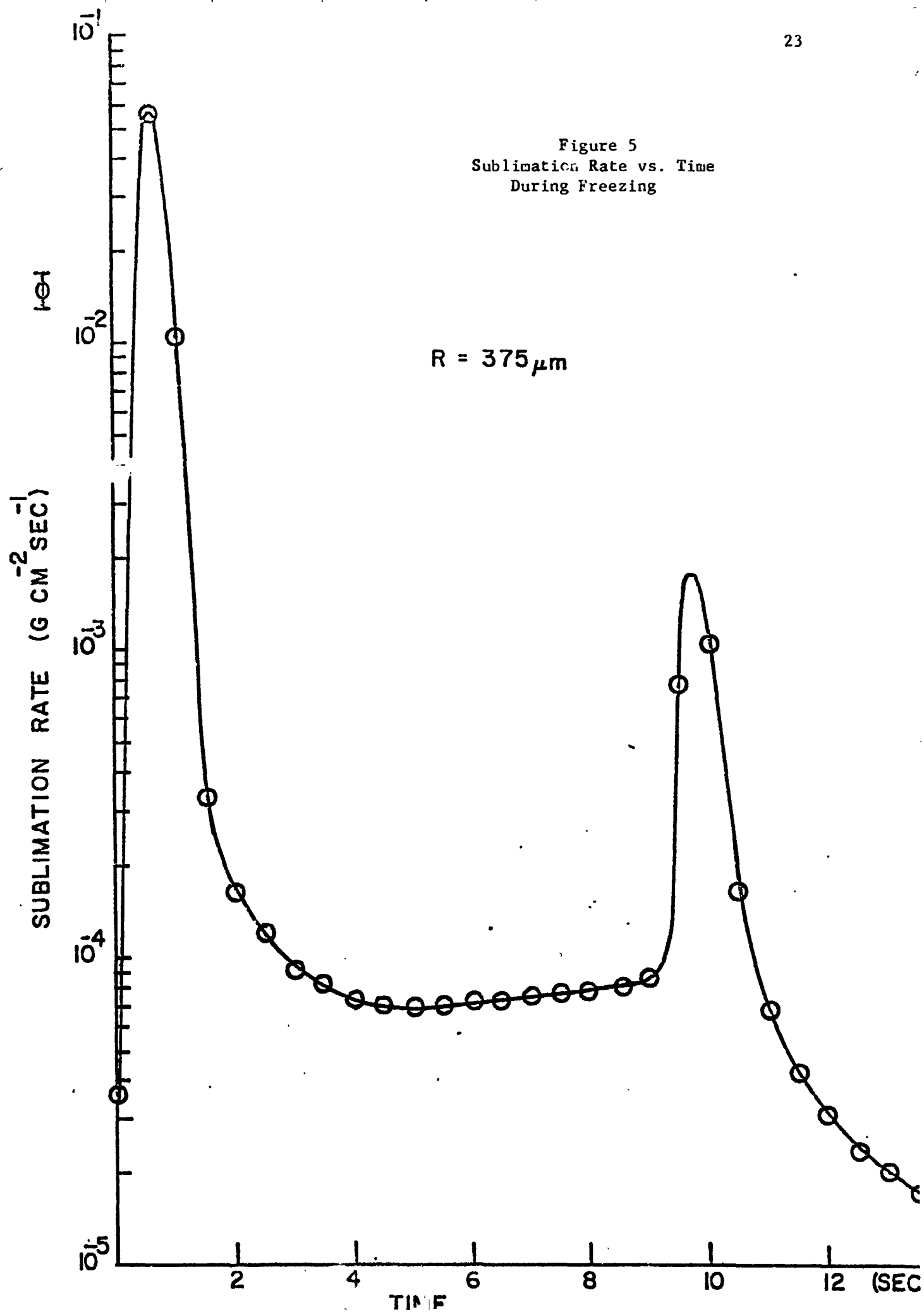
Figure 6(a) - Motion Picture Sequence of Freezing Droplet (22X)

16   17   18   19   20

21   22   23   24   25
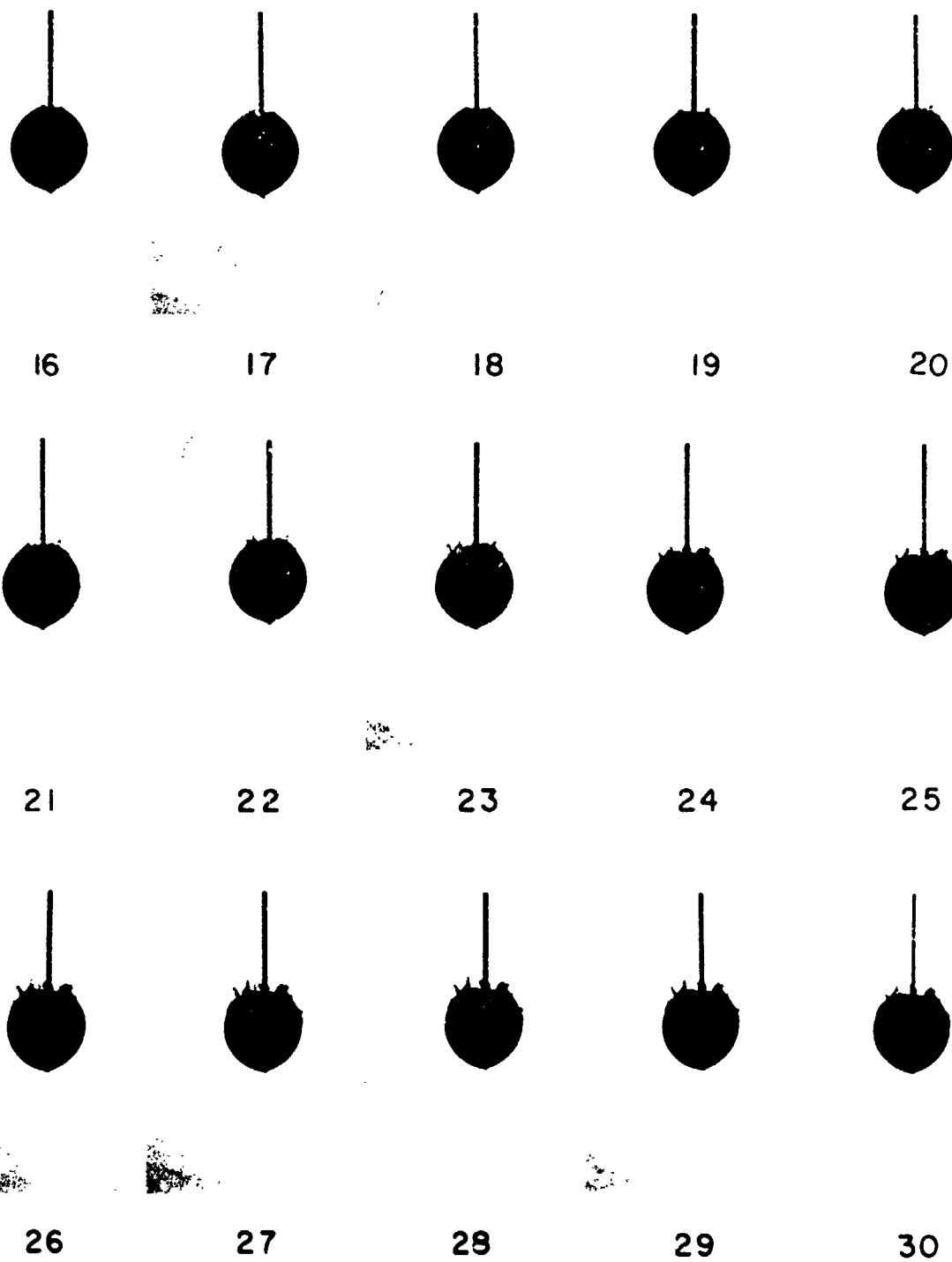
26   27   28   29   30

Figure 6(b)

In the sequence of Figure 7, a droplet is attached to the side of the quartz fiber. This is not the usual position of droplets when mass measurements are taken. But for the purpose of following the visual appearance of the droplet through the freezing process, this position allows for a better view through the interior of the droplet. In the first two frames the supercooled droplet appears transparent. When one proceeds to the third frame the appearance has completely changed. In the time interval between the second and third frame the droplet froze and became completely opaque. While the freezing time cannot be resolved here, it is smaller than 1/16 sec. During the sequence of the next 16 frames (from 4 through 19) one can notice a gradual improvement of the transparency of the ice particle. In about the 18th and 19th frame the ice particle has become almost as transparent as the original liquid supercooled droplet. Note that the particle is indeed frozen as evidenced by the discontinuities of the surface curvature. After the 19th frame the ice particle becomes again more opaque within a few frames. From then on however no further changes of the visual appearance can be noted.

3.2.3.1.2.4 Simultaneous Motion Picture and Sublimation Rate Measurements - In Figure 6 the quartz fiber is located in the middle of the droplet. In this sequence of pictures a simultaneous measurement of the sublimation rate was made. This was accomplished by a modification of the illumination system for the optical feedback which keeps the fiber in oscillation. (For details of the feedback system see Ref. 9).

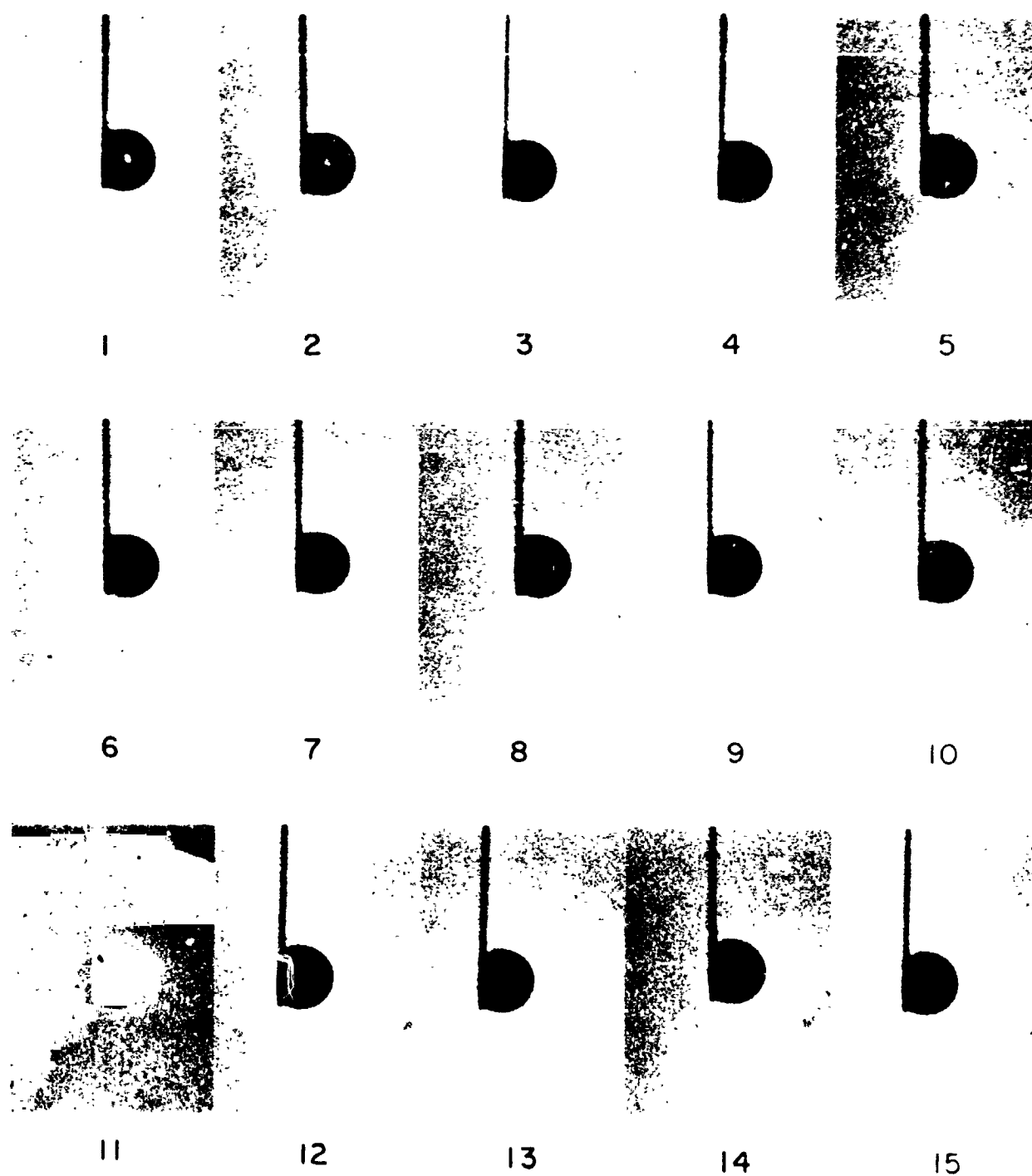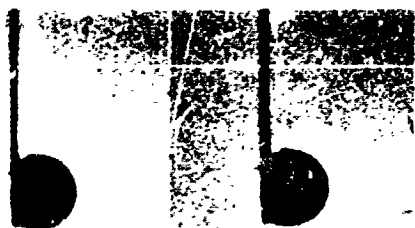In order to supply illumination for the exposure of the movie film

Figure 7(a) - Motion Picture Sequence of Freezing Droplet (22X)

16 17 18 19 20

21 22 23 24 25

26 27 28 29 30

Figure 7(b)

two precautions had to be taken. One is to keep the radiation level
in the vacuum chamber at a minimum so that extra heat does not interfere
with the sublimation measurement. At the same time the sensitive photo-
transistor must be protected from the high illumination levels which are
required for the photography. With these considerations in mind the
following experimental arrangement was employed. To ensure sufficient
illumination for the photographic process with a minimum of radiative
heat transfer to the droplet, a stroboscopic light was used and synchronized
with the shutter of the movie camera. In order to protect the photo-
transistor of the optical feedback system, the phototransistor was used in
conjunction with an infrared filter. In order to protect the film from
the illumination of the optical feedback system, the light source for the
phototransistor was also passed through an infrared filter. The arrangement
is shown in Figure 8. The frequency measurement of the fiber was
synchronized with the film by an event marker which was activated about
every 20 seconds. This provided an event signal on the frequency print-out
and at the same time stopped the stroboscope pulses. This resulted in
blank frames on the film. Through this procedure, a coordination of visual
appearance with the mass of the particle and thus with the sublimation rate
was achieved.

In Figure 6 the visual appearance of the supercooled drop is shown
in frame number 1. Since the quartz fiber penetrates the center of the
droplet the central transparent region is somewhat attenuated compared
to Figure 7. Nevertheless at least in the original negative the distorted,
amplified image of the fiber can be seen in the transparent part of the droplet.
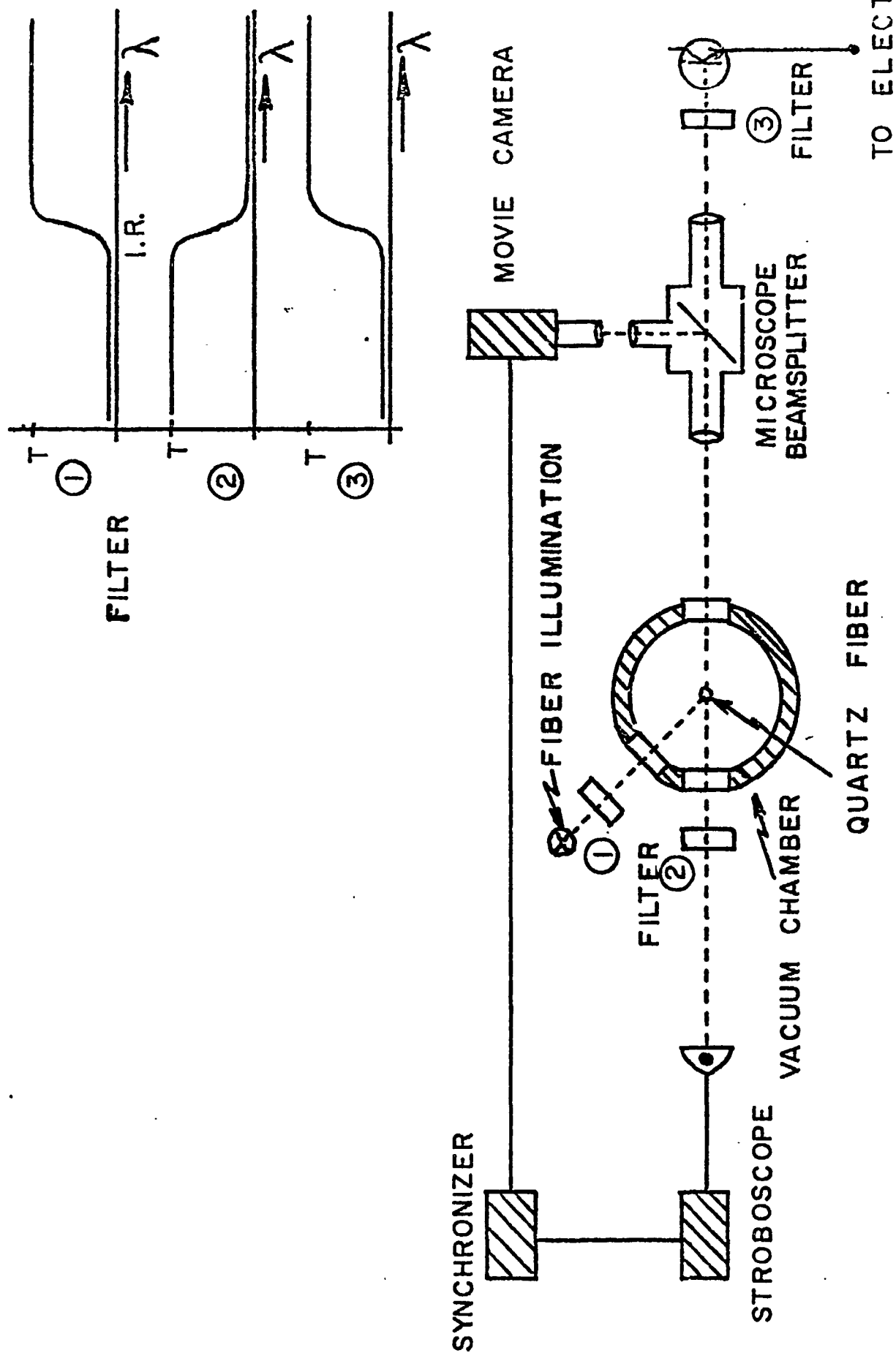
Figure 8

Components for Simultaneous Sublimation Rate and Particle Transparency Information

The simultaneous sublimation rates are shown in Figure 9.
Between frame 2 and frame 3 the freezing of the supercooled droplet
occurs as is evident by the sudden opaqueness. Frame 3 recorded on film
sometime within the interval indicated in Figure 9. The freezing event
apparently coincides with the first maximum of the sublimation rate. As
in the previously discussed freezing history, the ice particle becomes
increasingly transparent between frame 3 and frame 24. The sublimation
rate during this time period goes through a minimum. As in the previous
freezing event, the ice particle once again becomes opaque at around
frame 25. Unfortunately the gradation of opacity is not as easily visible
as in Figure 7. The greatest change in visual appearance seems to be
between frame 24 and frame 25 with the greatest transparency occurring
at frame 23. The occurrence of frame 23 is indicated in the time interval
shown in Figure 9. It seems to coincide with the second maximum of the
sublimation curve.

Another experimental run is shown in Figures 10 and 11. Figure 10
shows the visual appearance of the supercooled droplet as it proceeds
through the freezing process, while Figure 11 exhibits the sublimation
rate during this event. As in the previous examples the onset of the
freezing is brought out by the sudden loss in transparency of the particle
between frames 2 and 3. As before the transparency is partially restored,
reaching a maximum at about frame 21. After frame 22, the particle once
again becomes opaque.

In the three motion picture runs (Figures 6, 7, and 10) one can
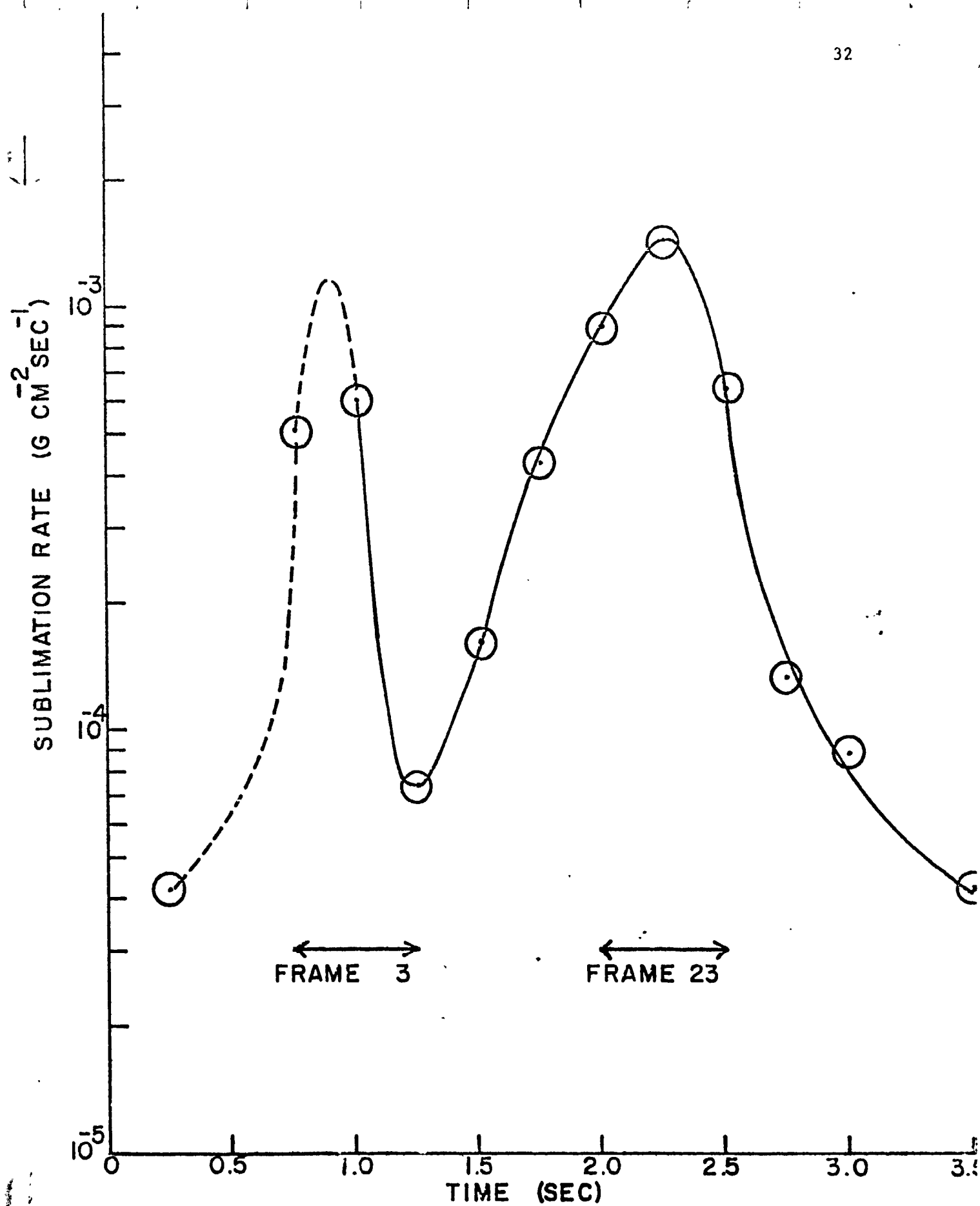
Figure 9
Coordination of Sublimation Rate with Motion Picture Sequence

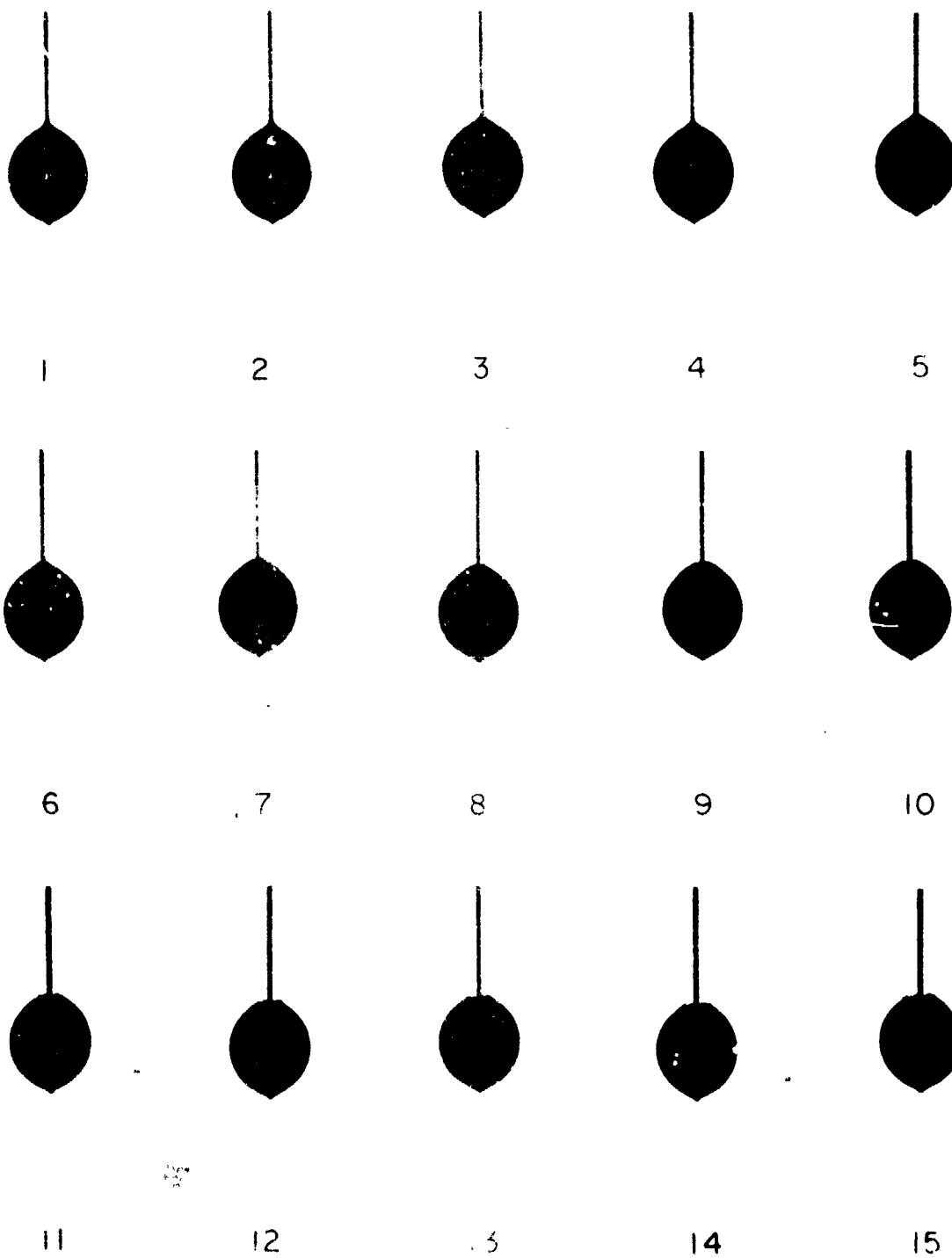1 2 3 4 5

6 7 8 9 10

11 12 13 14 15

Figure 10(a) - Motion Picture Sequence of Freezing Droplet (22X)

16 17 18 19 20
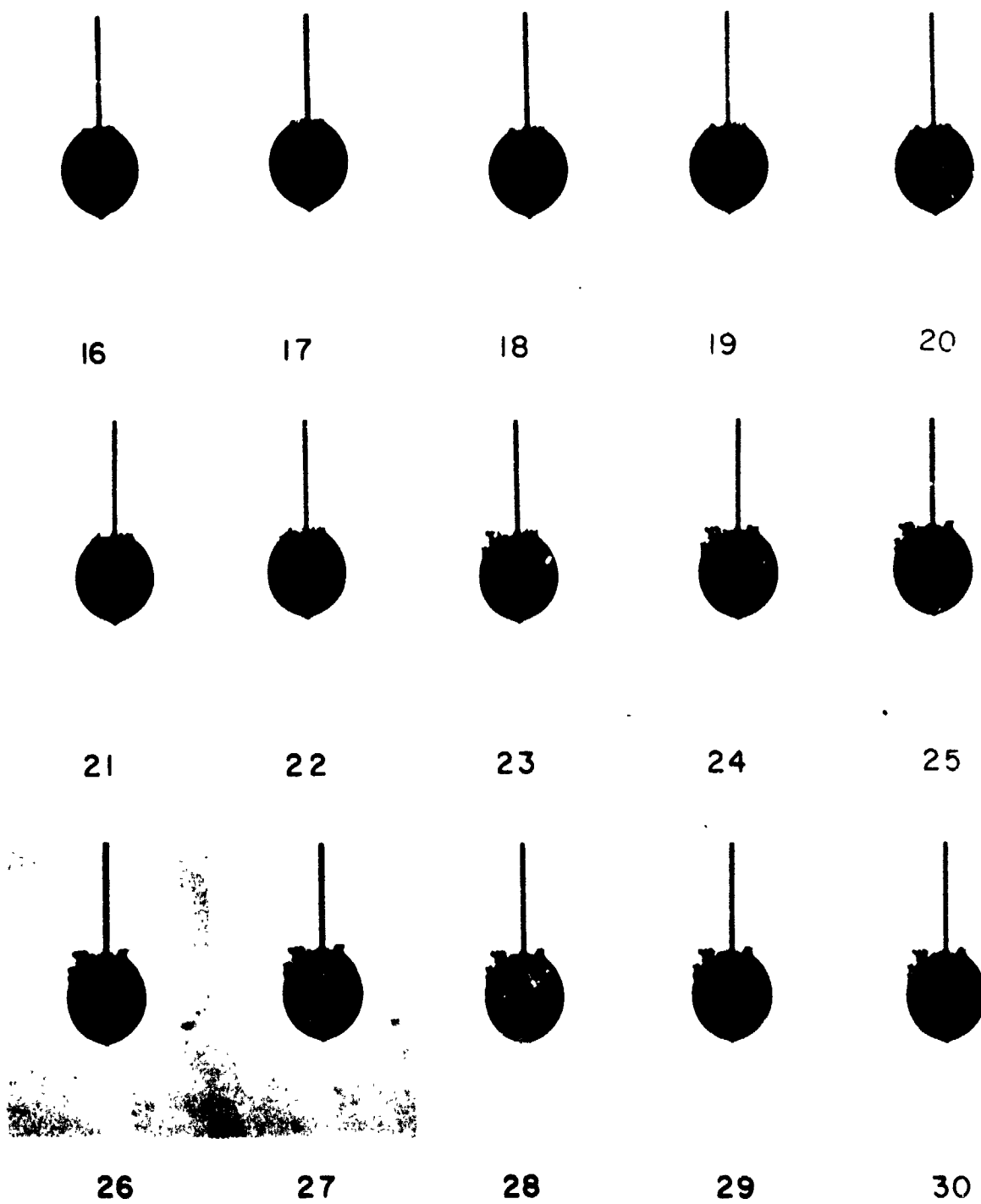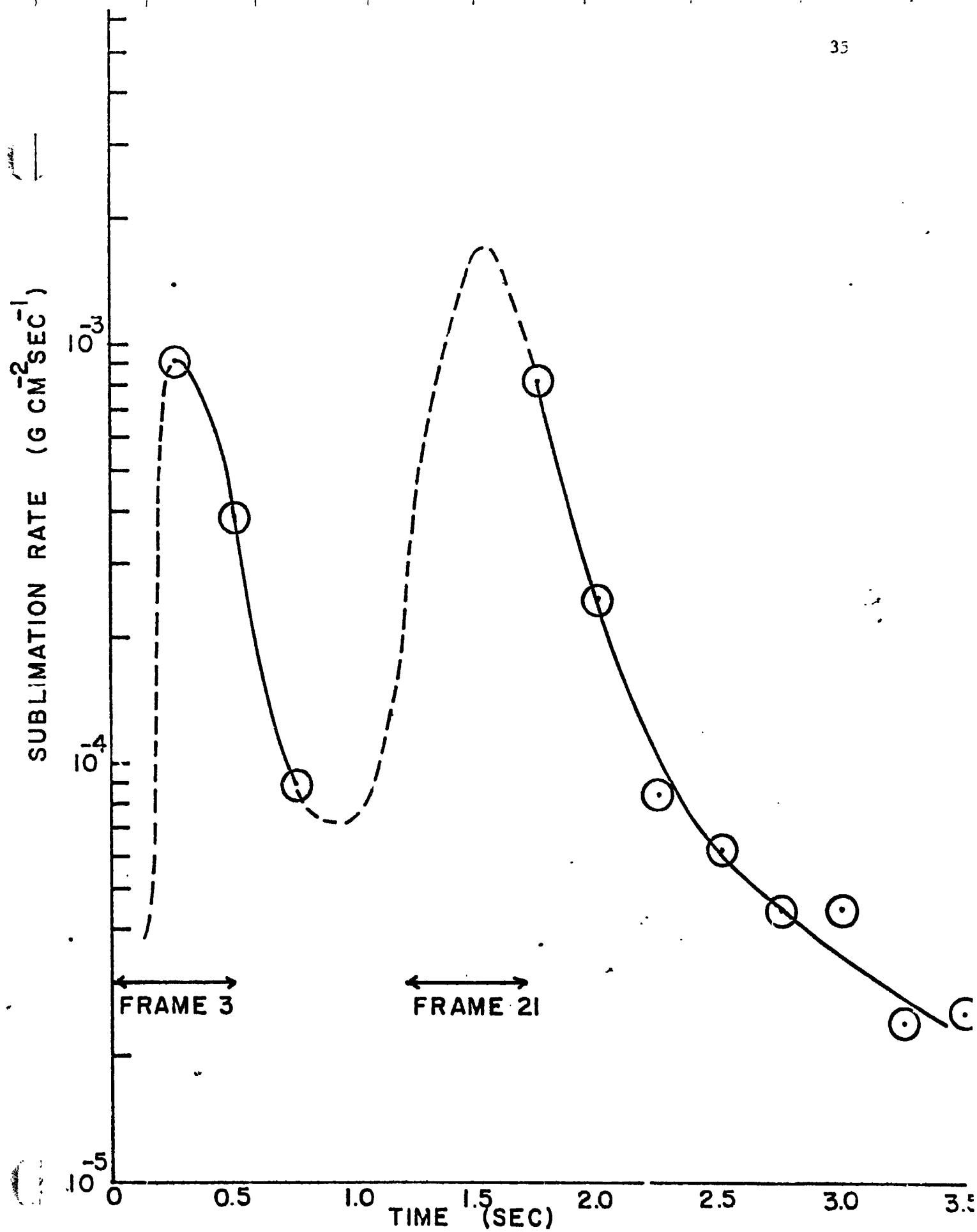
21 22 23 24 25

26 27 28 29 30

Figure 10(b)

Figure 11
Coordination of Sublimation Rate with Motion Picture Sequence

observe the apparent separation of dendrites from the surface at the top of the ice particle during the time of increasing transparency. A close study of consecutive frames strongly suggests that the structure of the surface of the ice particle is made of dendrites running parallel to the ice surface. The quartz fiber disrupts the continuity of the dendrites creating loose ends, which curl back continuously with each frame. Note for instance the sequence of dendrites in frames 13 and beyond in Figure 6. The dendrites are present well before the ice particle reaches its final opaque appearance. Therefore the dendrites must be part of the initial freezing process. It appears that the freezing of an ice particle in vacuum is not a simple event. In order to develop a working hypothesis for the observed sequence of events more experimental facts have still to be developed. Of prime importance in this respect is a determination of the surface temperature of these particles during the freezing process.

3.2.3.1.2.5 <u>Surface Temperature Measurements</u> - In order to follow the surface temperature of supercooled water droplets through the freezing process, tiny chromel-constantan thermocouples with wire diameters varying from $12.7 \mu m$ to $25.4 \mu m$ were loaded with water droplets in the same fashion as the quartz fiber of the oscillating fiber microbalance. After loading, the thermocouple was inserted into the vacuum chamber in the same location where sublimation runs were performed and subjected to the same treatment. The vacuum chamber was slowly pumped down, and the thermocouple voltage was recorded on an oscilloscope. In Figure 12 a photograph of a supercooled
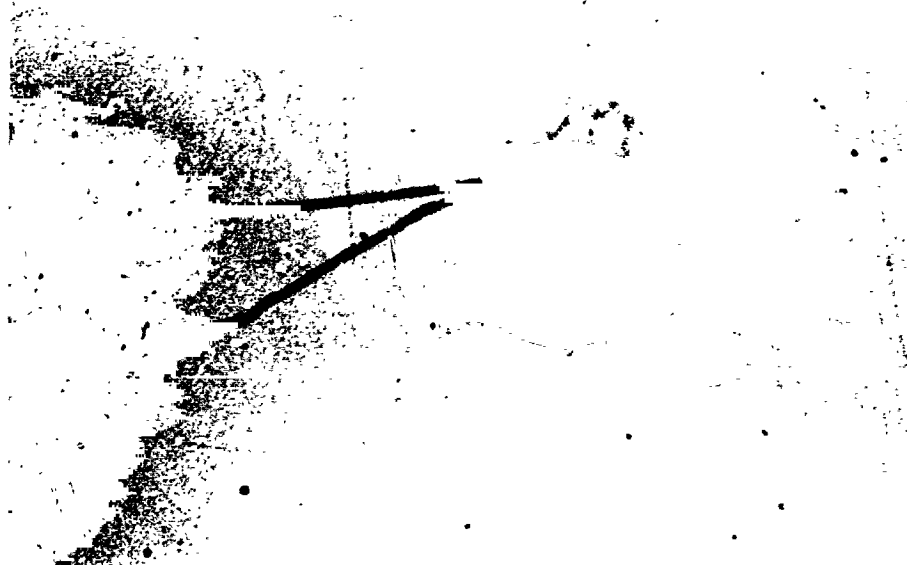
Figure 12 - Thermocouple at the Surface of a Droplet Before and After Freezing (50X)

droplet is shown suspended from a thermocouple made with a 12.7 μm

diameter wire. The thermocouple junction is at the surface of the

droplet. Figure 12 also shows the ice particle resulting from the freezing

of the droplet. Note that the thermocouple is still at the surface. The

dimished size of the ice particle compared to the supercooled droplet is

due to time differential between the taking of the two photographs. Since

there is no way of knowing when the droplet will freeze it is not possible

with a still camera to record the appearance of the droplet immediately

before a freezing.

In order to preserve a record of the temperature behavior during

freezing, an oscilloscope camera was installed. Upon freezing of a

supercooled droplet, the positive slope of the temperature increase sets

the sweep into motion, and a record of thermocouple voltage during freezing

is obtained. A record of the thermocouple output during freezing is shown

in Figure 13. Several traces prior to freezing are shown in the upper half

of the oscillograph as horizontal lines. These correspond to surface

temperatures of the supercooled droplet of -18°C and -23°C. The calibration

of the photograph is 0.588 mv/cm with a sweep of 0.2 sec/cm. One can

notice another sweep halfway through the picture at -23.5°C. 0.9 sec after

the beginning of this sweep a sudden rise of the surface temperature from

-23.5°C to zero$^{\circ}$C occurs within about 10^{-2} sec. This rapid temperature

rise coincides with the rapid freezing as documented in the first darkening

of the droplet in the motion picture sequences. This moment in the freezing

history corresponds also to the first peak of the sublimation rate measurements.

The observed decrease of the sublimation rate after the first peak
raises the question of whether on not the surface temperature was
changing during the remainder of the freezing process. This question
can now be answered. The temperature remains at a constant zero degrees
centigrade over an extended period and the temperature remains exactly
at zero degreees centigrade until the surface temperature drops abruptly.
In Figure 13 the surface temperature remains exactly at the freezing point
for as long as 0.8 sec. After this period a sudden and sharp drop of the
surface temperature occurs at a rate of about $163^{\circ}C$/sec. This rapid
decline of the surface temperature indicates that all the energy supplied
by the release of the latent heat has been dissipated and that the particle
draws only from the energy stored in the heat capacity. The solid line at
the bottom of Figure 13 is a sweep which was intentially triggered several
seconds after freezing. It indicates a surface temperature of $-70^{\circ}C$. Note
that the decline of surface temperature seems to have a slight hump. This
feature is more clearly visible in Figure 14 where such a hump is super-
imposed on a otherwise typical decay curve. In this photograph one can
also clearly see the fast rise of the temperature and the absolute constancy
of the surface temperature during a time period of 0.72 sec and an initial
decay slope of about $168^{\circ}C$/sec. One can see two premature triggered sweeps,
the lower indicating a temperature of $-17^{\circ}C$. This means that the water
droplet cooled at least to this temperature value prior to freezing. The
final steady state temperature of the ice particle is given by the intentially
triggered sweep at the bottom of the photograph indicating a surface

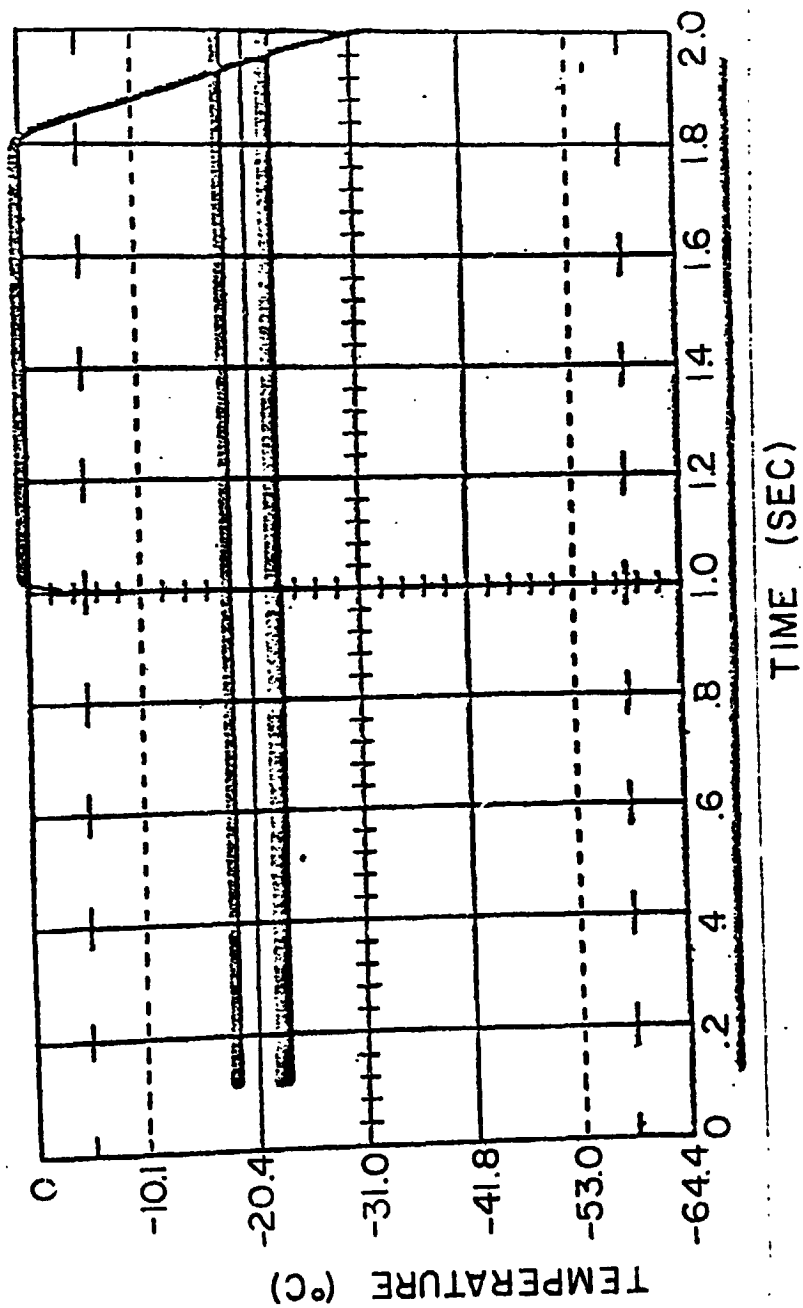TIME (SEC)

Figure 13
Temperature vs. Time at Particle Surface

TEMPERATURE (°C)

0
-10.1
-20.4
-31.0
-41.8
-53.0
-64.4

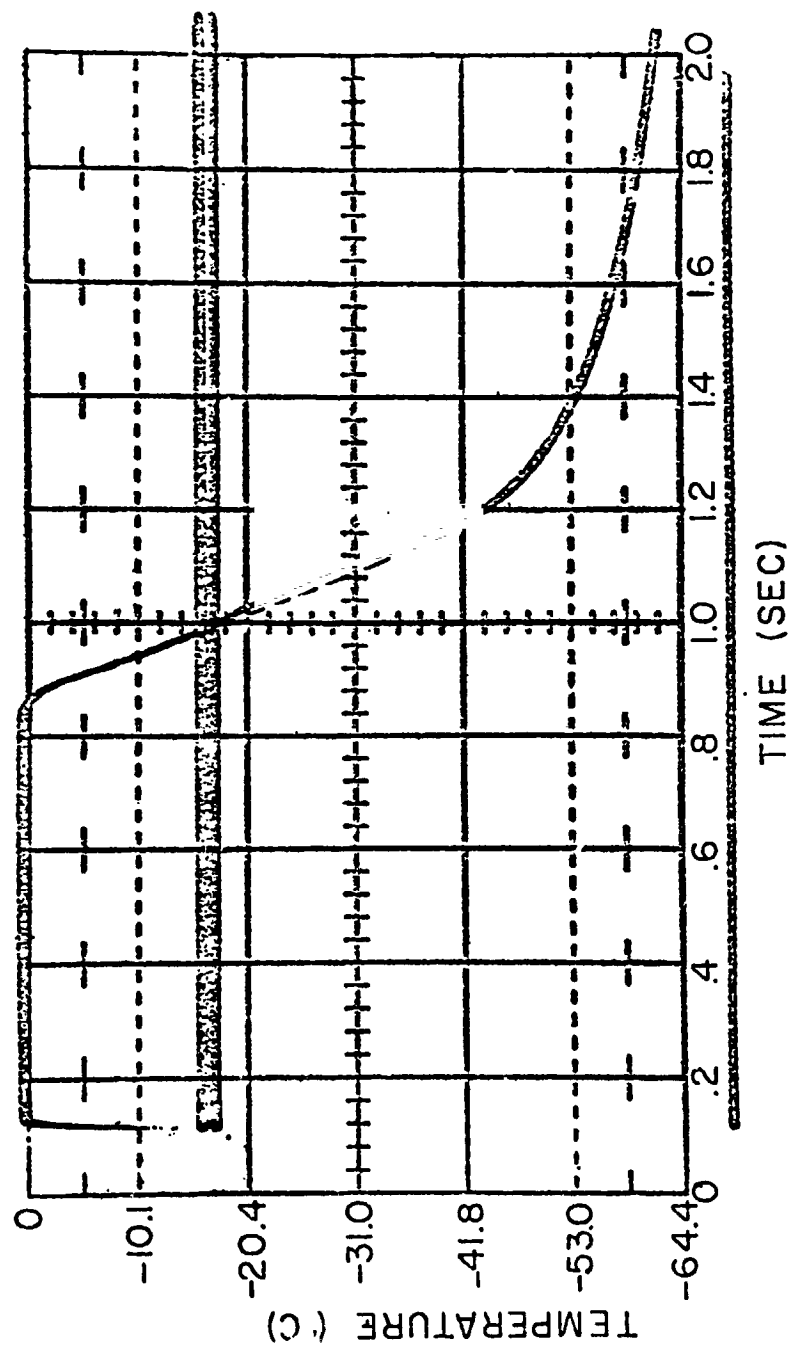0   .2   .4   .6   .8   1.0   1.2   1.4   1.6   1.8   2.0

Figure 14
Temperature vs. Time at Particle Surface

temperature of -70°C. The photographs of the particle prior and after freezing are shown in Figure 15. From these pictures it is not entirely obvious that the thermocouple is located at the surface. To demonstrate, that the junction is located at the surface of the particle a photograph of the unloaded thermocouple is also shown in Figure 15.

A third example of the time dependence of the surface temperature is shown in Figure 16. The same type of behavior is again reproduced. Note again the hump during the cooling of the surface. In this particular example the dwell time at which the surface temperature is at zero degrees centigrade is shorter than in the previous examples and amounts to 0.24 sec. The photographs of the droplet that produced these data are shown in Figure 17. In this case too the thermocouple was at the surface of the particle which can be readily seen if the picture of the unloaded thermocouple is superimposed.

In all the previous examples the surface temperature was measured. For comparison, the time dependence of the temperature at the interior of a particle needs to be examined as it goes through the freezing process. Figure 18 shows a particle in the supercooled and frozen state suspended by a thermocouple, whose junction is the interior. The corresponding thermocouple voltage versus time curve is shown in Figure 19. As in the previous runs depicting the time dependence of the surface temperature, the temperature in the interior of the particle reaches a plateau at 0°C. The dwell time at this temperature was 0.3 sec. The characteristic rapid time from the temperature

Figure 15 - Thermocouple at Surface of Droplet Before and After Freezing (50X)
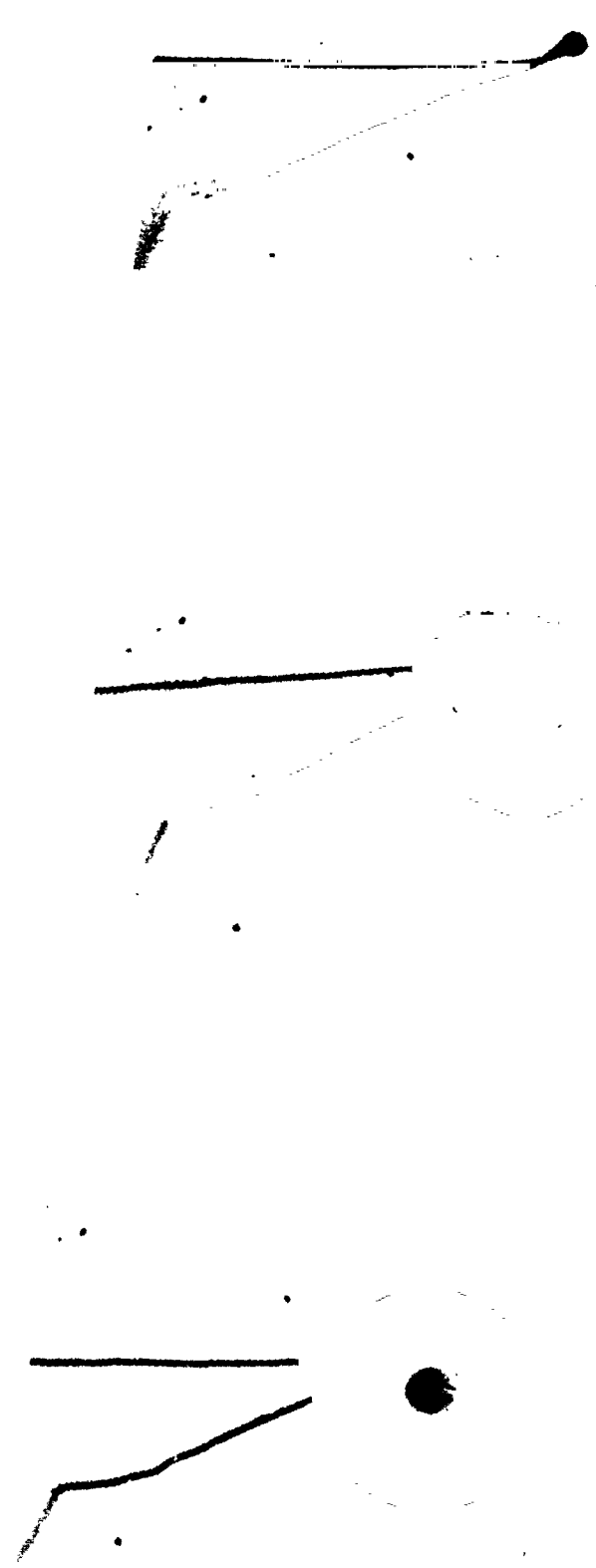
Figure 16

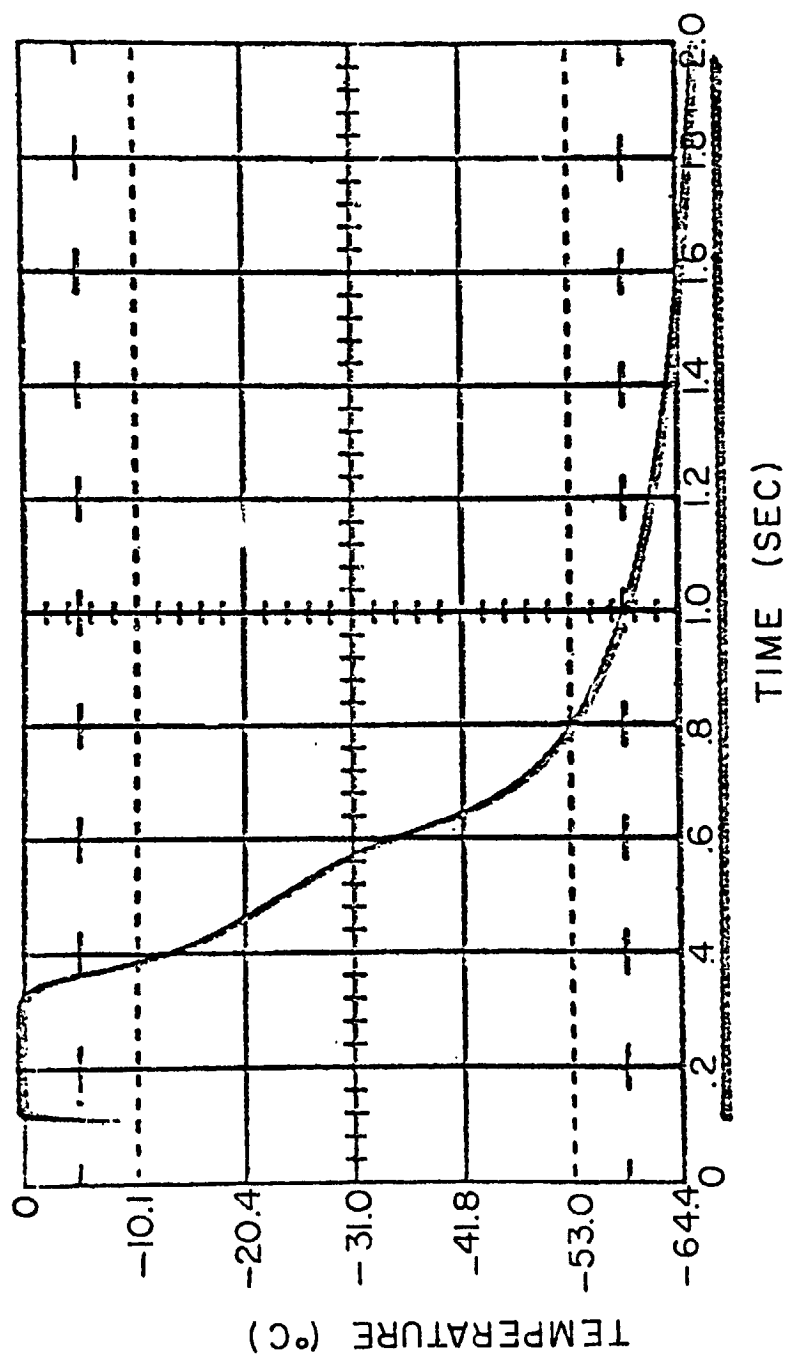Temperature vs. Time at Particle Surface

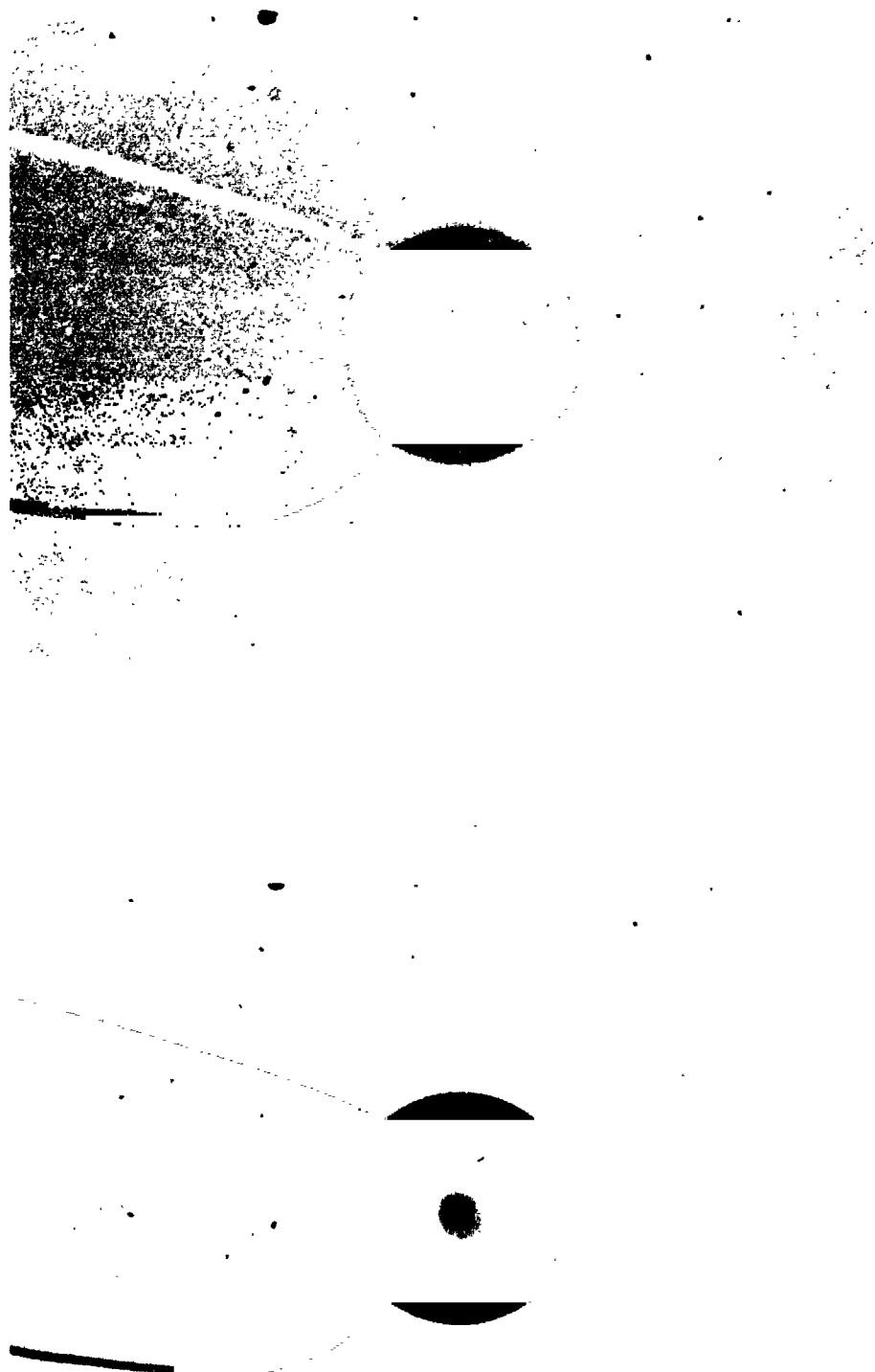Figure 17 - Thermocouple at Surface of Droplet Before and After Freezing (5.0X)

Figure 18 – Thermocouple at Center of Droplet Before and After Freezing (50X)
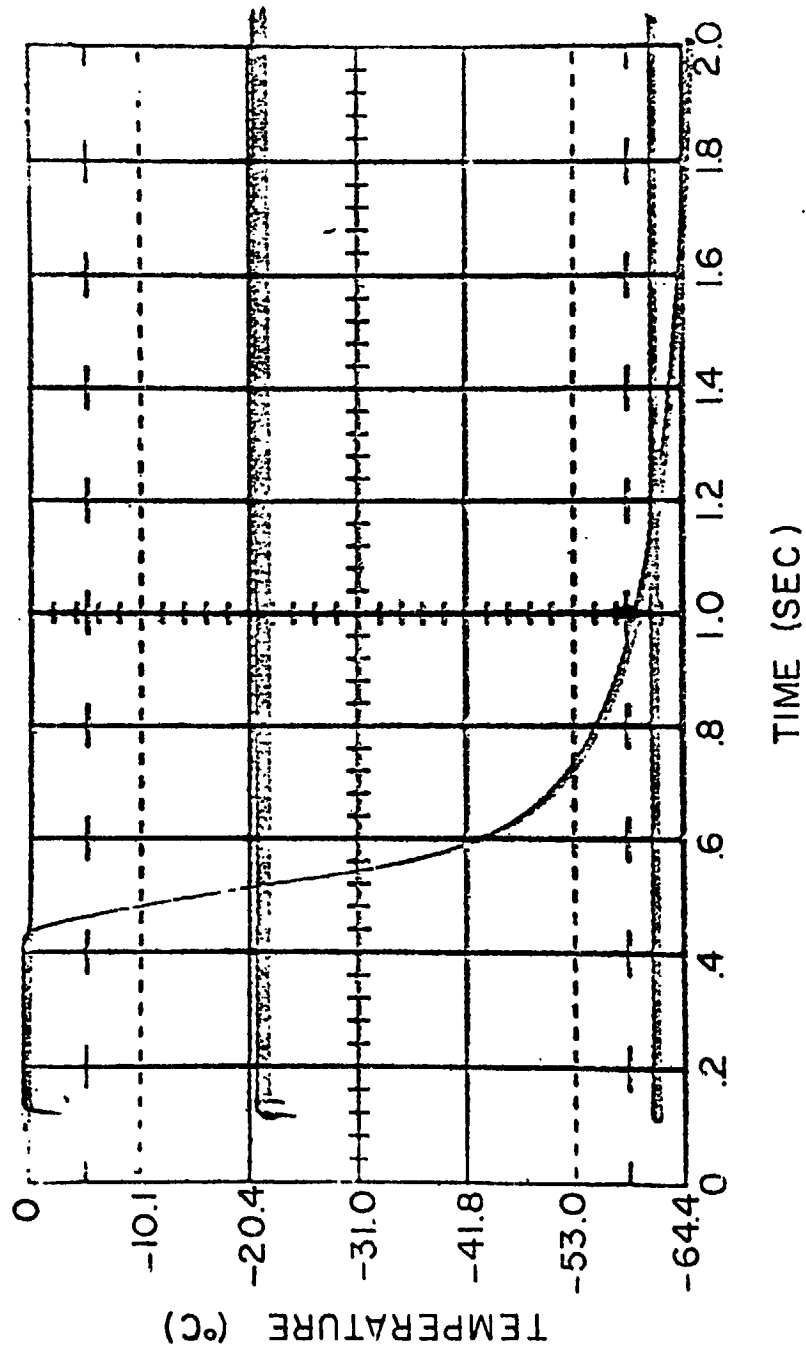
Figure 19
Temperature vs. Time at Center of Particle

of the supercooled state to zero degrees is again clearly discernable.
The initial slope of the temperature decrease is about $-320^\circ C/sec$. This
indicates that the cooling rate in the center of the particle is greater
by about a factor of two. An important point to be noted here lies in
the fact that the hump which is so clearly evident on the surface cooling
curves is not visible in the cooling curves pertaining to the center of the
ice particle. This indicates that the hump is the result of a surface
phenomenon.

The ability to utilize these experimental results on the time
dependence of surface cooling depends upon the reproducibility of the
cooling curves of particles of the same size freezing under the same
conditions. The superposition of the three surface runs discussed above is
shown in Figure 20. The curves have been matched at the clearly identifiable
point in time where surface cooling is initiated. The superposition of the
surface temperature runs leads to a very gratifying result in terms of
consistency of the slope of the temperature decrease, but the above
mentioned surface feature (hump) is lost in the averaging process.

3.2.3.1.3 Interpretation of the Freezing Process of Water Droplets
in Vacuum - A great number of experimental observations have been presented
above. A consistent picture of the freezing of degassed supercooled water
droplets in vacuum can be developed in light of these observations. It turns
out that the freezing process is quite a complex event.

The motion picture shows that the onset of freezing becomes observable
through the sudden change of the transparency of the droplet. This sudden
onset of freezing is also documented by a sudden outburst of the mass loss
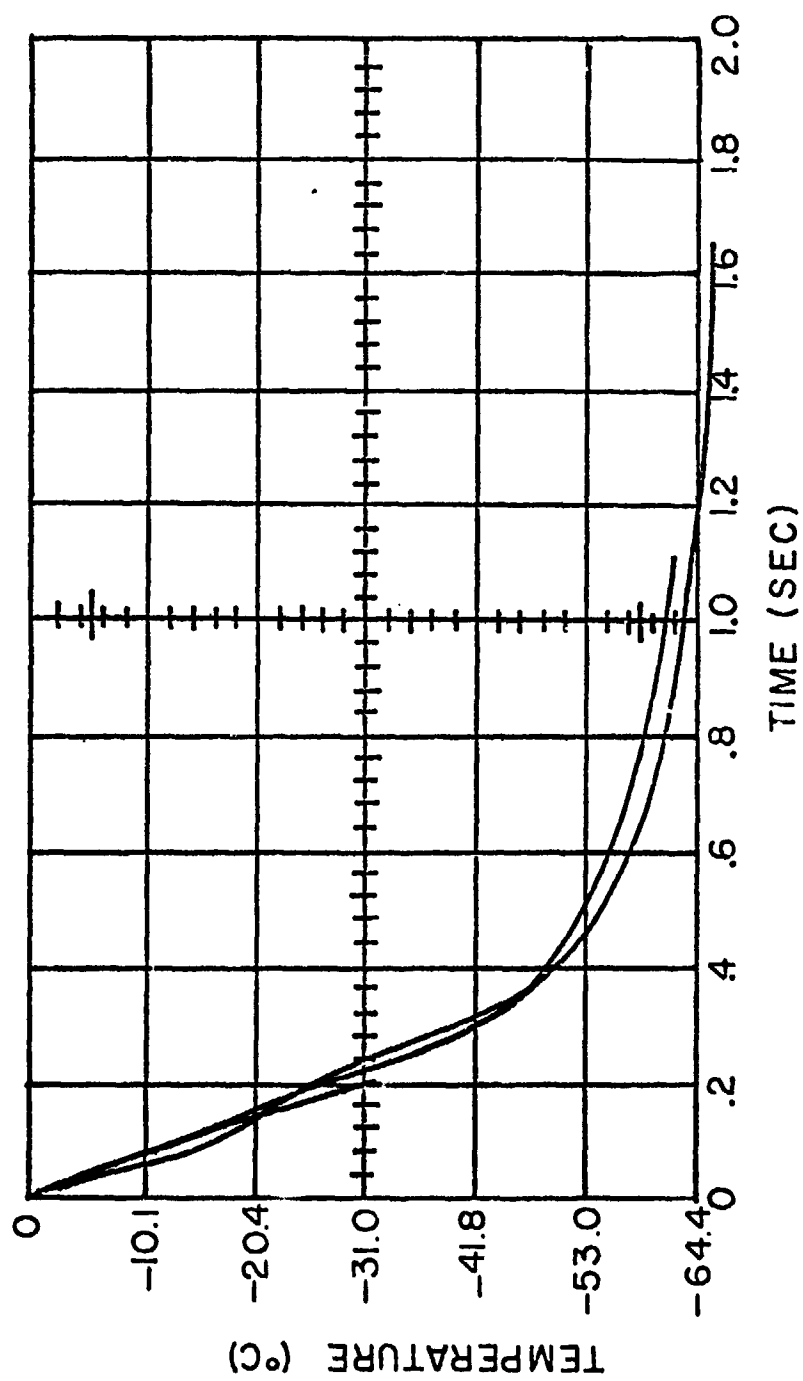
Figure 20
Superposition of Surface Cooling Curves

evidenced by the rapid rise of the first peak in the sublimation curves.
The temperature runs also show a very rapid rise to zero degrees centigrade
within 10^{-2} seconds. It is most likely that a dentritic growth of ice takes
place during this event. Other investigators (Ref. 12), although not working
in vacuum, have observed dendritic growth initiating the freezing of
supercooled droplets, and the growth velocity of dendrites has been measured
to be of the order of 1m/sec. In this first stage of freezing the mass of
dendritces created in the droplet is limited by the need for latent heat to
bring the droplet temperature up to zero degrees centigrade. In this
growth process the dendrites propagate along the surface and form a cocoon
which is filled with water and dendrites. It is an astonishing fact that
the surface temperature stays now absolutely fixed at zero degrees centigrade
for an extended period of time beyond the initial freezing. This is in
contrast to the sublimation rate which drops down after the first peak.
This is not the type of behavior that one would expect for a surface at a
constant temperature. Even more surprising is the appearance of a second
peak which occurs usually between a few tenths of a second to several
seconds after the appearance of the first peak. In Figure 21 the history
of the sublimation rate around the second peak is shown as a composite of
a number of similar sublimation runs. It should be pointed out that the
superposition of the first peaks do not exhibit a constant level of the
sublimation rate, but vary widely. In constrast, however, the sublimation
rate at the second peak is consistently reproduced from run to run. By
the synchronization of the motion pictures with the sublimation rate
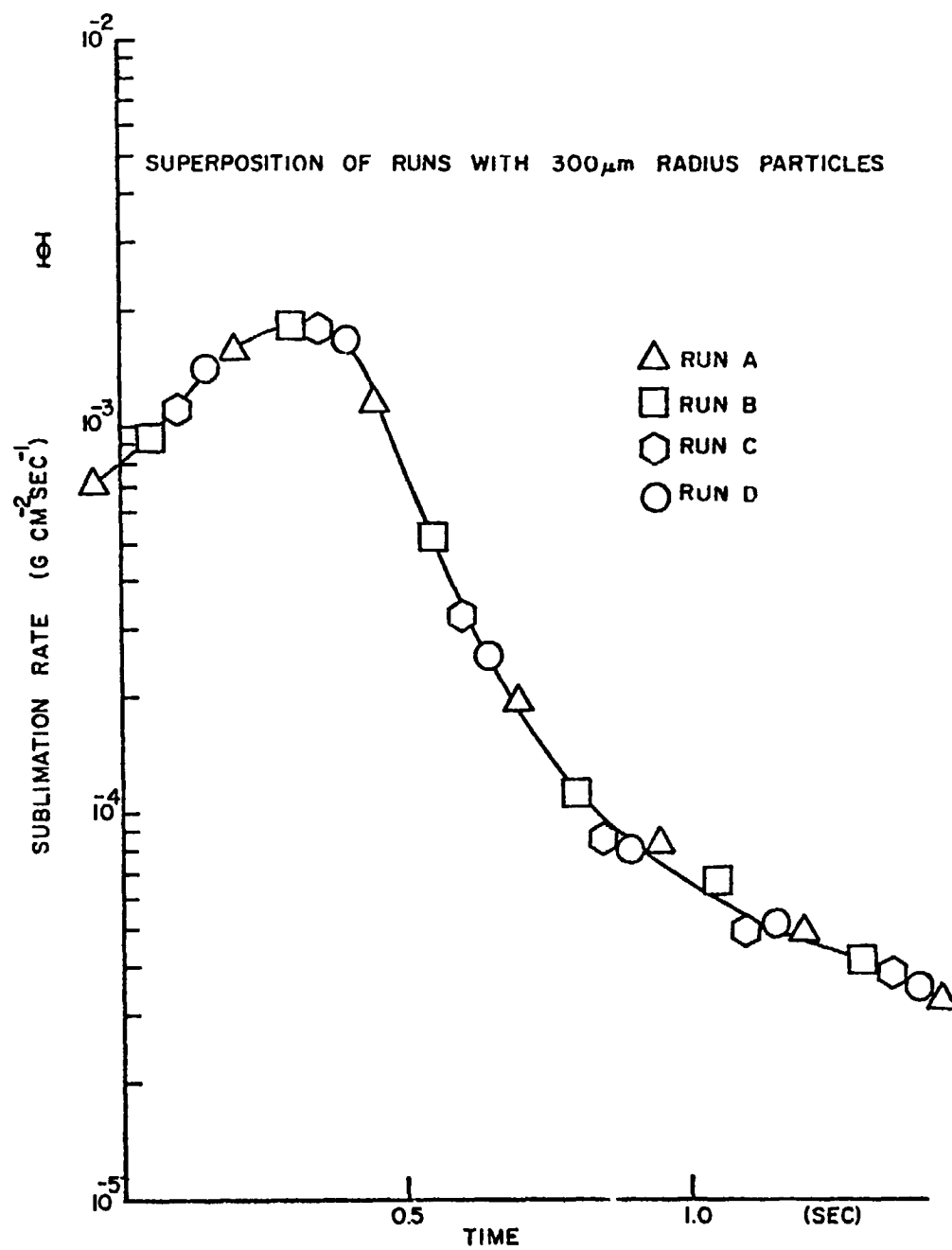
Figure 21
Superposition of Sublimation Rate Curves

information it was clearly established that the appearance of the first

and the second sublimation peaks coincide with the very quick and the

slower "darkening" of the particle, respectively. One must keep in mind,

however, that all this time between the first peak and the second peak,

the surface temperature remains fixed at zero degrees centigrade. The

coordination of all these observations as a function of time is shown

qaulitatively for a typical particle in Figure 22.

A careful interpretation of the extensive bulk of data has led to

the following detailed description of the freezing of a water drop in

vacuum, which ties all the pieces of information together in a consistent

way.

Referring back to Figure 22 six separate time intervals have been

designated for the convenience of description.

During time interval (1) the drop is in a supercooled state. The

sublimation rate is low, the surface temperature is low and the transparency

is high. During time interval (2) freezing has been initiated and rapid

dendritic growth extends through the drop and forms a cocoon around the

surface. As a result of the freezing, the surface temperature rises

suddenly to zero degrees centigrade, and the sublimation rate shows a

pronounced peak which can be attributed to an increase of the particle

temperature (and possibly through the expulsion of very small water

droplets (Ref. 13). In the moment of freezing the transparency of the

particle decreases drastically as a consequence of the presence of the

dendrites. At the end of the period (2) the sublimation rate drops to
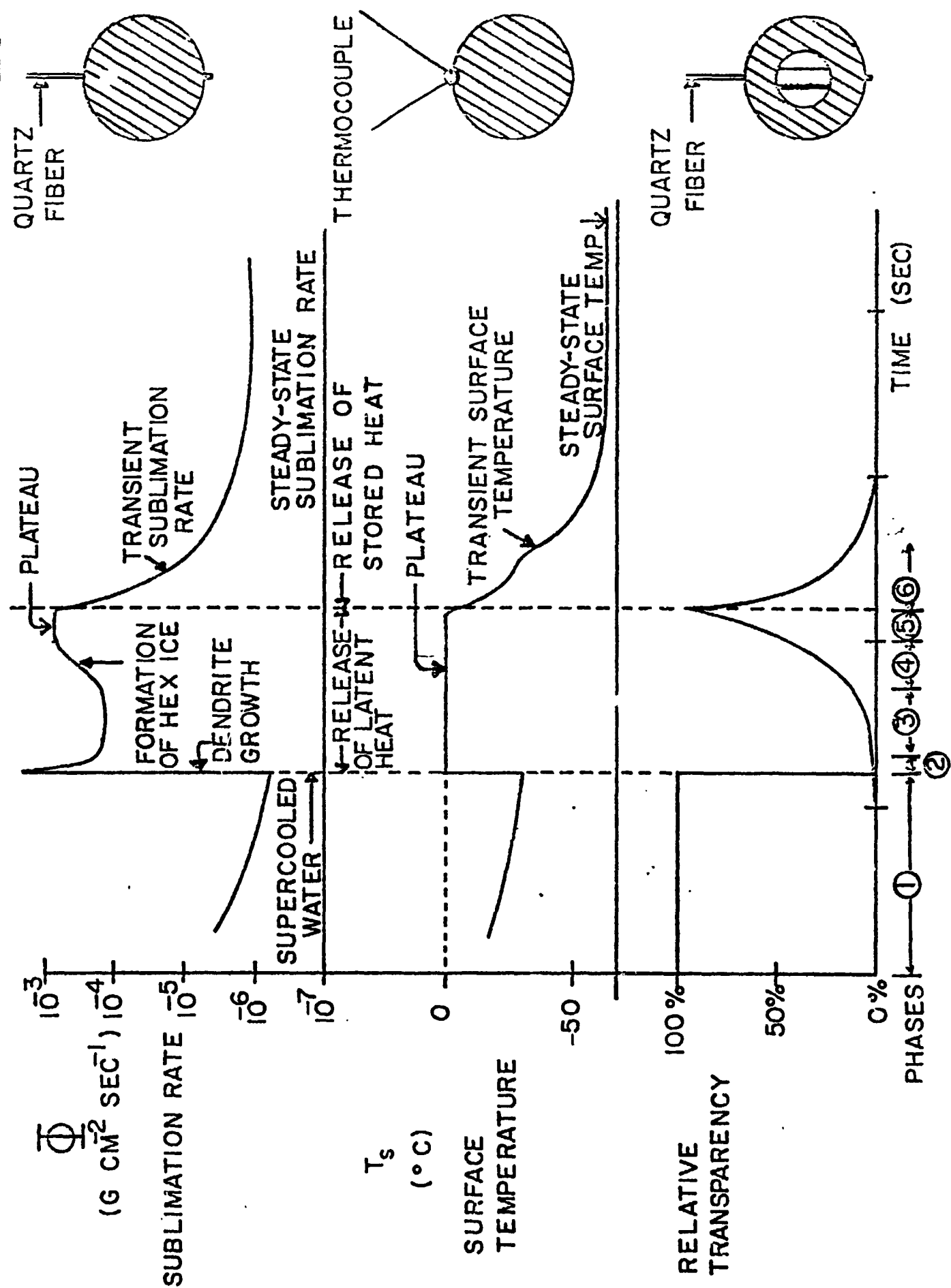
FIGURE 22. SYNCHRONIZATION OF SUBLIMATION RATE, SURFACE TEMPERATURE AND TRANSPARENCY DURING THE FREEZING PROCESS.

reach a minimum as one enters time interval (3). Since the surface

temperature remains constant, the sublimation rate during this time

period represents the sublimation rate of the dendritic surface material.

At the end of period (3), an increase of the transparency can be noted.

The duration of the time interval (3) varies greatly from run to run

depending upon the perfection of the dendritic shell. As the thickness

of the shell increases, tremendous pressure is being built up in the liquid

interior which will remelt the dendrites in the interior and replaces the

interior dendritic ice with an increase of the thickness of the surface

shell. This new ice growth, however, is relatively slow compared to the

rapid initial dendritic growth, and as a consequence, the appropriate

crystal habit consists of normal hexagonal ice grains. The above mentioned

increase in transparency during step (3) occurs when the growth of the

shell is no longer accommodated by the disappearance of the interior ice,

resulting in an increase of pressure which transports the rest of the

interior water along the grain boundaries of the hexagonal crystals and

through the pores of the fibrous dendritic network. The droplet does not

crack because the surrounding fiber structure with its enormous tensile

strength holds it together. As this process progresses, the particle

becomes increasingly more transparent. The water squeezed to the surface will

crystallize as soon as the pressure is released after its escape through

the pores. As a consequence, the ratio of dendritic ice to normal hexagonal

ice at the surface decreases steadily, and the sublimation rate changes

from that of the dendritic structure to the one of hexagonal ice (step 4). The

burial of the fibers in the hexagonal structure completes period (4).

During period (5), the sublimation rate stays at a plateau until all the

latent heat is dissipated, and the particle is completely frozen. A fast

drop of both the surface temperature and the sublimation rate initiates

period (6). The ice particle becomes opaque again as there is no water

left to reduce scattering between grain boundaries. A pictorial represen-

tation of the important freezing steps as they manifest themselves optically

is shown in Figure 23.

3.2.3.1.4 Calculation of the Evaporation Coefficient - Two sets of

reliable data have been obtained for the same size particles freezing under

the same environmental conditions. It should be pointed out that the shroud

temperature in these experiments was varied from $296^{\circ}K$ to $273.^{\circ}K$. However,

the influence of the shroud temperature can only affect the cooling of the

particle near the steady state temperature. In this vicinity there is also

a perturbation due to the heat conduction through the quartz fiber or

through the thermocouple wires. The perturbation is effective in the

vicinity of the steady state condition because the temperature difference

between the particle and its surroundings is largest and so is the time

available for heat transfer. During freezing, however, and the period of

rapid cooling after freezing, neither the temperature differentials nor

the available interaction times are sufficient to cause a significant

perturbation. During the period where the surface temperature is at zero

degrees, and during the time when the temperature is changing rapidly,

the enery dissipated by sublimation overwhelms by far the perturbing

OPTICAL APPEARANCE

TRANSPARENT   SUPERCOOLED WATER

OPAQUE   DENDRITES
(FAST GROWTH)

WATER

PARTIALLY
TRANSPARENT   HEXAGONAL ICE
(SLOW GROWTH)

WATER FLOW

OPAQUE   HEXAGONAL ICE
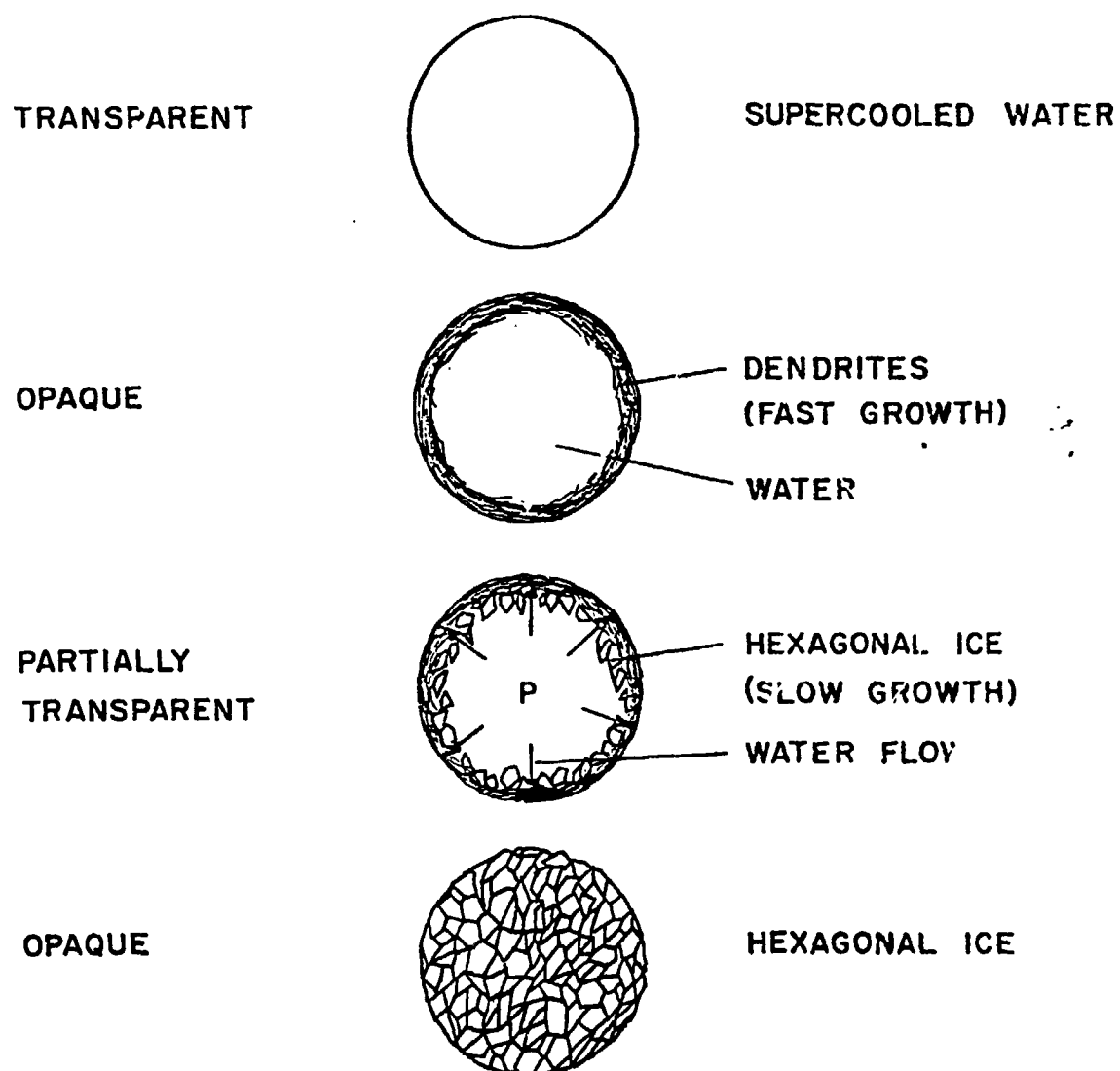
Figure 23
Pictorial Representation of the Optical Appearance of a Freezing
Droplet

influences of radiative heat exchange and thermal conduction through the

measurement probes. An extension of the data into the region of slow

temperature change, close to the steady state condition, requires

corrections especially for the highly sensitive surface temperature data

which at this moment cannot be provided with certainty. Since the steady

state reading of the thermocouple is about $200^{\circ}K$ it was decided to discard

the temperature values below $210^{\circ}K$ corresponding to a time interval of

about one second after the initiation of cooling.

Since both surface temperature and sublimation rate are functions

of time, sublimation rate as a function of surface temperature can be

obtained by synchronizing both curves at the point where the particle

starts to cool down from the zero degree plateau. Since the definition of

the evaporation coefficient is

$$\alpha (T_s) = \frac{\dot{\phi}_{exp} (T_s)}{\dot{\phi}_{th} (T_s)} \qquad (10)$$

$\alpha(T)$ is readily calculated from the data contained in Figures 20 and 21.

The result is shown in Figure 24 together with α values of several other

experimenters. A survey of the literature certainly confirms that the data

presented in Figure 24 represents the most detailed study over the largest

temperature range ever attempted.

3.2.3.1.5 Interpretation of the Evaporation Coefficient - The

evaporation coefficient is shown as a function of $10^3/T$ in Figure 25 in a

Figure 24
Evaporation Coefficient vs. Temperature

58
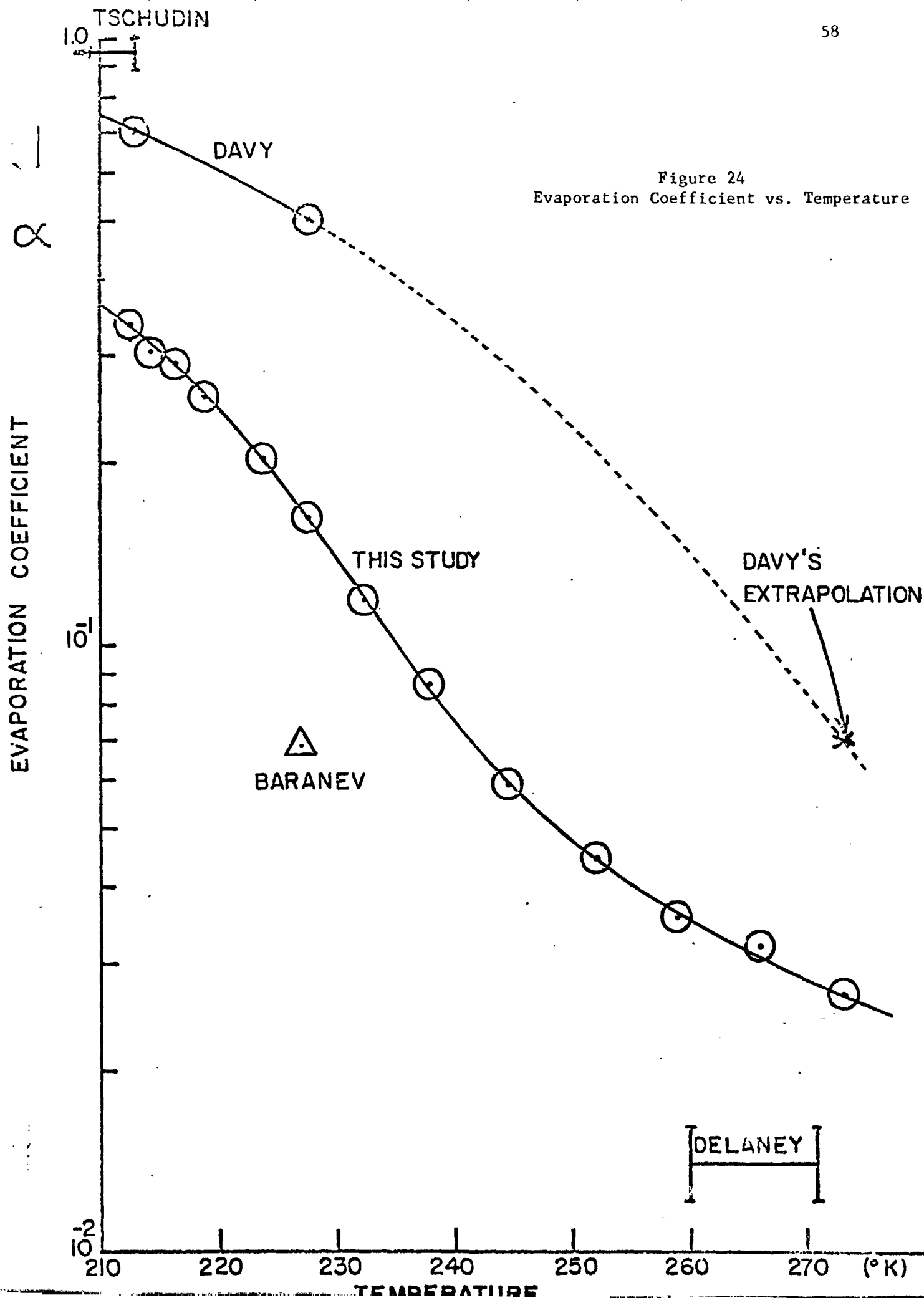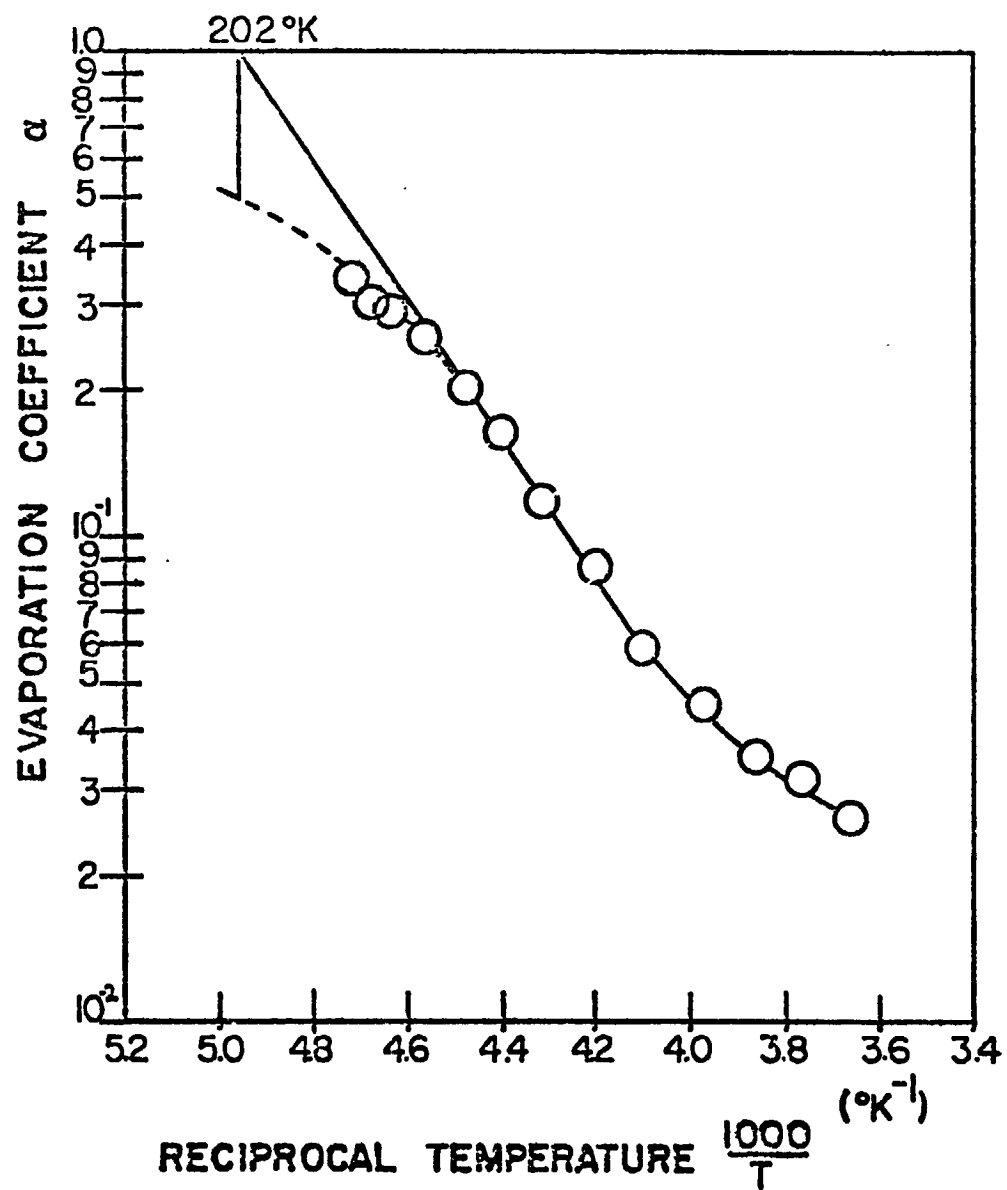
Figure 25
Evaporation Coefficient vs. Reciprocal Temperature

semilogrithmetic plot. It follows a general exponential behavior previously not recognized. A deviation from the exponential behavior is evident at lower temperatures where the evaporation coefficient converges toward unity. The intercept of the exponentially extrapolated curve intercepts the value $\alpha = 1.0$ at a temperature of $T_o = 202^{\circ}K$. The extrapolation of the data points leads to a value of about 0.5 at this temperature.

Although the details of the nature of the ice surface are unknown, it is worth noting that the type of behavior described above is similar to that of a Fermi distribution function. The Fermi distribution represents the probability for the occupancy of an energy state through the introduction of the Fermi level, ε_f. If the Fermi level is above the state, the occupancy is one, if it is below, the occupancy decreases exponentially with the depression of the Fermi level. When the Fermi level crosses the state level, the occupancy is 0.5 if the statistical weight factor, γ, of the state is unity. According to this description of α one can write:

$$\alpha(T_s) = \frac{1}{e^{(E-\varepsilon_f(T)/kT_s}+1} = \frac{1}{e^{\Delta\varepsilon/kT_s}+1} \qquad (11)$$

Where E represents the energy of the state under consideration. If $\Delta\varepsilon$ is developed into a Taylor series in the vicinity of T_o one has

$$\Delta\varepsilon = \frac{\partial \varepsilon_f}{\partial T}(T-T_o) + \cdots \qquad (12)$$

and equation (11) becomes:

$$\alpha = \frac{1}{\gamma e^{\frac{1}{k}\frac{\partial \varepsilon_f}{\partial T}\frac{(T-T_o)}{T}}+1} \qquad (13)$$

For $T < T_o$, one can recognize that α coverages toward one as expected.

For $T = T_o$

$$\alpha = \frac{1}{\gamma + 1} = \frac{1}{2} \qquad \text{for } \gamma = 1 \qquad (14)$$

as found by extrapolation of the data.

For $T > T_o$, however, the addition of one in the denominator can be neglected and $\alpha(T)$ becomes an exponentially decreasing function of temperature, as observed experimentally.

$$\alpha(T) \approx \frac{1}{\gamma} e^{-\left(\frac{1}{k} \frac{\partial \varepsilon_f}{\partial T} \frac{T - T_o}{T} \right)} \qquad (T > T_o) \qquad (15)$$

The apparent campatability of a Fermi distribution with the temperature dependence of α suggests an interpretation of α as a relative concentration of molecules at the ice surface ready for evaporation. At low temperature the surface concentration of these molecules is equivalent to their equilibrium concentration. As the sublimation rate increases with increasing temperature, the concentration of these particular surface molecules declines in respect to the equilibrium concentration because of decreasing supply. A decreased relative surface concentration as a result of an inability of the surface diffusion and/or generation rate to supply these molecules, leads to a reduction of the sublimation rate compared to the rate predicted from equilibrium considerations.

In conclusion one can say that the investigation of the evaporation
coefficient has yielded not only the temperature dependence of this
quantity, but has also by its functional dependence, led to an interpretation
of the evaporation coefficient as a relative surface concentration which
can be represented by a Fermi distribution. Therefore the definition of α as

$$\alpha = \frac{\phi_{exp}}{\phi_{th}}$$

is directly linked to the relative surface concentration of water molecules
ready for evaporation.

3.2.3.1.6 'The Sublimation Rate of Ice as a Function of Surface
Temperature - The correlation of the sublimation rate as a function of time
(Figure 21) with the surface temperature as a function of time (Figure 20)
yields the sublimation rate as a function of surface temperature which is
shown together with the theoretical sublimation rate in Figure 26. Note
the convergence of the experimental sublimation rate toward the theoretical
rate at the lower temperatures. Near the melting point, however, the
experimental sublimation rate is nearly two orders of magnitude below the
theoretical rate ($\alpha \approx 0.027$).

Figure 26
Comparison of Experimental and
Theoretical Sublimation Rates
vs. Temperature
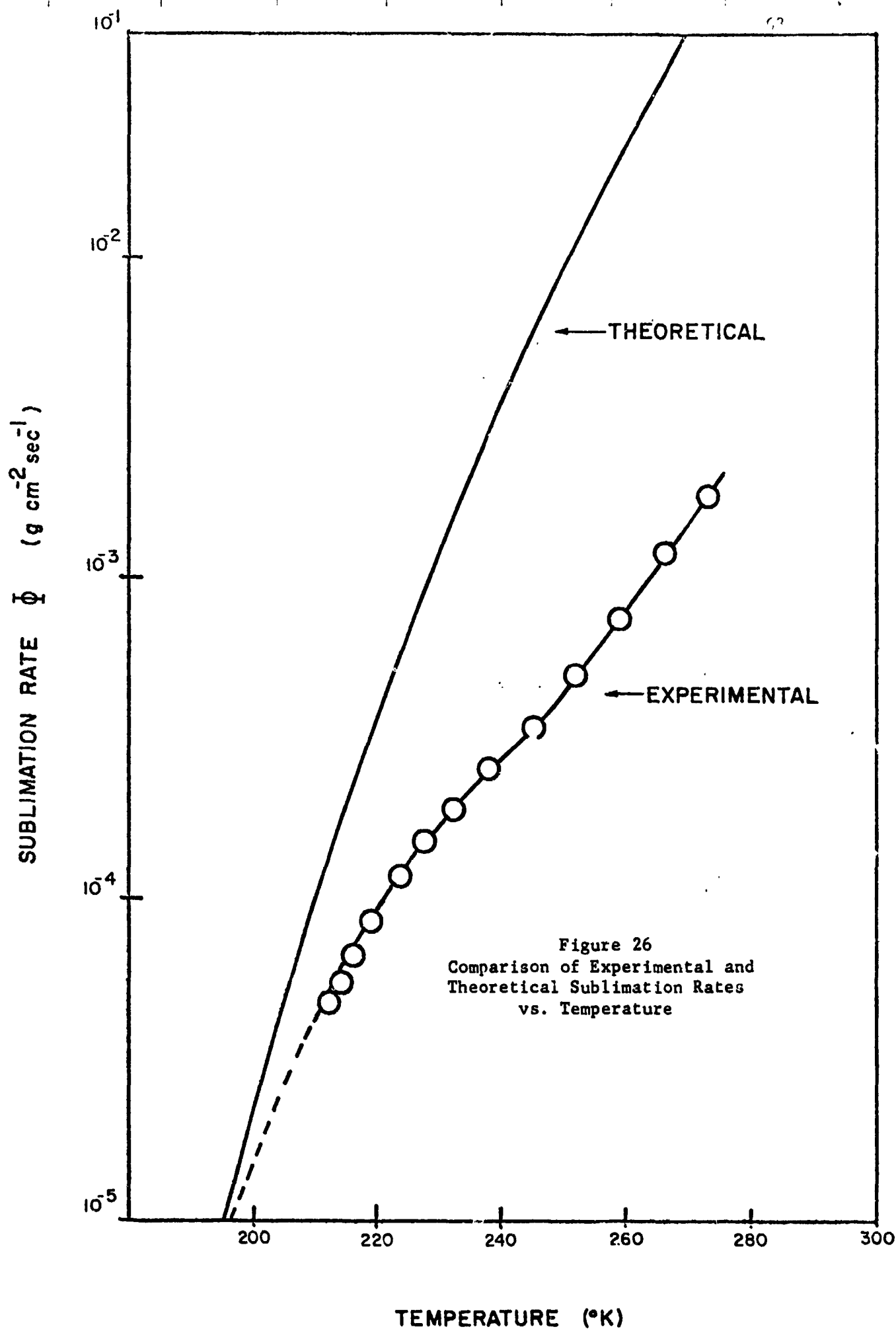
3.2.3.1.7 <u>Can Liquid Water Exist on Comets?</u> - The presence of oxidized iron in chondridic meteorites suggests the presence of liquid water at some stage during their development. If chondritic material is cometary in origin, then the possibility of liquid water existing during a solar passage should be explored. With the above data, one can now estimate an approximate solar distance, where the melting point of ice is reached. Using the theoretical sublimation rate, a distance of about 0.03 A. U. or less than 7 solar radii would appear to be necessary. If one uses the experimental sublimation data, a distance of about 0.2 A.U. is sufficient. Of course many more comets have perihelion distance; within 0.2 A.U. compared to those which pass within 7 solar radii.

3.2.3.2 <u>The Sublimation Rate of Pure Ice Particles under Solar Simulation</u> - After having studied the sublimation rate of ice in vacuum as a function of surface temperature, it would appear that all that one has to do to predict the sublimation rate of ice particles in space is to choose a reasonable value for the albedo and to perform a trivial calculation of the sublimation rate as a function of the distance from the sun. The result of this calculation would yield a constant sublimation rate for each solar distance independent of particle size. In fact this is the standard procedure in comet literature to date. The question arises: Is there any point for further thought or experimental investigation? Without taking such tradition-steeped physics for granted, a study of the sublimation rate of individual ice particles was conducted under solar simulation. At the same time a theoretical study was carried out.

The results of the experimental runs of sublimation rate versus ice particle radius are shown in Figure 27. The radiation flux at the particle from the xenon arc lamp was 189 mw/cm^2 and the walls surrounding the ice particle were at liquid nitrogen temperature. One can note that particles with decreasing radius show a decrease in sublimation ra'-. These sublimation rates, however, should not be taken to represent the sublimation rates under solar illumination because of the difference in the spectral distribution between the xenon arc lamp and the sun. The ice particles were spherical and relatively smooth but varied slightly in respect to surface scattering. No major influence of surface scattering ou the sublimation rate has been noticed. Nevertheless a study to assess the influence of surface scattering on the sublimation rate was initiated. The results are reported in the next section (3.2.3.3).

Figure 27 indicates that with decreasing particle radius the sublimation rate becomes smaller. An obvious question arises: does this trend continue so that one is left with ice particles which never disappear? Experimentally. the pursuit of measurements with ice particles of radii smaller than those reported here is an extremely difficult task due to severe handling problems on fine fibers. However, as will be seen in sections 3.3.2.5, 3.3.2.6 the agreement between theoretical expectations and experimental results allows an answer to this question by theoretical means.

In order to compare these experimental results with theoretical calculations it is necessary to introduce complex index of refraction data in che computations. Another experiment on pure ice has been carried out
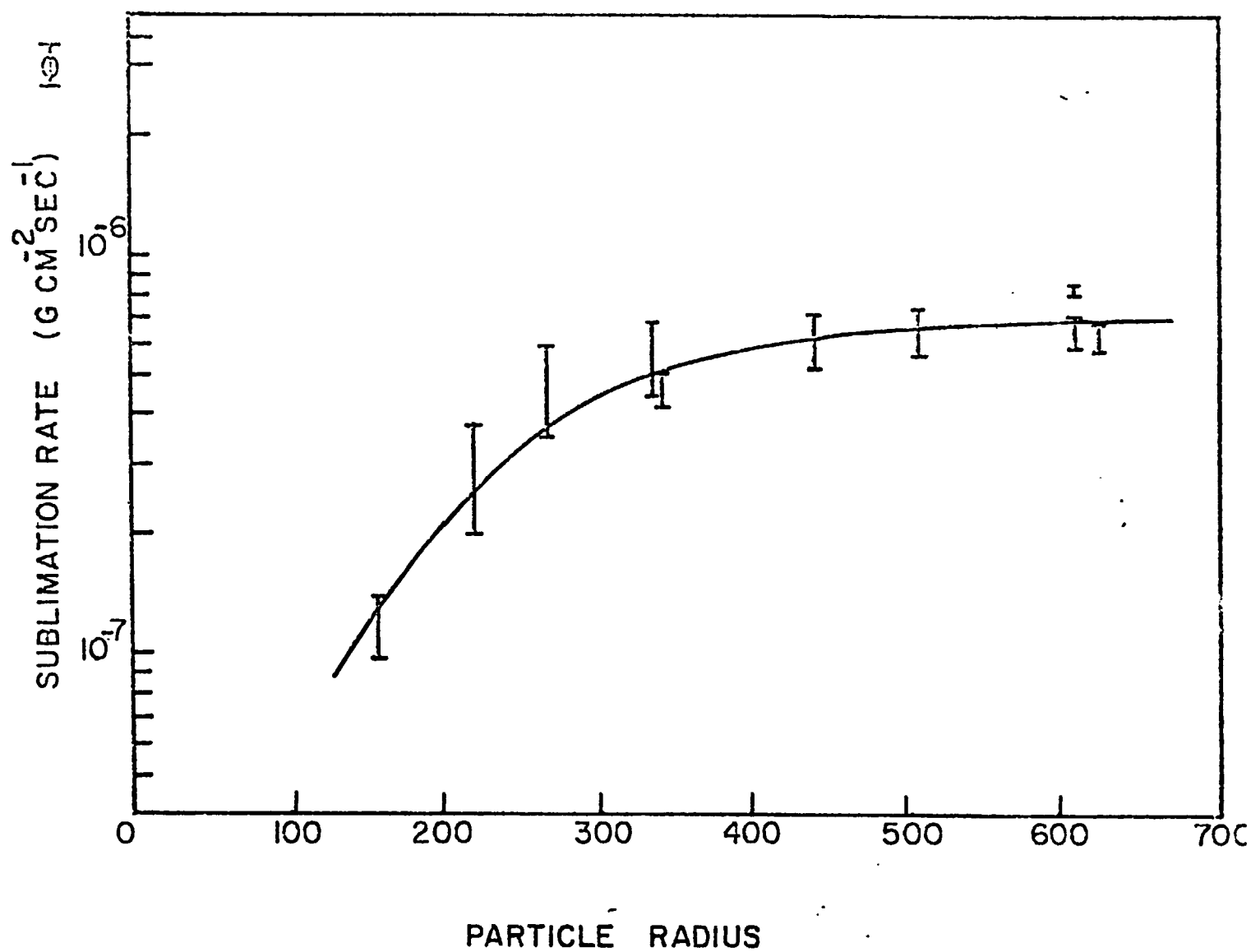
Figure 27
Sublimation Rate vs. Particle Radius
Under Solar Simulation (189 mw cm^{-2})

which provides a means to discriminate between different sources for
the complex index of refraction available in the literature. The results
of this experiment can be presented more clearly in conjunction with the
calculations of the sublimation rate of ice particles in space, where the
necessity for this additional experiment first became apparent (Section 3.3.2.4).

3.2.3.3 <u>The Effect of Surface Roughness and Light Scattering on</u>
<u>the Sublimation Rate</u> - It has been observed during experimentation that
ice particles develop a rough surface under vacuum conditions (ref. 9).
In the course of the present work it was observed that two different degrees
of surface roughness occur when ice particles sublimate in a vacuum. A
severe surface roughness develops when the water from which the ice particles
are made is saturated with air. If, however, the water is boiled immediately
before freezing, the particle surface tends to remain relatively smooth.
An example is shown in Figure 28.

In order to assess the influence of surface roughness on the
sublimation rate for pure ice, a core-mantle type particle was examined.
A blackened sphere 318 μm in radius was placed on the end of the fiber.
An ice mantle was formed around this core. Two typical examples are shown
in Figure 29. Both ice mantles are of about the same size but have different
scattering properties. In this arrangement virtually all the light from
the solar simulation impinging on the core is absorbed and contributes to
the sublimation process. A second series of runs was conducted where the
core was coated with aluminum. In this case a core with a high reflectivity
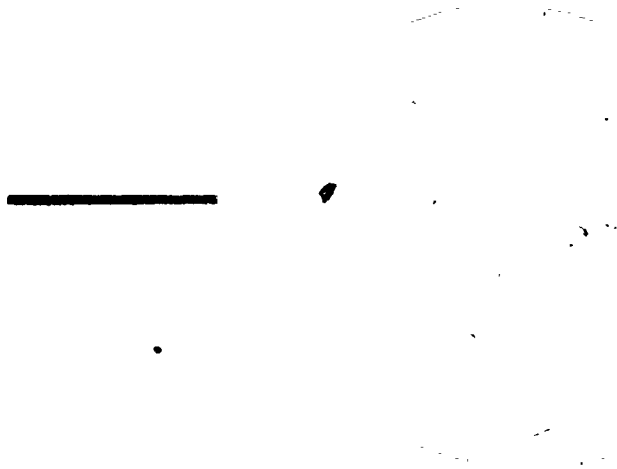was obtained. The resulting sublimation rates of both cases under solar

Figure 28 – Comparison of Particles Made with Degassed Water (left) and Air-saturated Water (right) (50X)

Figure 29 – Visual Appearance of Core-Mantle Ice Particles (6X)

simulation at 170 mw cm^{-2} are shown in Figure 30. For comparison, the

sublimation of ice spheres without a core have rates in the region of

10^{-7} g cm^{-2} sec^{-1} for this radiant flux and these particle sizes. In

the case of the black body core, a number of mantle sizes varying over a rel-

atively wide range have been investigated. One can notice that the

sublimation rate increases with decreasing particle radius. This can be

attributed to the fact that the core is the major absorber of radiative

energy which is dissipated at the ice mantle surface. For smaller particle

radii a smaller surface area is available for this energy dissipation and

consequently the sublimation rate must increase. The effects of different

amounts of scattering for particles of the same size show up in sublimation

rate differences. As an example, the experimental points in Figure 30

labeled A and B correspond to results of sublimation measurements of the

particles labeled A and B in Figure 29. The indication is that less light

is reaching the core of particle B resulting in a slightly lower sublimation

rate than that observed for particle A. In Figure 30 the theoretical

sublimation rate for a black body core particle without scattering is

shown as a dotted line for comparison.

It is interesting to note that the presence of the highly reflecting

aluminum core has a greater influence than one would intuitively expect.

With all its reflectivity the aluminum core still allows the sublimation

rate to come within 50% of the black body core results.

For the power flux as used in these experiments, the experimental

situation can best be described as follows: the power absorbed by the

Figure 30

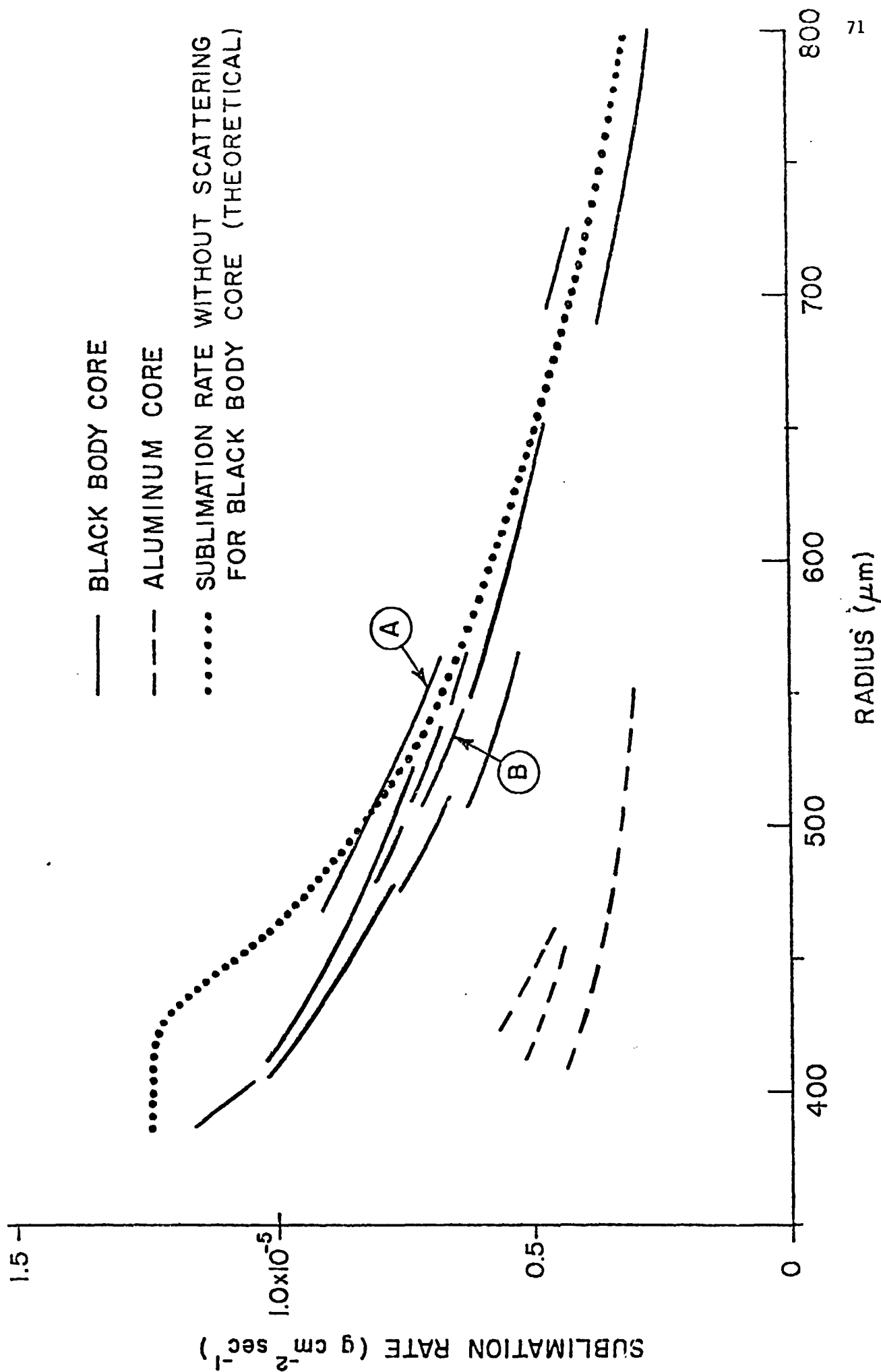Sublimation Rate vs. Particle Radius for Core-Mantle Ice Particles

Legend:

—— BLACK BODY CORE

– – – ALUMINUM CORE

•••••• SUBLIMATION RATE WITHOUT SCATTERING
FOR BLACK BODY CORE (THEORETICAL)

Axes: SUBLIMATION RATE (g cm^{-2} sec^{-1}) vs. RADIUS (μm)

particle is mainly funneled into the sublimation process. The power
of the outgoing radiation is of long wavelength and therefore almost
independent of scattering. Therefore the change in sublimation rate
between runs of a given core material can be solely attributed to a
change in absorption at the core which is caused by the scattering effect.
The core mantle experiment should be viewed as a means for assessing the
effect of scattering on the sublimation rate of a pure ice particle. This
core mantle experiment is really a worst case estimate in view of the fact
that the particle is being forced to be sensitive to the short wavelength
(visible) radiation where pure ice particles do not absorb efficiently
and yet where scattering has its greatest influence.

In conclusion, one can state that although the effect of scattering
is very prominent visually, its effect on the sublimation rate of ice
particles in space is a relatively small perturbation. As a rule of thumb
the effect of an absorbing impurity in the optical window of ice
is more important than the effect of scattering.

3.2.3.4 <u>Sublimation Rates in the Presence of Impurities</u> - Comets
are believed to contain particulate material intermixed with ice. It is
therefore of interest to examine the behavior of ice and ice particles
under solar illumination containing different types of particulate impurities.
Out of an unlimited number of possibilities, three substances have been
selected. The selection was guided by the aim to obtain representative
substances of widely diverse optical properties. For an initial pilot
investigation, charcoal power, aluminum microspheres and aluminum oxide
powder were introduced into ice particles at varying concentrations.

Charcoal powder does not scatter but absorbs without preference over the entire spectral region. Three different concentrations have been introduced into water to make a slurry from which the ice particles were generated. The distributions for these concentrations are shown in Figure 31. The results of sublimation rate measurements are shown in Figure 32 for the three distributions A, B, and C. As expected, the higher the carbon concentration the higher the sublimation rate. For comparison the sublimation rate of pure water for the same particle size is plotted.

Aluminum microspheres were examined in the same manner. Their particle size distribution is shown in Figure 31, and the sublimation rates obtained with these distributions are shown in Figure 32. Aluminum spheres are absorbing in the near ultraviolet and scattering in the visible region of the spectrum, while the absorptivity decreases with increasing wavelength. As in the case of the charcoal powder, the sublimation rate increases with increasing particle concentrations.

Aluminum oxide, on the other hand, is characterized by its strong light scattering capability in the visible part of the spectrum. Al_2O_3 powder absorbs in the infrared but shows virtually no absorption in the visible. Three concentrations of $0.05 \mu m Al_2O_3$ powder were examined with normalities of 0.125N, 0.25N and 0.5N. The results are also shown in Figure 32. The introduction of the powder has virtually no effect on the sublimation rate compared to pure water.

As an example how the powder of an arbitrary substance will influence the sublimation rate of ice particles, a slurry was made from chondritic
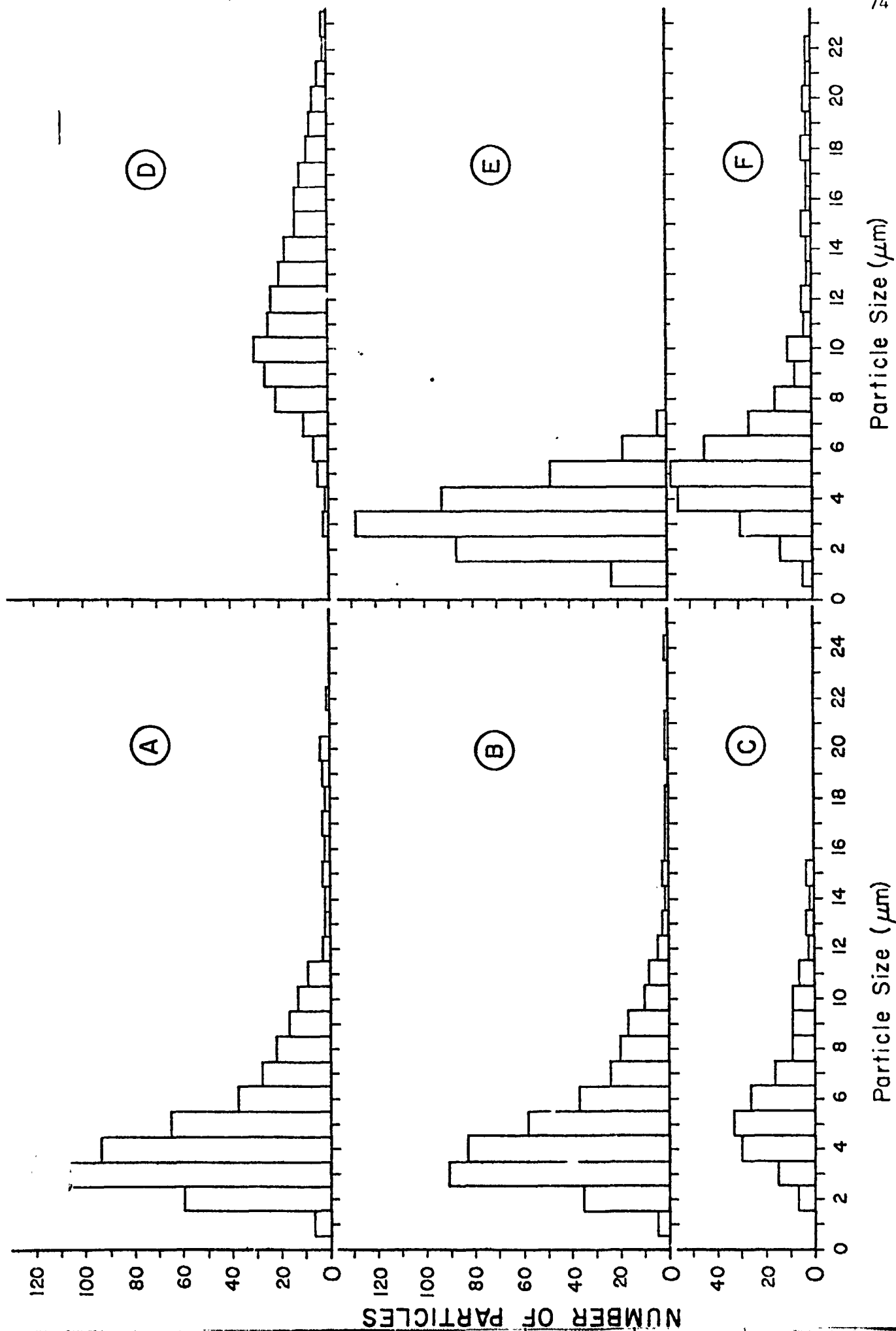
ALUMINUM MICROSPHERES

CHARCOAL PARTICLES

Figure 31
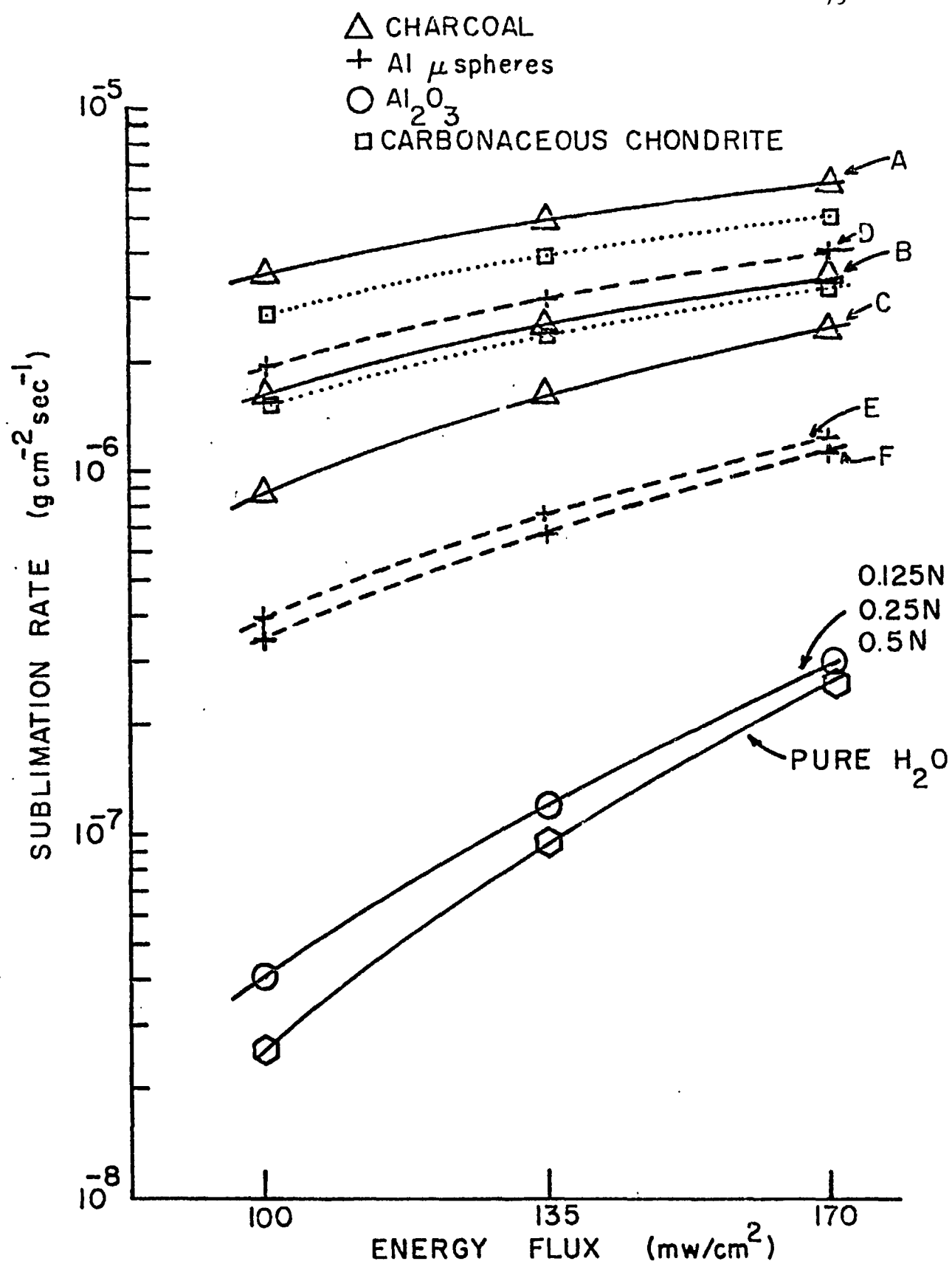Particulate Impurity Size Distributions

Figure 32
Sublimation Rate vs. Energy Flux for Various
Particulate Impurities in Ice

material. The same concentration as the two heavier concentrations of charcoal were investigated. As one would anticipate, the resulting sublimation rates are slightly below the _esults for charcoal.

During these preliminary investigations of particulates in ice, it became apparent that a meaningful study of the effects of particulate impurities can only be conducted if the important parameters such as concentration and particle size distribution are specifically given. In this case a prediction of the sublimation rate can be achieved through the measurement and the introduction of an effective index of refraction as a function of wavelength. This approach is discussed in Section 3.2.3.7.

3.2.3.5 Effects of Particulate Contamination on the Surface Structure of Ice - From the previous runs an interesting result was obtained in respect to the effect of the particulates on the surface structure of the ice particles.

Aside from influencing the sublimation rate, particles imbedded in the ice have been observed to produce structural changes on the ice surface when exposed to solar radiation. The degree of surface change seems to have a correlation to the absorption properties of the particulate matter. In Figure 33 these effects are shown. Aluminum oxide produces a rather smooth surface structure, while for the aluminum microspheres, some surface roughening is clearly evident. For charcoal power, a completely erroded dendritic-like surface structure results. It is interesting to note that the degree of surface roughening seems to increase as the impurity particle becomes more absorbing in the visible range. When viewing the surfaces

Figure 23 - Surface Structure of Ice under Solar Simulation with Different Particulate Impurities

under the microscope, the surface with aluminum oxide shows little

observable change while for the ice with charcoal impurities, the surface

is bustling with activity. One can observe dendrities in rapid motions;

bending, twisting, and being ejected. These observations have been made

at radiant flux levels equivalent to one solar constant. A motion picture

of a charcoal doped ice surface has been taken. One of the interesting

features is the record of the ejection of a 90 μm diameter ice grain in a

horizontal direction. Three successive frames of the motion picutre are

shown in Figure 34. The first picture (bottom) shows the ice surface

before the event. The second frame (middle) records the trajectory of the

ice grain as it was ejected, and the third frame (top) shows the surface

after the event. Since the trajectory starts out originally in a horizontal

direction, a simple analysis of the resulting parabolic curve yields an

ejection velocity of 24 cm sec^{-1}. A visual count of about 2 particles

cm^{-2} sec^{-1} was made. This observation suggests a possible mechanism for

the introduction of large ice grains into comet comas requiring only the

presence of embedded particulate matter absorbing in the visible range.

3.2.3.6 Impurities in the Optical Window of Ice - There is an

inexhaustible number of substances and combinations of substances which

might exist in the matrix of cometary ice grains. How is one going to

make a meaningful statement as to the effect of such innumerable possibilities

on the sublimation rates? A pedestrian approach which would examine the

sublimation rates of ice particles mixed with a great number of different

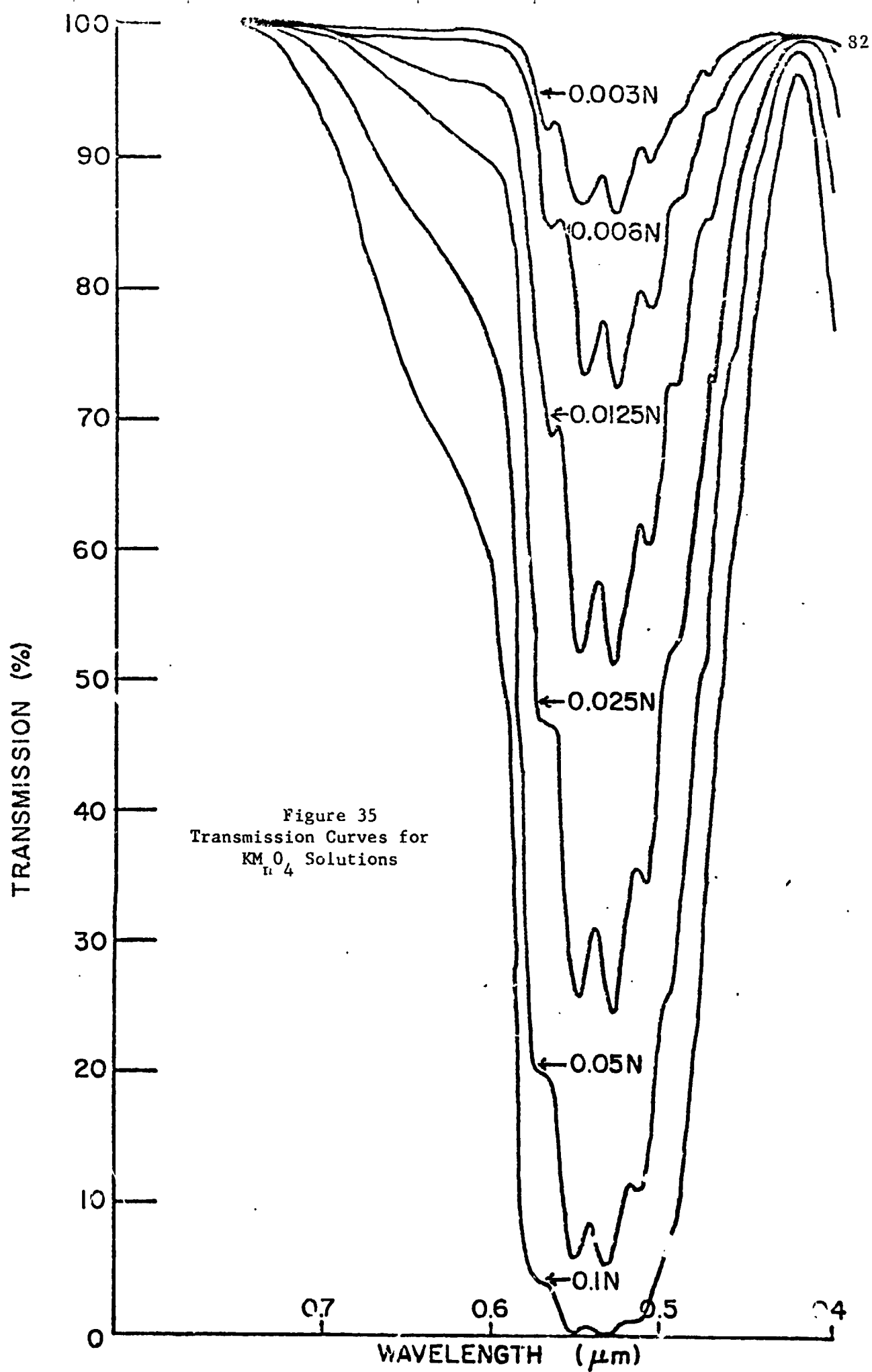materials with different morphologies at different ice grain sizes at

different solar distances is not only impractical but would not lead to results which could be used in a manageable way to analyze photometric profiles of comets. What is needed, instead, is a way in which basic parameters can be varied in a model so that the results can be compared directly to observations. Once a set of parameters has been established which achieves agreement with observations, one can then conduct a meaningful search for those substances which yield this set of parameters.

What are those parameters? The sublimation rate of an ice particle is dependent upon the power it can absorb. The results of the measurements with the powders, particularily those for aluminum oxide, clearly demonstrates that particles whose absorptivity is in the same spectral region where ice absorbs heavily, i.e. the infrared, have little effect on the sublimation rate. Consequently only impurities which absorb in the optical window of ice can effectively alter the sublimation rate. The problem to determine the influence of the impurities on the sublimation rate of ice boils down to the task to determine the change of the absorption of the contaminated ice in the ice window region.

3.2.3.7 Determination of an Effective Complex Index of Refraction

In order to deveop a model to treat the sublimation rate of nonhomogenious ice particles in the solar system, it is necessary to introduce the concept of an effective complex index of refraction. Since the real part is hardly changed by small to moderate amounts of impurities, once can in this case restrict oneself to the consideration of the imaginary part, $n''(\lambda)$, which is the primary parameter for the absorption of an ice particle. The effective imaginary part of the complex index of refraction, $n''_{eff}(\lambda)$, is

defined as the value which when introduced into scattering theory calculations at a particular wavelength, will yield the absorption efficiency of the composite ice particle. $n''_{eff}(\lambda)$ can be obtained from equation (7) when the measured experimental value of the sublimation rate is introduced. It is also apparent from equation (7) that these measurements should be carried out with monochromatic radiation. In a sense, the measurement of the sublimation rate represents an absolute determination of the absorbed power and therefore of the absorption efficiency which yields the effective imaginary part of the complex index of refraction. Unfortunately the present experimental setup does not have the appropriate optics to provide sufficient power for monochromatic measurements. However, the procedure can be demonstrated experimentally in the following way: an impurity with a narrow band absorption in the optical window is introduced into the ice. By this means the power imput into this particular spectral region is preferentially increased. It should be possible, therefore, to invoke equation (7) to determine the effective value of the imaginary part of the complex index of refraction for the narrow wavelength region where the added impurity absorbs. In the case of a soluble impurity, n''_{eff} is equal to the actual n'' of the solution if there is no scattering involved. In the presence of light scattering, these two values will differ. As an absorbing medium in the window region, potassium permanganate has been chosen. Transmission curves for $KMnO_4$ solutions in a cell 0.0127 cm thick are shown in Figure 35. From a 0.005 N solution a drop was frozen at the end of the fiber and placed into the microbalance. The microbalance chamber

Figure 35
Transmission Curves for
KM_nO_4 Solutions

0.003N

0.006N

0.0125N

0.025N

0.05N

0.1N

82

TRANSMISSION (%)

WAVELENGTH (μm)

0.7   0.6   0.5   0.4

was evacuated and the walls of the chamber were cooled to liquid nitrogen temperature. The xenon arc lamp was used for illumination along with a filter which eliminated radiation below $0.4 \mu m$. By use of this filter the increase of the absorption of $KMnO_4$ in the near ultraviolet was effectively neutralized, and as a result, the impurity in the ice particle produced a narrow band absorption in the ice window region. The sublimation rate of the ice particle was determined and a calculation was carried out to determine the value for n''_{eff} in this wavelength region. The calculation assumes a bandwidth of $0.1 \mu m$. The result for n''_{eff} is shown in Figure 36 in comparison to the values of n'' as obtained from the transmission curves.

As pointed out above, an agreement between n'' and n''_{eff} can only be expected when no scattering is present. Therefore, this technique can become extremely valuable when scattering centers exist in the ice. If one adds aluminum oxide powder to the potassium permanganate solution to increase the light scattering in the ice particle, a different n''_{eff} can be anticipated. In this situation, however, a transmission curve will no longer yield the absorptivity, but an extinction coefficient, a mixture of scattering and absorption, which is not readily related to the absorbed power. In Figure 37, an extinction curve for a 0.005 N $KMnO_4$, 0.5 N Al_2O_3 slurry is shown together with the extinction curve for the 0.5N non-absorbing Al_2O_3 slurry. Given this optical information even in combination with backscattering measurements (shown in the bottom half of Figure 37), it is a major undertaking to reliably determine the power which is absorbed in this medium in a given particle. The
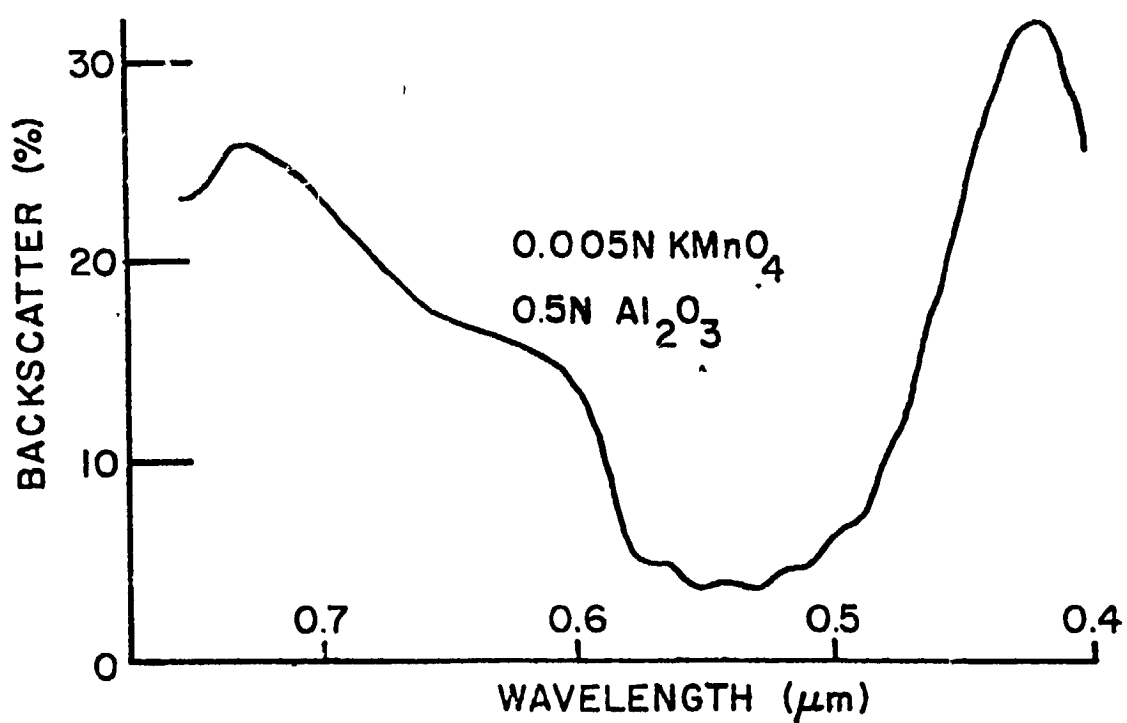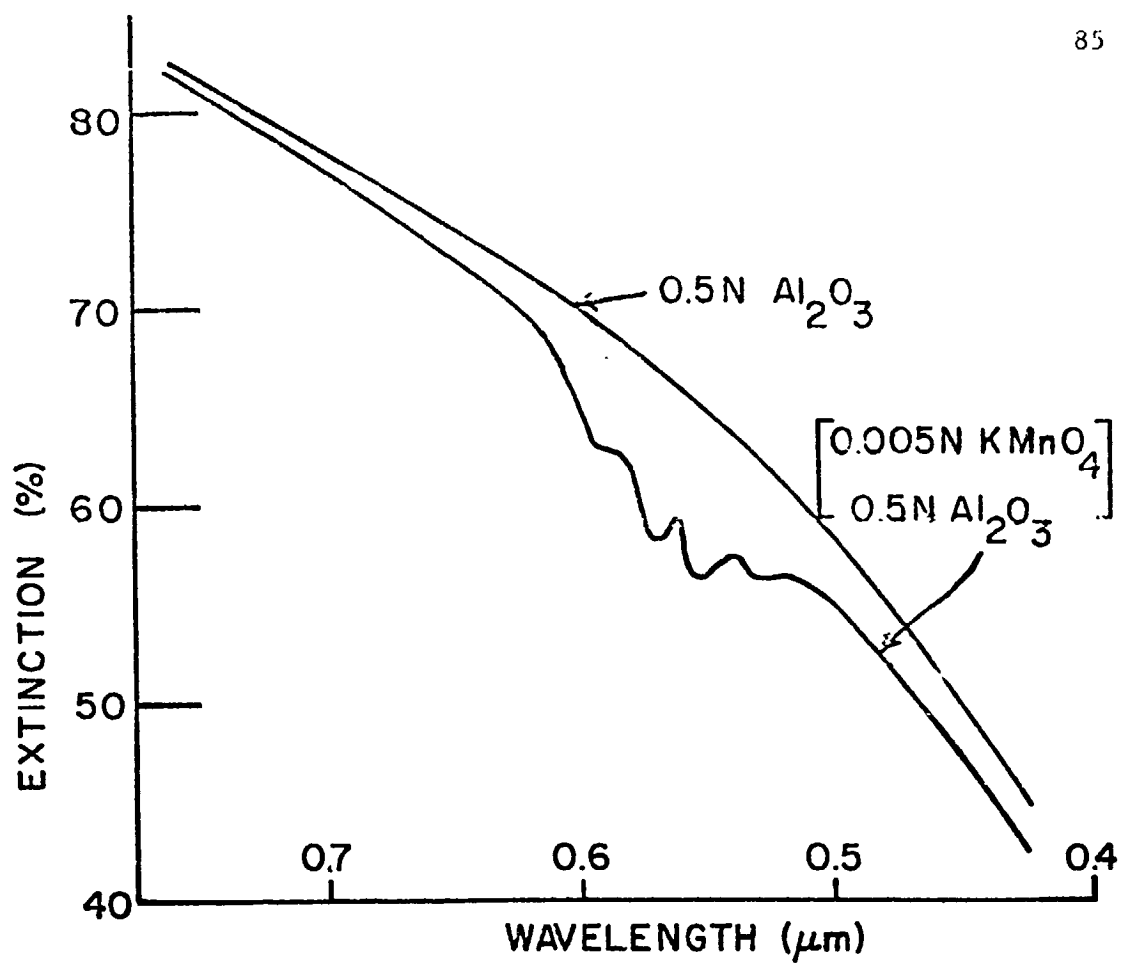
Figure 36
Comparison of Spectrometer and
Sublimation Measurements for N''
of KM_nO_4 in Water and Ice,
Respectively
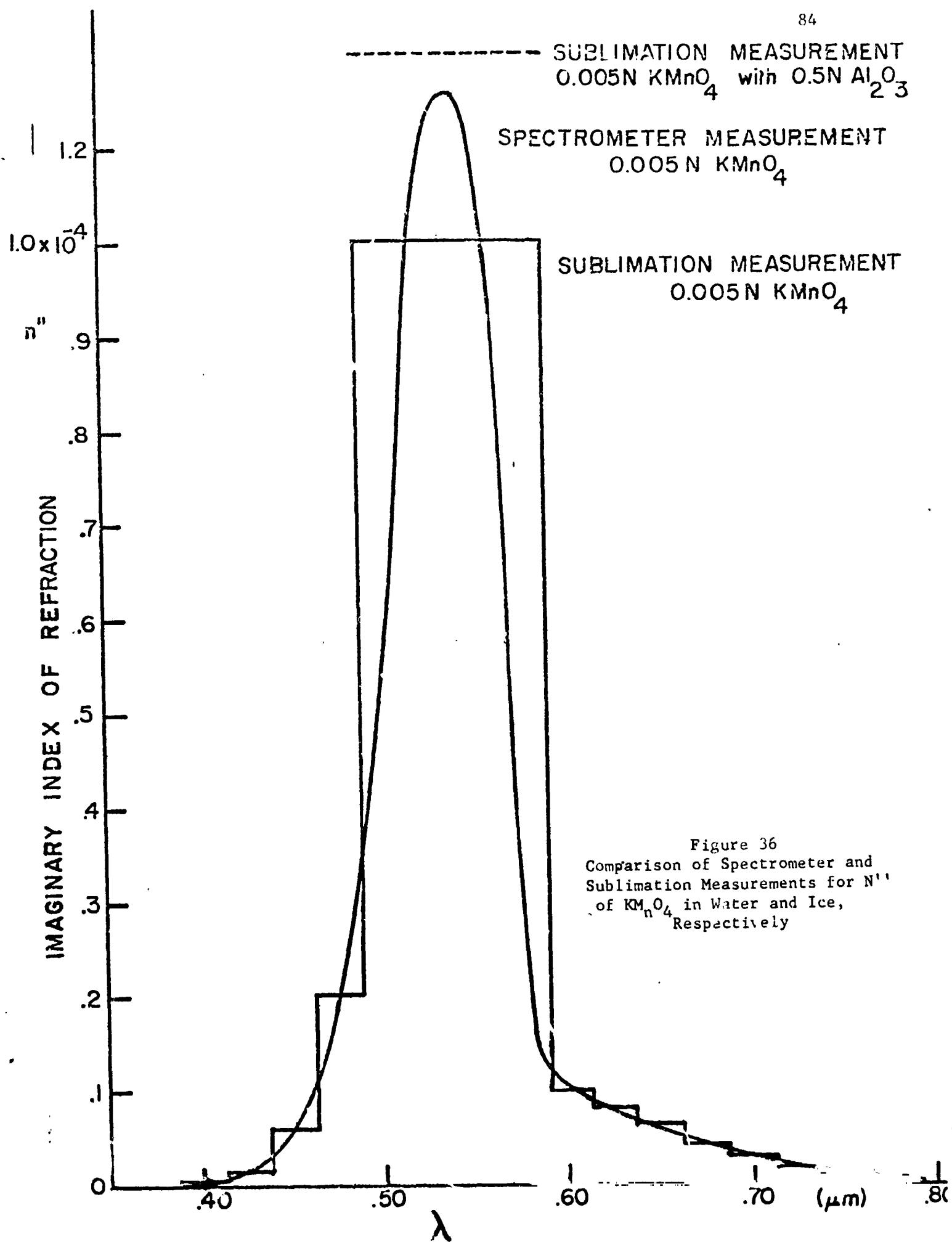
Figure 37
Extinction and Backscatter Measurements on Mixtures of KM_nO_4
and Al_2O_3 in Water

measurement of the sublimation rate, however, is a straight-forward approach. In Figure 36 the result of n''_{eff} for a particle formed from a mixture containing 0.005 N $KMnO_4$ and 0.5 N Al_2O_3 is shown. From these results one can conclude that a measurement of n''_{eff} as a function of wavelength for ice particles with impurities can be achieved through the use of monchromatic measurements of the sublimation rate. It would appear that this approach which measures the absorption of a particle directly is a unique optical technique which is potentially capable of establishing a parameterization through the use of n''_{eff} (λ) which can then be used to compute the sublimation rate of a given ice particle under given radiation conditions.

3.3 <u>Theoretical Calculations for Ice Particles Under Solar Radiation and Solar Simulation</u>

3.3.1 <u>Computer Program</u> - During the course of this contract a significantly improved version of a computer program which calculates the sublimation rates for ice particles in space has been developed. The input of the radiation field and the complex index of refraction can be introduced in any wavelength step size from the ultraviolet to the far infrared. For the present calculations on ice, the step sizes were chosen to be 0.1 μm from 0.2 to 5 μm, 1 μm steps in the wavelength range from 5 μm to 20 μm, 5 μm steps from 20 μm to 100 μm, and 10 μm steps from 100 μm to 350 μm. Index of refraction data from Irvine and Pollack (I. & P.) (Ref. 14) and Bertie, Labbe and Whalley (B.L.W.) (Ref. 15) have been used and compared.

The spectral distribution of the sun was approximated by a 5900°K

black body radiation. For particles with radius smaller than 100 μm
the absorption efficiency, Q, was computed using Mie theory when the
values of

$$| n* | \cdot x > 0.3 \qquad (16)$$

where

$$x = \frac{2 \pi r}{\lambda} . \qquad (17)$$

For

$$| n* | \cdot x < 0.3 \qquad (18)$$

the Rayleigh approximation was used. For particles greater than 100 μm
an approximation developed by Van de Hulst (Ref. 16, see also Plass, Ref. 17)
was employed. This approximation holds for dielectric spheres whose real
part of the complex index of refraction is close to unity.

3.3.2 Theoretical Predictions - In section 3.2.3.2 a question was
raised concerning the necessity to go beyond an albedo concept to describe
the sublimation properties of ice particles in space. The experimental
results shown in this section indicate a decrease of the sublimation rate
with decreasing particle size, but obviously a calculation using an albedo
for the ice particles would simply yield a constant, size independent
sublimation rate.

The computer program which has been assembled using the basic
physical equations from section 3.1 and scattering theory for the interaction
of the particles with the electromagnetic field should provide the answer
if the theory is adequately describing reality. Next to the theory itself
the input of the fundamental physical properties of the ice particles and

and the properties of the radiation field are the most essential

ingredients. These critical inputs are the complex index of refraction

of ice and the spectral distribution of the radiation field.

3.3.2.1 <u>The Optical Properties of Ice</u> - There are two major sources

for the complex index of refraction, those of Irvine and Pollack (Ref. 14)

and Bertie, Labbe and Whalley (Ref. 15). Initially the values for the

complex index of refraction of ice were obtained from Irvine and Pollack

in the wavelength range between 1 and $100 \mu m$, while from 100 to $350 \mu m$ the

data from Bertie, Labbe, and Whalley were used. For lack of experimental

data in the wavelength region shorter than $1 \mu m$, the values for the imaginary

part of the complex index of refraction for water which are also listed by

Irvine and Pollack were used. This approach can be justified, since only

a very small fraction of the energy is absorbed in this spectral region.

Furthermore, it can be seen from Figure 38 that the absorption index plotted

as a function of wavenumber follows a general exponential decrease for ice

in the near infrared region. This feature is common to all transparent solids,

as has been shown by Rupprecht (Ref. 18). The exponential decline of k

is caused by a multiphonon interaction. A continued exponential decrease

in k for ice is therefore to be expected. If one examines the absorption

index for water for wavelength values greater than $0.95 \mu m$, the agreement

with the exponential behavior of ice is obvious; therefore, one can consider

supplementing the missing data for ice with those for water.

In Figure 38 the absorption index of ice and water is plotted as a

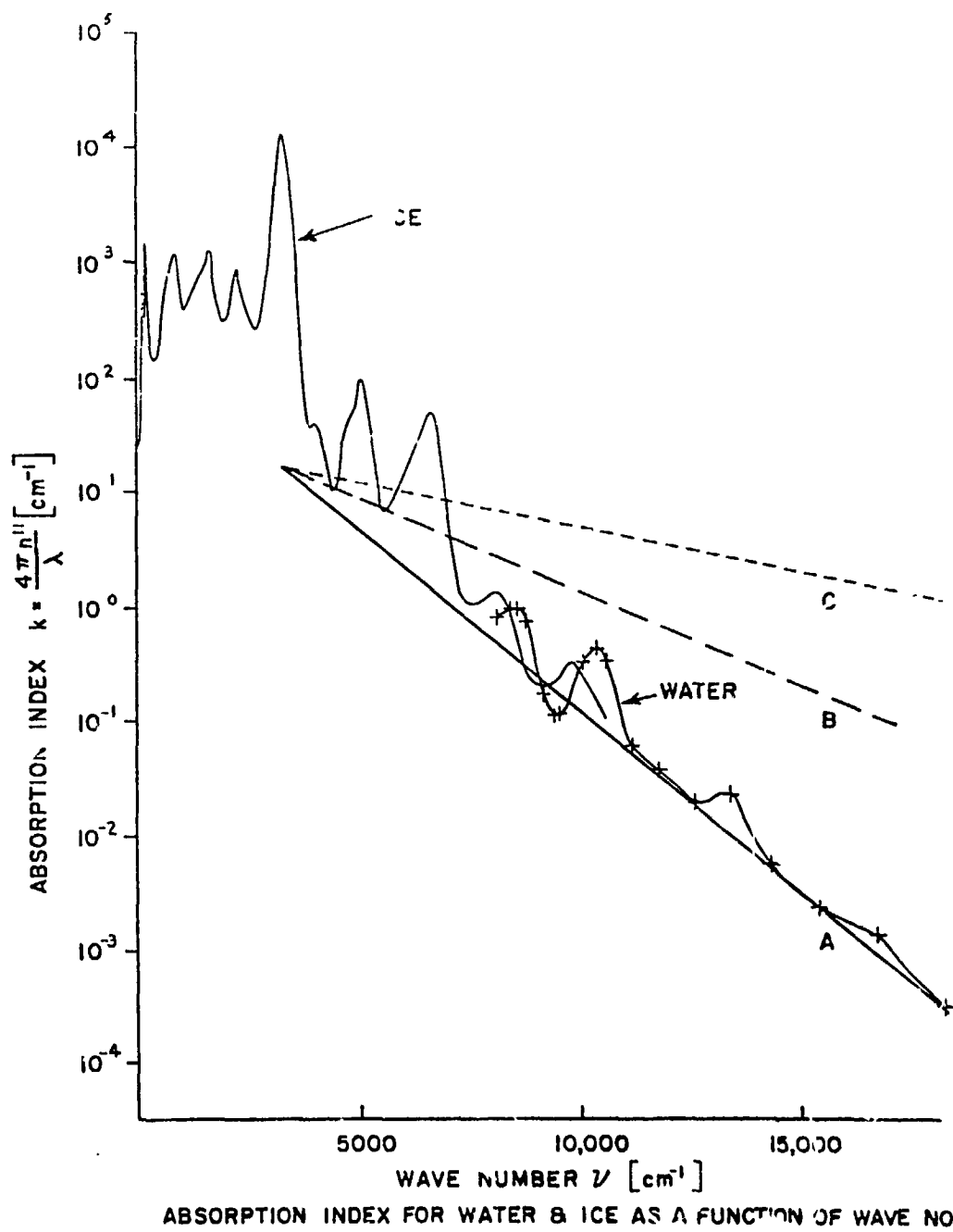function of wavenumber. Combination frequencies and higher-order harmonics

ABSORPTION INDEX FOR WATER & ICE AS A FUNCTION OF WAVE NO.

Figure 38

of the 3μm peak are superimposed on the background absorption represented
by a "baseline", A. Straight lines designated by B and C pertain to a
decreased slope of baseline A, by factors of 2 and 4, respectively, are
added for subsequent use with respect to the influence of impurities in
the optical window of ice.

3.3.2.2 **Preliminary Calculations of the Sublimation Rate of Ice**
Particles under Solar Illumination - Using equation (7), the particle
temperatures and sublimation rates have been calculated as a function of
particle radius at a number of solar distances. The solar radiation $S(\lambda)$
was approximated by a $5900°K$ black body radiation, and the background
radiation T_w was set equal to the usually accepted $4°K$. The results are
plotted in Figure 39. The gap at $1.0 \mu m$ radius is due to the shift from
Mie theory to van de Hulst's approximation, but the discrepancy becomes
sma ler for increasing particle radii.

A sublimation rate minimum develops with increasing solar distance.
While its position depends on the spectral distributions of both the complex
index of refraction and the radiation field, the particle size at the minimum
is independent of solar distance. To demonstrate the influence of the
absorption properties on the sublimation minimum, the effect of an increase
of the absorptivity in the near-infrared and the optical window region of
ice is shown. For $\lambda < 1.33 \mu m$, a "baseline" for the absorption index can be
represented by the solid straight line labeled A in Figure 38. Two other
sets of absorption indices as a function of wavenumber are obtained by
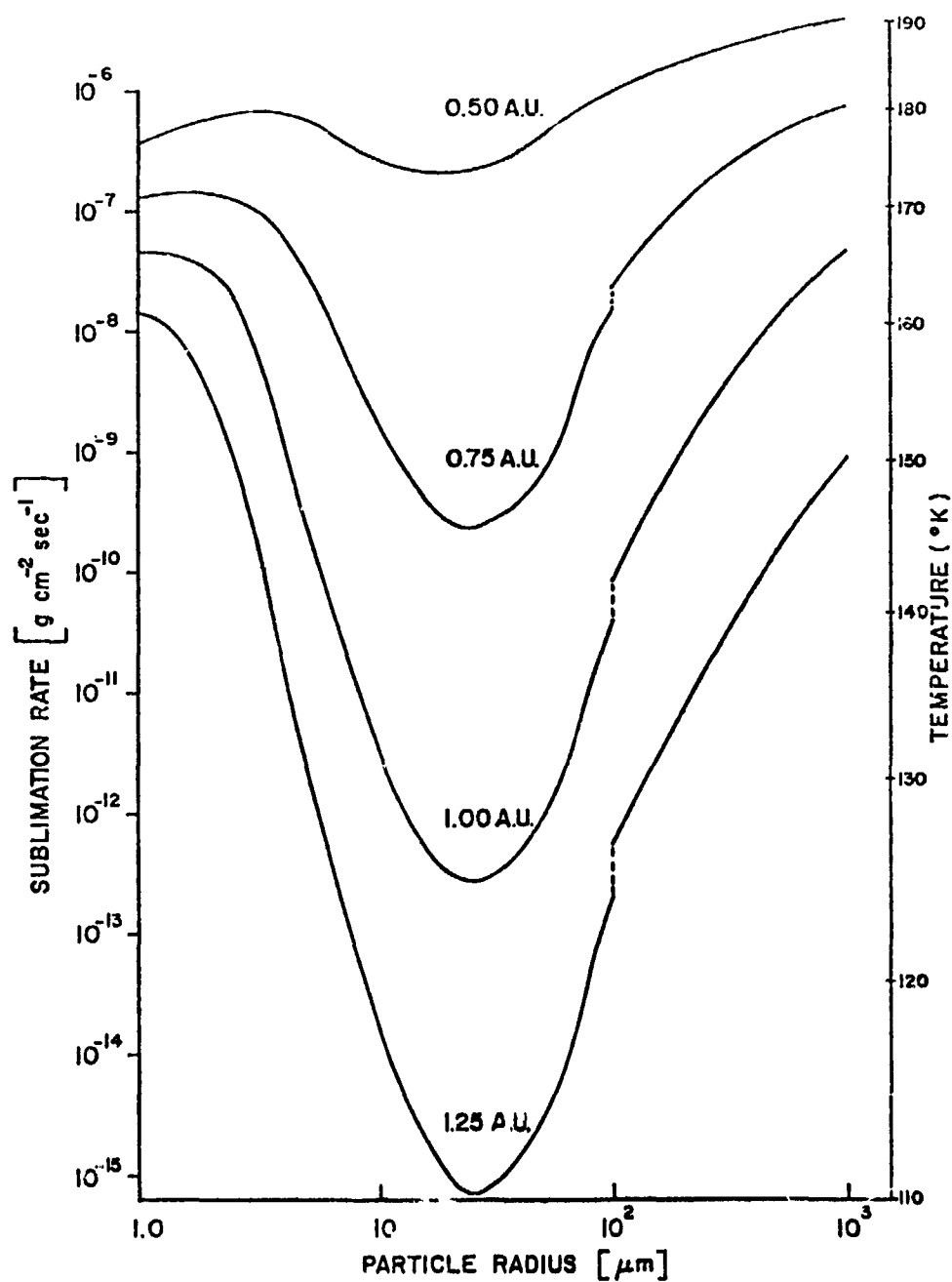adding an amount determined by decreasing the slope of the original base

Figure 39
Sublimation Rates and Temperatures of Pure Ice
for Solar Distances From 0.5 AU to 1.25 AU as
a Function of Particle Size

line by factors of 2 and 4. These baselines B and C, are illustrated
in Figure 38 by the dashed lines. In Figure 40 the sublimation rates as
a function of particle size for the original and incremented absorption
indices are shown at 1 AU. Aside from an increase in the sublimation rates,
a slight shift of the position of the minimum toward a smaller particle
size can be observed. Increasing the absorption is essentially similar
to the introduction of a small amount of impurities into the ice. Note
that the effect of this increased absorption at the absorption edge is
more significant for the larger particles.

These results tend to confirm the experimental observation that at
least for larger particles the sublimation rate decreases with decreasing
particle radius. However, a direct comparison of the absolute values for
the sublimation rate cannot be made because the experimental measurements
were carried out with the radiation of a xenon arc lamp whose spectral
distribution is different from that of the sun. A direct comparsion,
however, can easily be made by introducing the xenon arc lamp spectral
distribution into the computations. This is done in section 3.3.2.5.
First, however, the explanation for the sublimation rate minimum will be
given, since this leads to a discriminating decision between the two
sources for the complex index of refraction.

3.3.2.3 The Explanation for the Sublimation Rate Minimum - In order
to provide some insight into the variation of the sublimation rate with
particle size, an inspection of the product of the absorption efficiency,
Q, and the solar spectral distribution, S, versus wavelength is helpful.
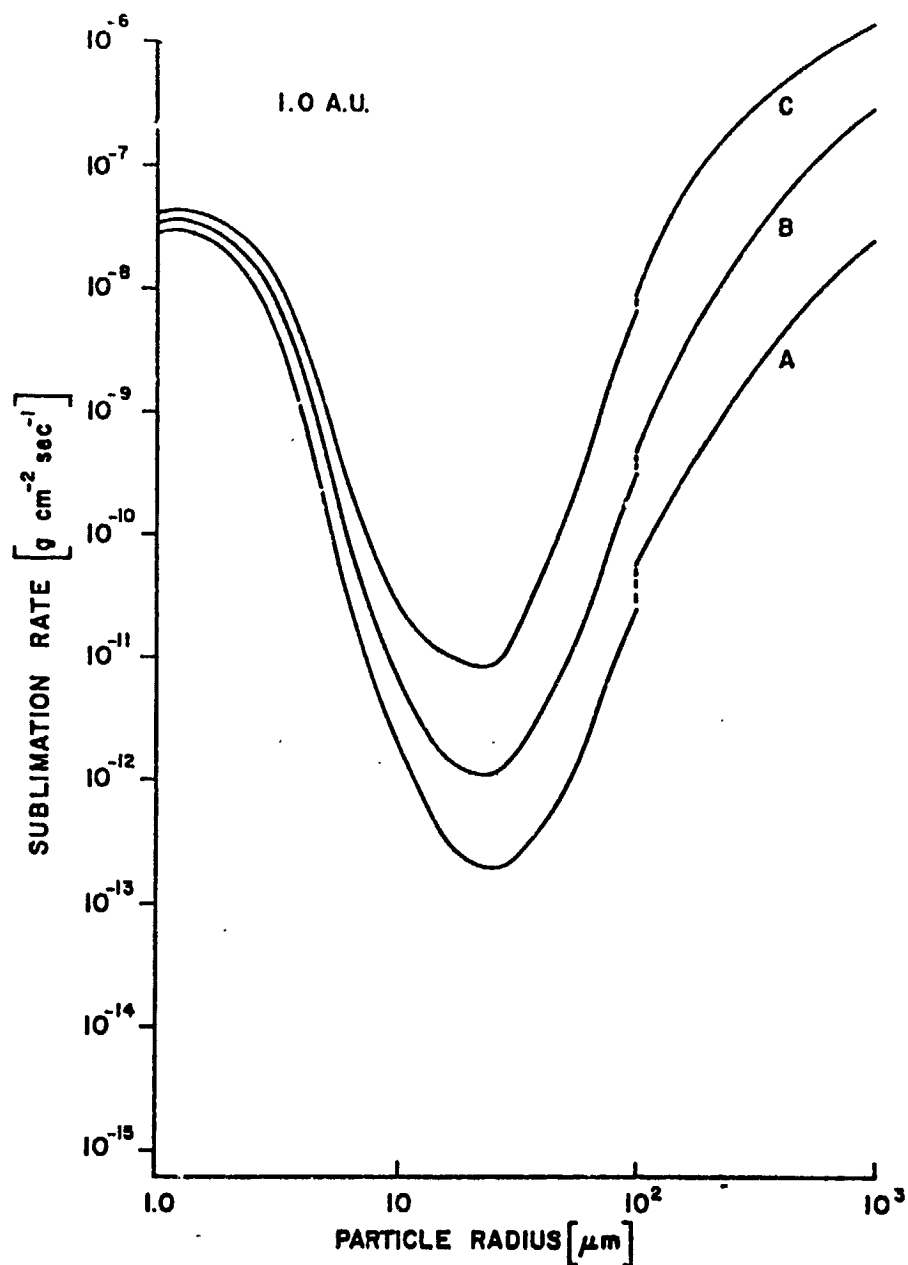
Figure 40
Sublimation Rate as a Function of Particle Size
at 1 AU for Different Absorptivities

In Figure 41 the energy distribution of the sun is represented by a black body radiation at 5900°K. The integral

$$\Delta P_{c.} = \int_{\lambda_1}^{\lambda_2} Q(\lambda, r, n^*) \, S(\lambda) \, d\lambda \qquad (19)$$

gives the power absorbed per unit area at one A.U. between the wavelengths λ_1 and λ_2. The product Q·S is shown in Figure 41 for particle radii between 1 and 10^3 μm. It is apparent that for large particles the main contribution to the absorbed power stems from the absorption peaks of ice at 1.5 μm and 2.0 μm. For smaller particles, however, the absorption by these peaks decreases drastically and the 3 μm peak dominates the absorption. This decrease of the absorption is simply due to a decrease of the effective optical path with decreasing radius. For particles of the order of and smaller than 1 μm even the strong absorption peak at 3 μm becomes inceasingly ineffective in respect to the absorbed power. This variation of the rate of decrease of absorbed power with particle radius is coupled with a decline of the ability of the particle to radiate in the long wavelength region with decreasing radius resulting in a redistribution of the dissipated energy toward sublimation.

3.3.2.4 <u>Evaluation of the Critical Near Infrared Optical Properties</u> <u>of Ice</u> - From the inspection of Figure 41 it is apparent that the sublimation rate depends critically upon the absorptivity of ice in the near infrared region. An examination of published values for the optical properties of ice leads to some discrepancies in this all important r gion. A plot of the data from Irvine and Pollack (Ref. 14) is compared to those of Bertie,
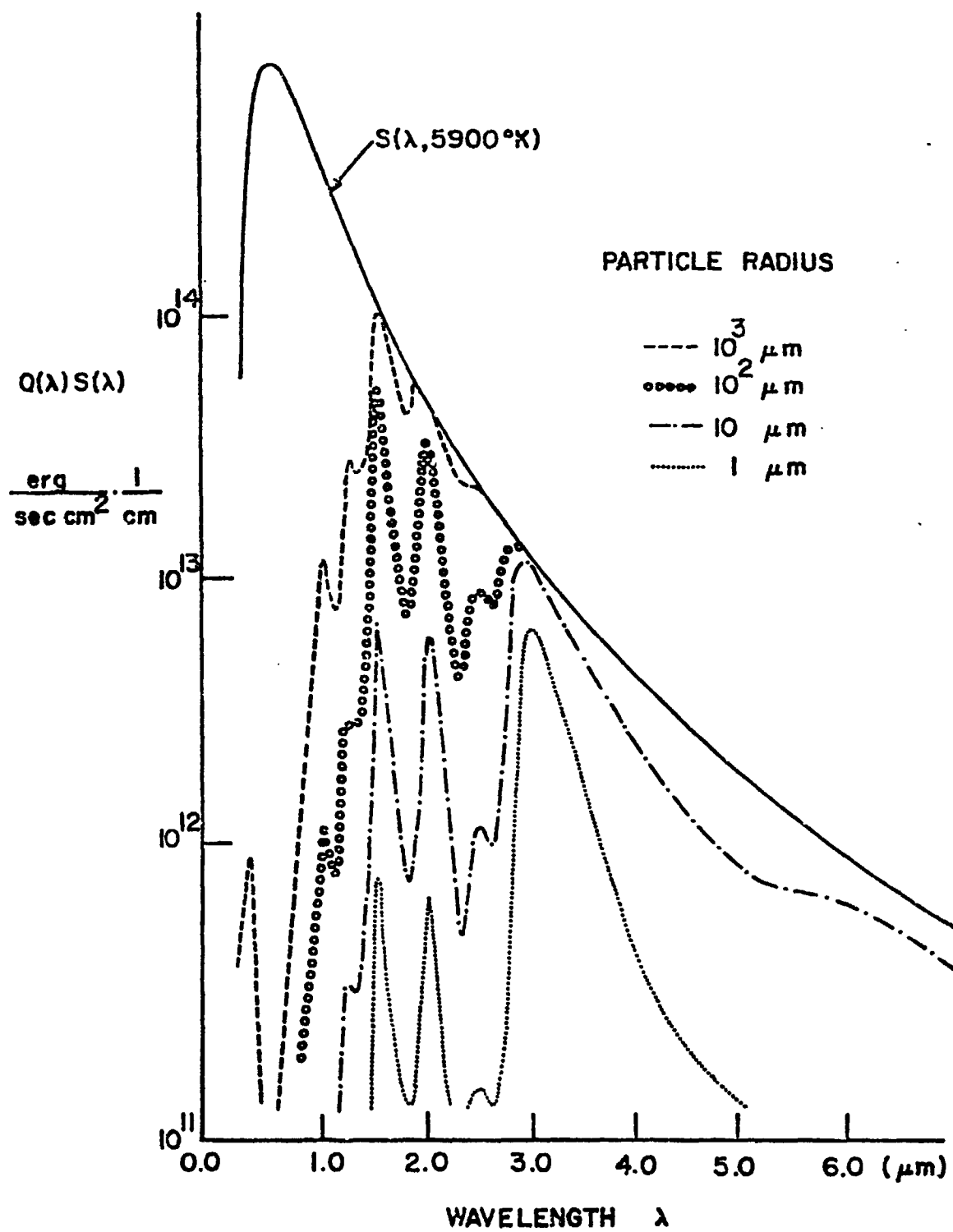
Figure 41

Q(λ) S(λ) vs. Wavelength for Particles From 1 to 10^3 μm

Labbe and Whalley (Ref. 15) in Figure 42. Although the difference between these two spectral absorption curves does not seem very significant, the resulting sublimation rates as shown for 1 A.U. in Figure 43 are somewhat different. Since some disagreement is apparent, an attempt was made to experimentally decide which of the two energy distributions is more appropriate.

To help discriminate between the two choices an experiment was performed which enhances the effect of the critical near infrared region. For this purpose a Corning colored filter glass (filter #3-72) was used to filter the radiation of the lamp. In Figure 44 the results of the theoretical calculations are displayed for the sublimation rate as a function of particle radius that would be expected with the filtered xenon arc lamp radiation using the refraction data from Irvine and Pollack and Bertie, Labbe and Whalley. A substantial difference is apparent. Also shown in the figure are the results of two sublimation rate measurements on ice particles in this filtered radiation environment. Apparently the agreement is closer for the B.L.W. data.

3.3.2.5 Comparison Between Theory and Experiment for Pure Ice Particles - At this point all the ingredients are now available to make a valid comparison between the experimental results of section 3.2.3.2, The Sublimation Rate of Pure Ice Particles under Solar Simulation, and the theoretical expectations. The introduction of the spectral distribution of the xenon arc lamp from section 3.2.1.3, Solar Simulation Calibration, and the index of refraction data from Bertie, Labbe and Whalley into the

WATER ICE

O B. L. W.
□ I. & P.

IMAGINARY INDEX OF REFRACTION

WAVELENGTH (μm)

Figure 42
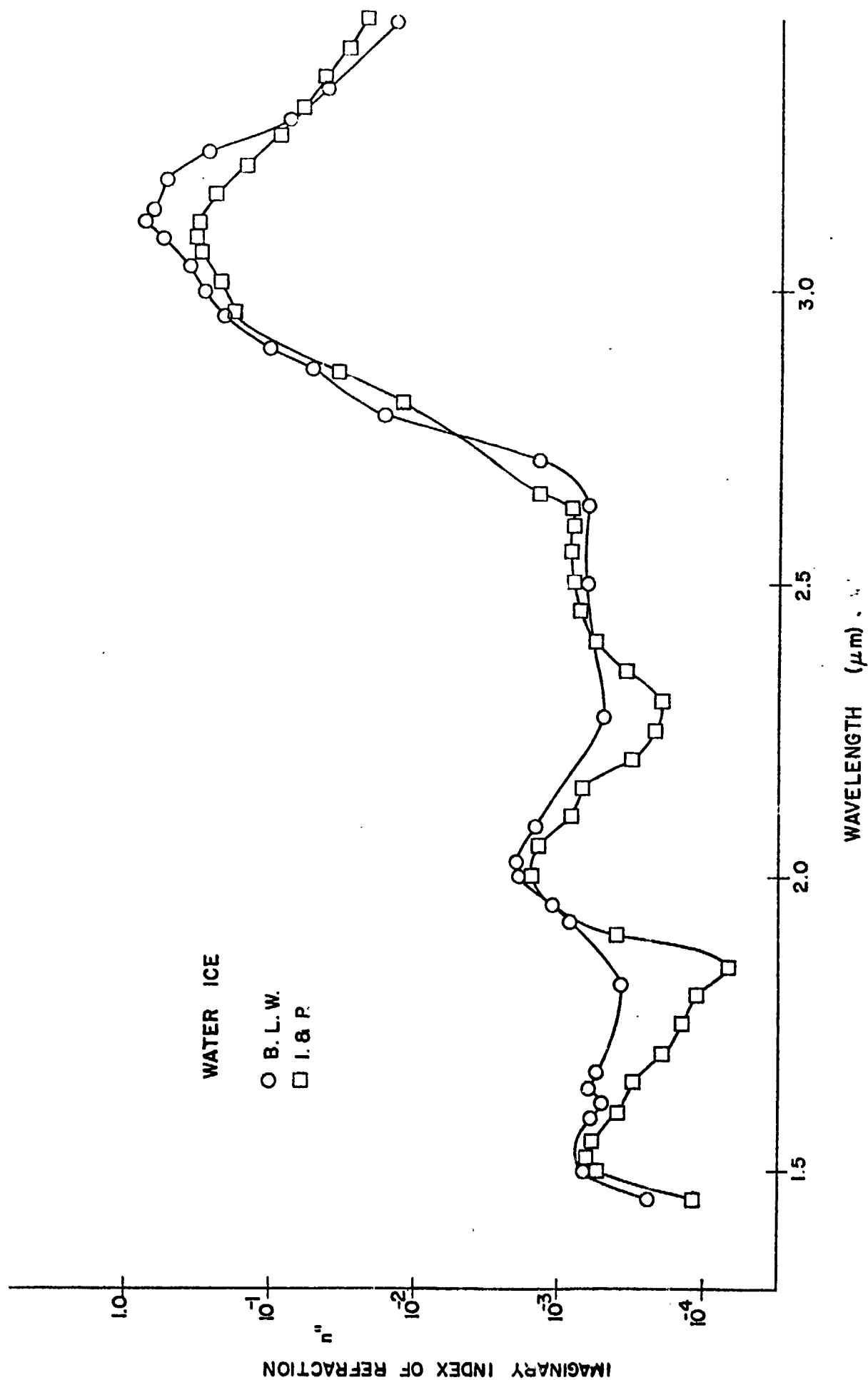
Comparison of Data for the Imaginary Part of the Complex Index of Refraction in the Near Infrared

PARTICLE RADIUS
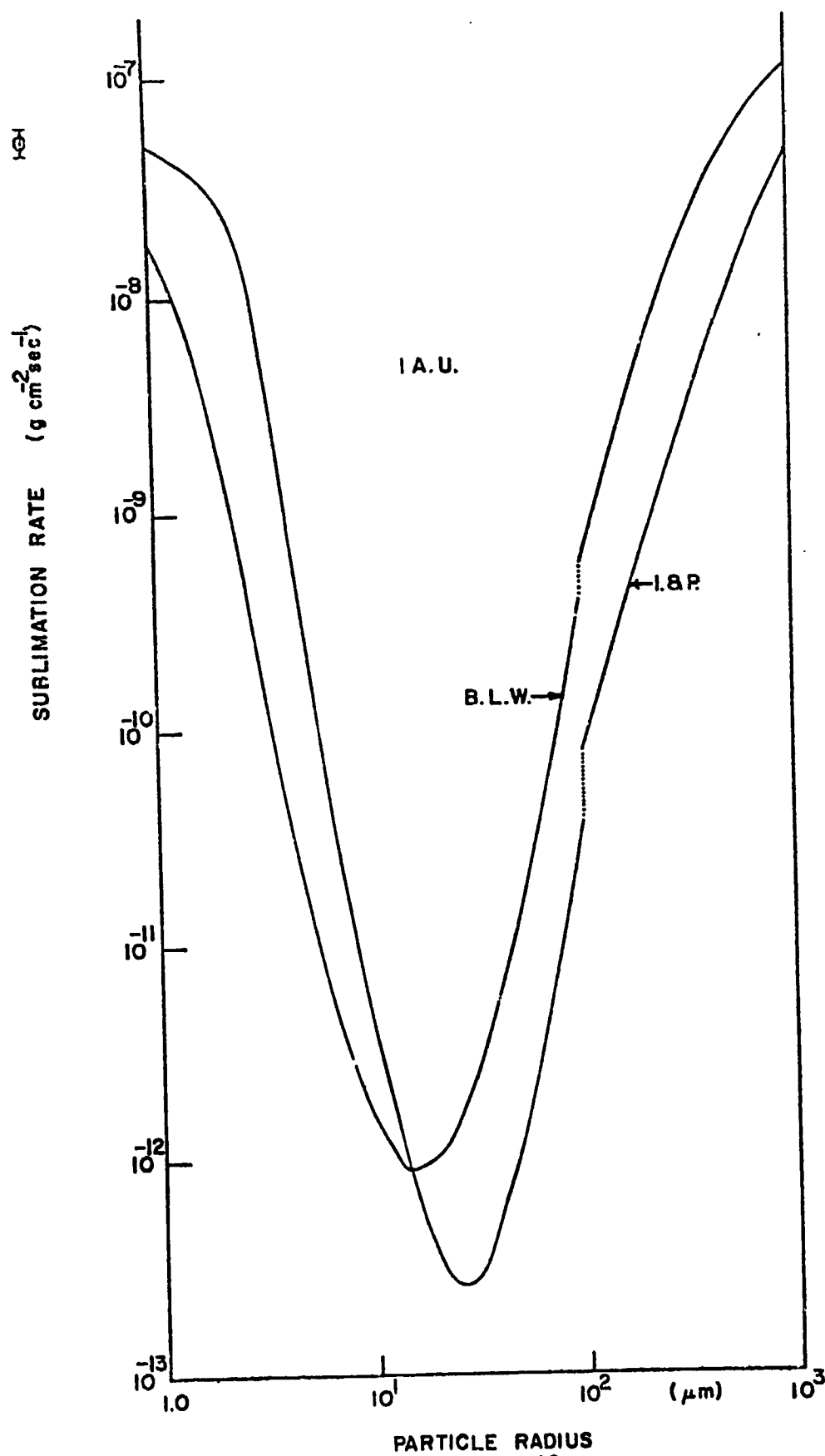Figure 43
Comparison Sublimation Rates vs. Particle Radius at 1 AU Using
Data From Irvine & Pollack (Ref. 14) and Bertie, Labbe, and
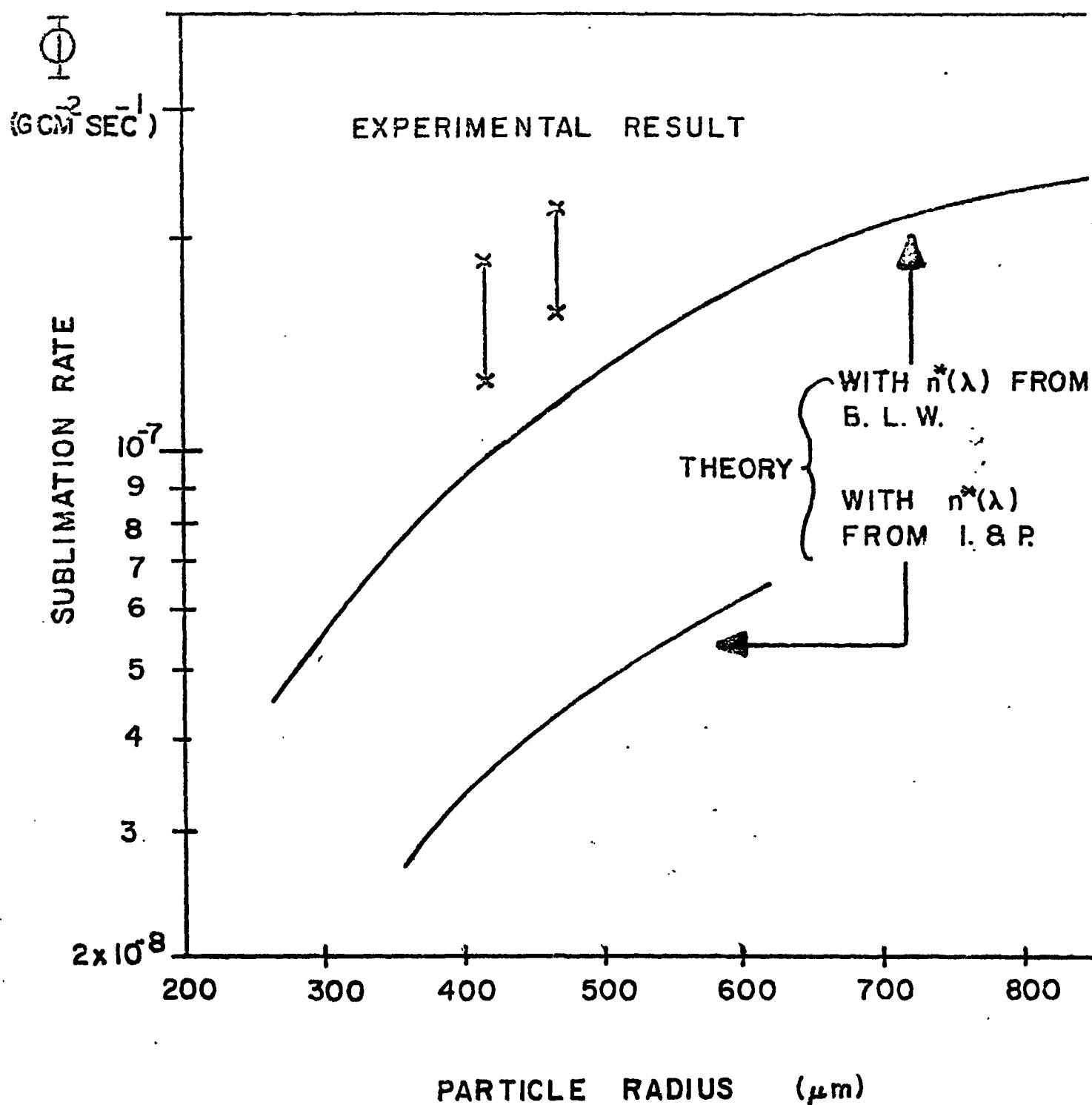Wh ll y (f 15)

Figure 44
Comparison of Experimental Sublimation Rates with
those computed from Irvine & Pollack and Bertie, Labbe, and
Whalley

the computer program yields the results shown in Figure 45.

The agreement between theory and experiment is obviously quite gratifying. Consequently the predictions of the theory become believable.

3.3.2.6 The Lifetime of Ice Particles and the Development of Ice Particle Distributions in the Solar System - In addition to the sublimation rate results computed for 1 A.U. using the index of refraction from Berti.., Labbe and Whalley shown in Figure 43, computations for 0.5 A.U. and 0.75 A.U. are shown in Figure 46.

As large particles become smaller the sublimation rate decreases and reaches a minimum at about 14μm. The sublimation rate increases again and reaches a maximum at about 1μm which coincides with the particle size where the absorption efficiency at the dominant 3μm absorption peak for ice begins to fall off as is evident from Figure 41.

As the solar distance increases, the variation of the sublimation rate becomes very substantial. It is obvious that the assumption of a constant size independent sublimation rate is meaningless. If one examines the consequence of the sublimation rate minimum on the life history of a particle distribution one can observe a considerable compression of this distribution as the particle sizes approach the sublimation rate minimum. An explicit example is shown in Figure 47 at a solar distance of 0.75 A.U. In this case an arbitrary particle size distribution is assumed at time $t = 0$ extending over a 900 μm size range from $10^2 \mu$m to $10^3 \mu$m.

$$t = 0: \quad 10^2 \mu m \leqslant r \leqslant 10^3 \mu m$$

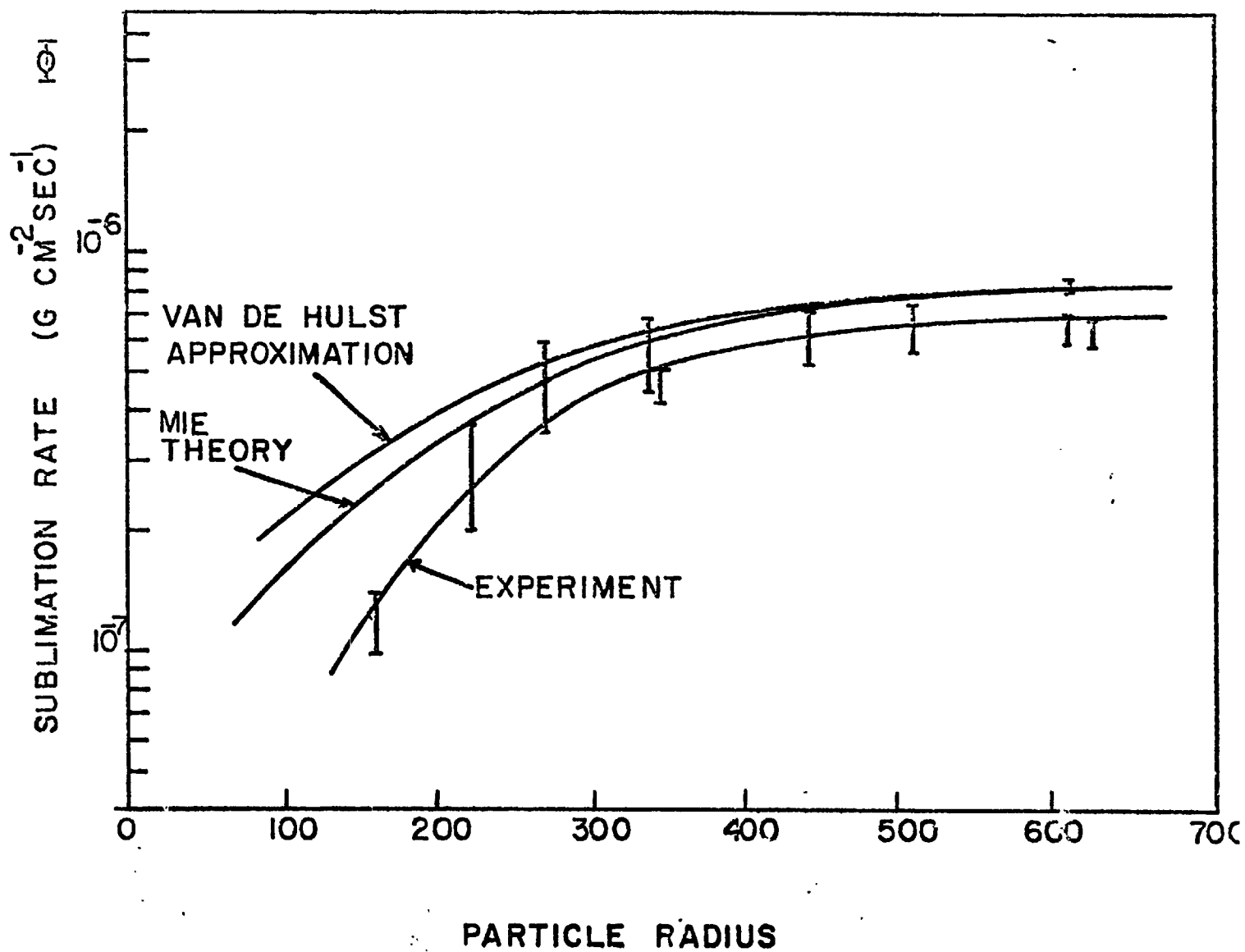The life history of this distribution is now followed. Since the

Figure 45
Comparison of Theory and Experiment of
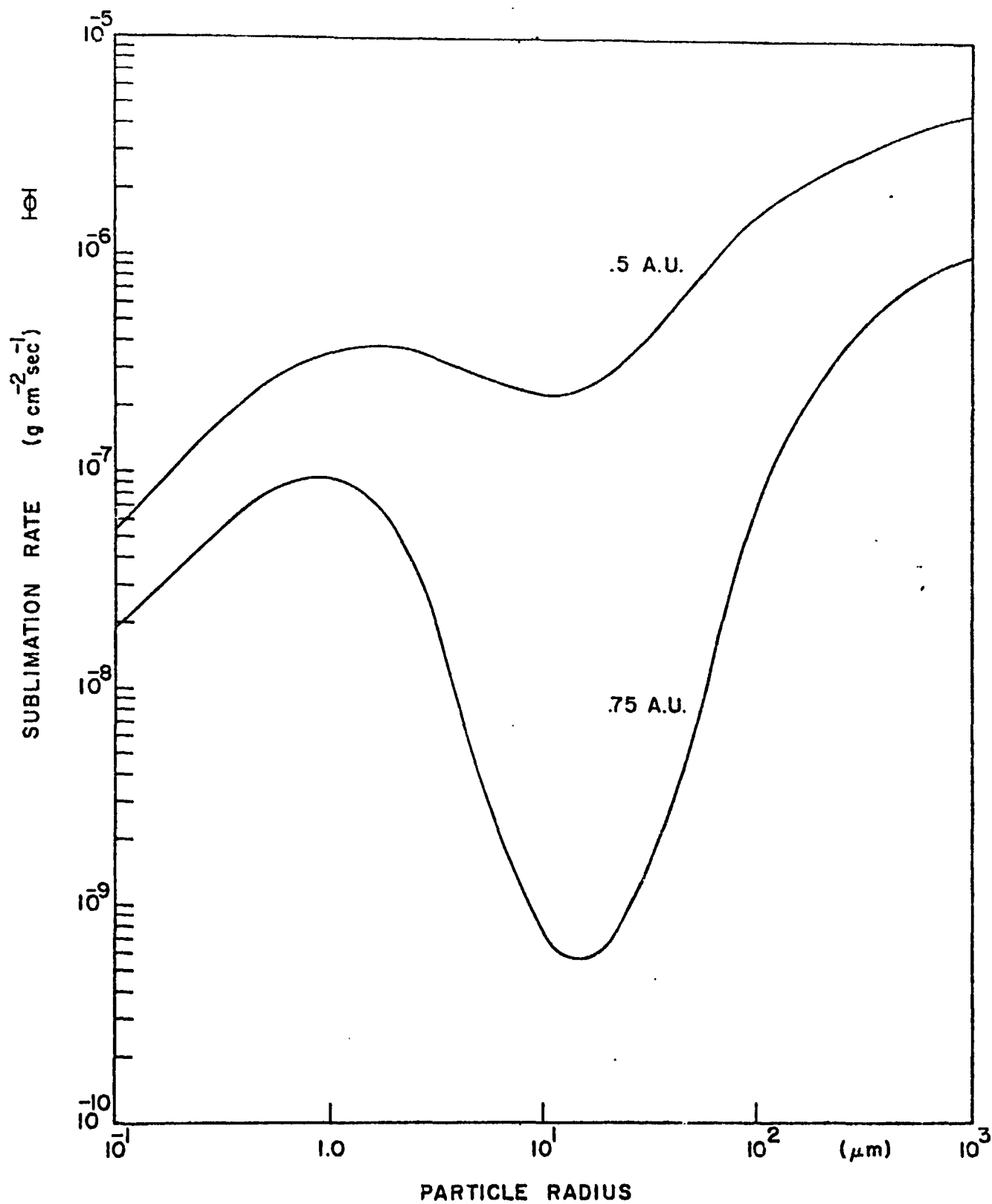Sublimation Rate vs. Particle Size (189 mw cm^{-2})

Figure 46
Sublimation Rate vs. Particle Radius at 0.5 and 0.75 AU
using Bertie, Labbe, and Whalley Data
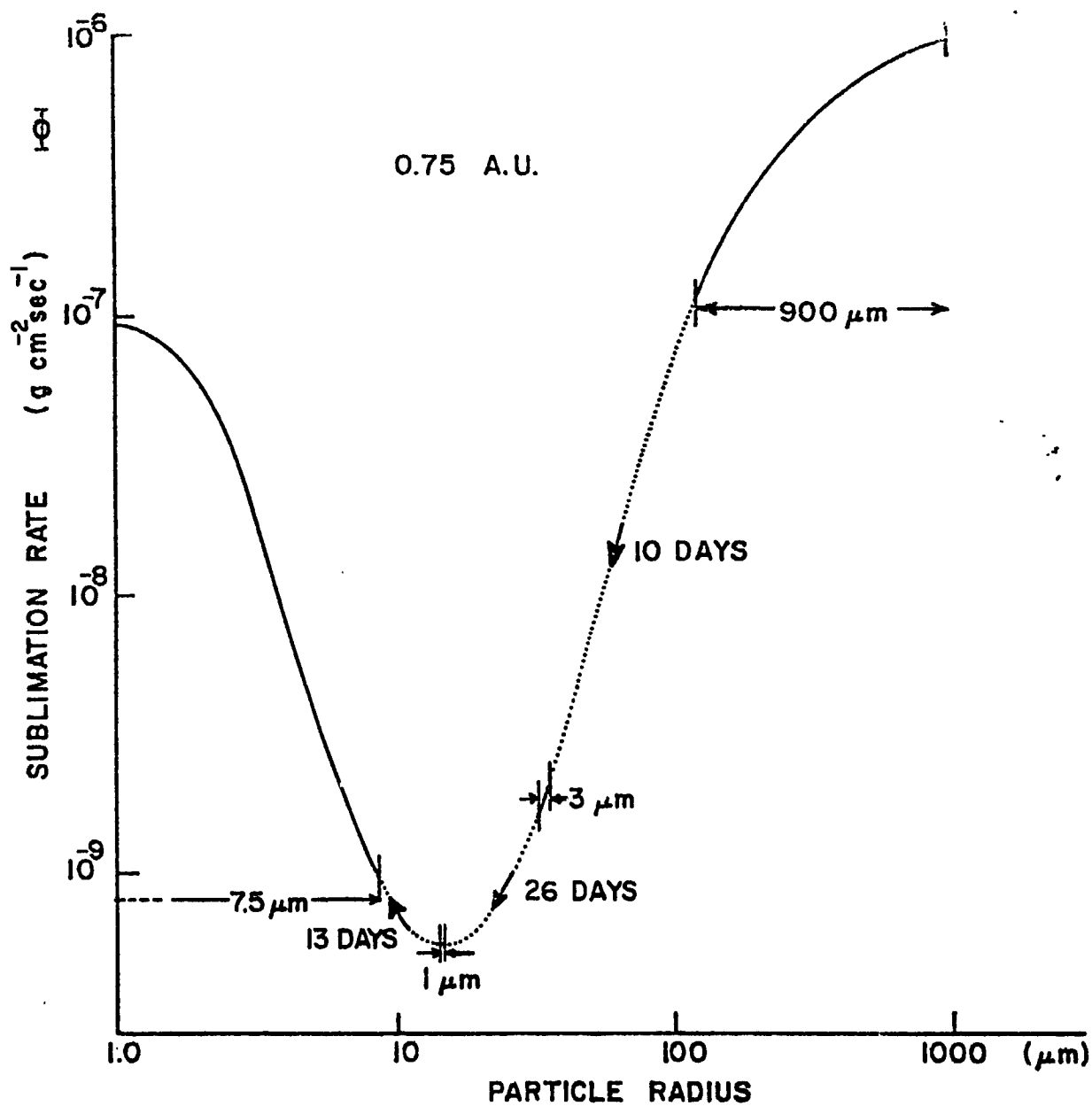
Figure 47
Particle Size Distribution Comparison

number of particles is conserved one finds that at time t_1 all the particles of this distribution are now confined to a rather narrow size range of 3.5 μm width.

$$t_1 = 8.24 \times 10^5 \quad \text{sec} \approx 10 \text{ days:} \quad 32 \,\mu\text{m} \leq r \leq 35.5 \,\mu\text{m}.$$

As the sublimation minimum is reached at time t_2, the size range is narrowed down still further to 1.1 μm. One finds:

$$t_2 = 3.06 \times 10^6 \quad \text{sec} \approx 36 \text{ days:} \quad 14 \,\mu\text{m} \leq r \leq 15.1 \,\mu\text{m}.$$

After another 13 days the lower boundary has receded beyond 0.01 m. At time

$$t_3 = 4.17 \times 10^6 \quad \text{sec} \approx 49 \text{ days:} \quad 0 < r \leq 7.5 \,\mu\text{m}.$$

Thus after 49 days all the particles of the original distribution are smaller than 7.5 μm.

Loosely speaking the effect of the sublimation minimum consists in a bunching of any arbitrary original particle size distribution, that in the history of this distribution all the particles are almost of the same size for most of the time.

This statement can be confirmed by considering the basic relation

$$\rho \, \frac{dr}{dt} = \phi(r) \tag{20}$$

where ρ is the density of ice. Equation 20 can be integrated to determine the lifetime, τ, of an ice particle. For this purpose one must decide about the minimum radius below which a particle is declared dead by sublimation. Since the light scattering of particles with radii $r < 10^{-2} \,\mu$m becomes small for optical wavelength radiation, $r_o = 10^{-2} \,\mu$m has been

defined somewhat arbitrarily as the existence minimum of an ice particle. According to equation 20 one finds:

$$\mathcal{T}(r) = \rho \int_{r}^{r_o} \frac{dr}{\phi(r)} \cdot \qquad (21)$$

The result of this lifetime calculation is shown in Figure 48, where the lifetime, $\mathcal{T}$, is plotted as a function of particle radius for different solar distances. For comparison the lifetime, $\mathcal{T}$, at one A.U. is shown as a broken line when a constant, size independent sublimation rate of $\phi_o = 10^{-7} (g\ cm^{-2}\ sec^{-1})$ is assumed. Obviously the discrepancy can reach several orders of magnitude and illuminates the futility of an albedo concept for estimating the absorption for particles in these size ranges. Figure 43 shows clearly that small ice particles, i.e. ice particles with radii $< 10\ \mu m$ disappear fast. A slight increase in size, however, extends their life span by orders of magnitude.

3.3.2.7 Implication for the Icy Grain Halo Model for Comets -

Delsamme (Ref. 19) has described the development of a comet coma in terms of an icy grain halo model where ice particles are stripped from the nucleus and are carried out by the gaseous drag of vaporizing matter. To determine the size and to describe the photometric profile of the coma, an albedo for the ice particle has been assumed from which particle lifetimes and hence the extent of the coma has been calculated. In order to meet the requirement for the extent of the coma, one is forced to assume initial sizes of particles up to the limit of the gravitational cutoff, which means sizes of the order of 1m in diameter. This requirement imposes exceptionally
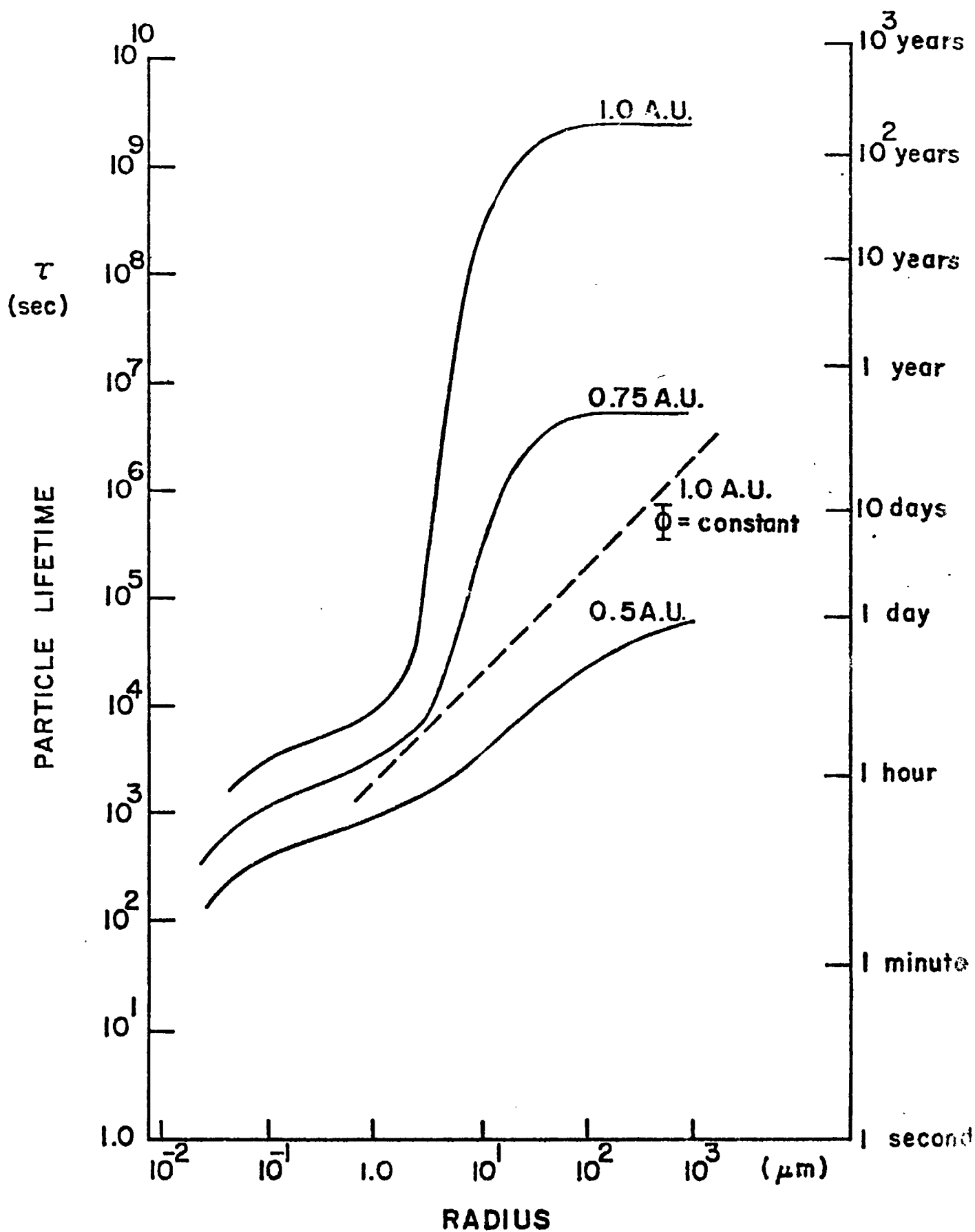
Figure 48
Particle Lifetime vs. Radius

large vaporization rates to impart the necessary momentum for these

tremondous "particles" to move away from the nucleus of the comet. The

necessity for such large ice boulders is due to the fact that the calculations

with an albedo yield a constant sublimation rate which according to Figure 48

yields particle lifetimes which are in error by many orders of magnitude.

If the icy grain halo model is to make sense, the calculations for the coma

have to be repeated in view of this present work. One can immediately see

that particles many magnitudes smaller in size will suffice where the

previous calculations required boulders. This also alleviates the difficulties

with exceptionally high varporization rates to provide drag forces.

3.4 Amorphous Ice and Comet Activity

3.4.1 Amorphous Ice as an Energy Source in Comets - A comet nucleus

is generally recognized as an icy conglomerate as originially proposed by

Whipple (Ref. 2). The Orbiting Astronomical Observatory observations of

Comet Tago-Sato-Kosaka (Ref. 20) and Comet Bennett (Ref. 21) support the

current ideas that H_2O is a major component of comets. If comets were indeed

formed though an accretion mechanism at distances of many A.U. from the sun,

what is the nature of the resulting form of water ice?

A number of studies on the deposition of water vapor at low pressures

and temperatures indicate that amorphous ice is formed. The reported

physical properties include: a density of 1.2g cm^{-3} (Ref. 22), a specific

heat 25% greater than that of ordinary hexagonal ice, and a latent heat for

the phase transition from amorphous to cubic ice of (24 ± 2) calorie g^{-1} (Ref. 23).

The transition occurs at a temperature near $1.0^{\circ}K$ (Ref. 24). If the pressure

and the temperature are high enough, the presence of certain impurities

seems to enhance the growth of clathrate hydrate ices, but both the

clathrates and the amorphous water ice can apparently coexist (Ref. 25).

Observational evidence indicates that comet outbursts require an

internal energy source (Ref. 26), and even much of the ordinary comet

activity seems to require more energy than is supplied by solar radiation.

If at least the surface of a comet nucleus contains a substantial percentage

of amorphous ice, then the phase transition of the amorphous ice to a cubic

structure provides a release of energy which may be responsible for the

outbursts observed in many comets. In addition, if the density of amorphous

ice is about $1.2g$ cm^{-3}, then a 'pulverizing' mechanism would exist because

of the abrupt stresses introduced by the volume change in the solid as the

density of the ice changes by about 30%.

The total energy released during a cometary outburst is of the order

of 10^{21} erg with an accompanying mass loss of 10^{12} g (Ref. 26). The

resulting energy requirement of 10^9 erg g^{-1} compares favorably with the

10^9 erg g^{-1} released during the amorphous - cubic phase change.

Any theory to explain cometary outbursts must consider the spatial

distribution of the phenomenon. Figure 49 reports the results of a study

in which the positions of the comets are shown at the time of outburst

(Ref. 27). Although some observational selection effects may be present,

a definite clustering is apparent within 2.5 A.U. from the sun. Calculations

(Ref. 28) have shown that celestial bodies consisting of water ice with an

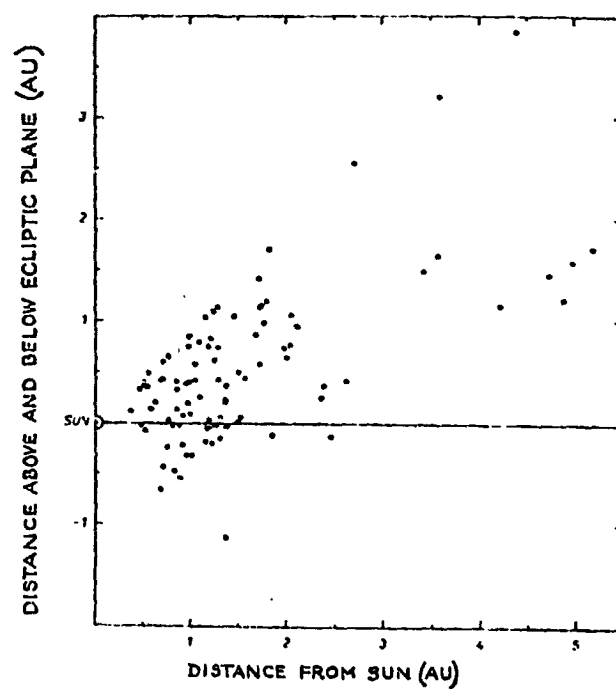albedo of 0.6, at a distance of 2.5 A.U. from the sun, have expected surface

Figure 49. Positions of comets at the time of outbursts. Open circles: hypothetical outbursts preceding discovery. Closed circles: observed outbursts after discovery. (Pittich, 1972)

temperatures ranging from $140^{\circ}K$ for a rapidly rotating sphere, to $180^{\circ}K$ for a non-rotating sphere (see Figs. 1 and 2 of Ref. 28). The phase transition from amorphous to cubic ice requires a temperature near $140^{\circ}K$. Higher temperatures are necessary if the surface has an insulating layer such as that predicted in the model we shall present here.

Any volume element which undergoes this phase transition increases its temperature by about $45^{\circ}K$. Therefore, the heat released can trigger the surrounding material so that the phase change is, in effect, a self feeding mechanism which propagates within a range where the local temperature is near $100^{\circ}K$.

The outburst of a comet can, therefore, be envisioned as occurring in a series of consecutive steps: initiation, propagation, pulverization, sublimation, ejection, and insulation.

Depending upon the condition of the surface of the comet, the amorphous - cubic phase transition can be achieved at different solar distances. If the surface is amorphous ice, an outburst is most probable at about 2.5 A.U. from the sun. If the surface is covered with an insulating layer, however, a closer approach to the sun is required. On the other hand, if amorphous ice is in heat exchange with material with a temperature which increases faster than that of the ice, then an outburst can be expected at greater distances.

Once the phase transition has been initiated, it will propagate within a region where the temperature of the ice is greater than $100^{\circ}K$. The volume into which the transition can propagate can be estimated. Our

calculations consider a spherical comet with a radius of 5 km. For a rough estimate we assume that the surface temperature around the subsolar point decreases as a cosine function. For a subsolar temperature of $140°K$, the surface area with a temperature above $100°K$ is bounded by a circle and contains 14% of the total surface area of the comet. Following Sommerfeld's (Ref. 29) development, it is possible to estimate the depth at which the phase transition terminates to be 1 m below the surface at the subsolar point. For this calculation the thermal diffusivity of glass, $2 \times 10^{-2} \ cm^2 \ s^{-1}$, is used. As this depth is reduced to zero at the perimeter of the previously computed area, an average depth of 50 cm is assumed. The resulting volur which undergoes the phase transition is $2.2 \times 10^{13} \ cm^3$. The density of amorphous ice is about $1.2g \ cm^{-3}$ and so the mass involved is $2.6 \times 10^{13}g$.

The transformation of amorphous ice into cubic ice with a density of $0.94g \ cm^{-3}$, must induce severe strains of the order of 9% which will pulverize the ice. It is useful to estimate the particle size which results from the fracturing process. For glass (Ref. 30) where the stress, S, is about 10^4 pound $inch^{-2}$, W is proportional to r^{4}, where W is the average mass of the ten largest particles that result when the stressed material fractures. If this relationship holds in general for higher stresses, then an extrapolation to the anticipated stress encountered for the amorphous - cubic ice transformation ($\approx 3 \times 10^5$ pound $inch^{-2}$ for strains of 9%), shows that W is of the order $3 \times 10^{-7}g$. This implies that the largest particle has a size of about 100 μm.

This mechanism therefore automatically provides a source of

particulate matter which creates a huge surface area. Consequently,
the equilibrium vapour pressure between the particulates will be rapidly
established. With the mass $(2.6 \times 10^{13}g)$ involved in the phase transition
the energy, E, which is released, is given by:

$$E = 2.6 \times 10^{13}g \times 24 \text{ calorie } g^{-1} \qquad (22)$$

$$= 6.25 \times 10^{14} \text{ calorie}$$

This can generate water vapour of mass, M:

$$M = E/H = 6.25 \times 10^{14} \text{ calorie}/650 \text{ calorie } g^{-1} \qquad (23)$$

$$= 9.6 \times 10^{11}g$$

where H is the heat of sublimation. This means that 3% of the generated
particulate matter is sublimated. This gas must certainly expand into the
vacuum of space at a few times the velocity of sound, carrying with it,
at least to an order of magnitude, a comparable mass of dust. This mass
is consistent with observed values for typical comet outbursts $(10^{12}g)$
(Ref. 26).

A large fraction of the fractured material remains on the surface.
This effectively creates an insulating layer with a high albedo which tends
to prevent further outbursts for some time.

This picture of comet outbursts can be subjected to many refinements,
such as variations of comet sizes, or of rotation rates and inclinations,
impurities and inhomogeneities in the ice, and orbital parameters. The
general features of this theory are, however, consistent with observations
and in our opinion provide for a more plausible source of energy than has

been previously suggested. Those suggestions have included the

vaporization of pockets of methane and/or carbon dioxide (Ref. 26),

explosive radical reactions (Ref. 31), and collisions with interplanetary

boulders.

3.4.2 Low Temperature, Low pressure Depositions - The essence of

the previous section has been published in Nature, (Ref. 7). At that time

the paper was somewhat speculative (as most comet models are) especially

since information on low pressure, low temperature depositions of different

ices and ice mixtures are sparce. Although the published model is based

on the evidence of relatively pure water ice (where at least a few papers

on the subject were available) it is thought that the proposition of pure

water is not a necessary condition for the functioning of the model.

According to this comet model the energy source for the comet activity

it pictured as being stored in the disordered molecular structure of the

amorphous ice. The literature contains only a limited number of studies

on the physical properties of this form of ice, and there are virtually no

studies available on the modification of the physical properties of this

ice when other gases are present during the condensation process. Since

this information would appear to be at the core of any attempt to understand

the behavior of comets, an experimental setup has been deviced and a number

of depositions have been conducted to establish a firm experimental base on

which the theory can be scrutinized and/or improved.

3.4.2.1 Instrumentation - Apparatus has been designed and constructed

which enables the deposition of ice at low temperatures and pressures on a

copper disc of 0.5 cm^2 area. The disc is attached with nitrocellulose to the end of a fiber approximately 3 cm long. The fiber acts as the elastic element in the microbalance system which has been described previously. At the connection between the fiber tip and the center of the copper disc, the junction of a fine thermocouple (wire diameter 25mm) is attached, the leads of which run roughly parallel to the fiber axis. The plane described by the thermocouple wires is perpendicular to the plane described by the oscillation of the fiber so that the fiber oscillation is affected as minimally as possible by the presence of the thermocouple. A hollow, quarter inch diameter stainless steel rod holds the fiber - copper disc - thermocouple assembly. The rod protrudes through the top of the vacuum chamber and is capable of vertical motion by use of an "o" ring compression fitting. The thermocouple leads are run through the interior of the rod and are available for readout at the top of the rod which is sealed by vaccuum wax.

To provide for cooling of the copper disc, a copper rod, 2.5 cm in diameter and 12.5 cm long is mounted on a temperature controlled platform. The platform is cooled by a copper tube which circulates liquid nitrogen through an external supply tank. The copper rod is bolted to the platform with an indium gasket to insure good thermal contact even under vacuum conditions. A teflon sheath surrounds the rod to minimize losses. At the top of the rod, a cylindrical extension about 3mm long and 7mm in diameter is provided as a platform on which the copper disc at the end fiber can be placed and cooled by conduction from the rod. The copper disc is slightly

larger in diameter than the protruding cylinder to minimize ice build-up between the rod and the disc during depositions.

A diagram of the experimental setup is shown in Figure 50. The electrodes are the field plates between which the fiber can be placed in oscillation. Not shown in the diagram is the copper cylindrical shroud which is temperature controlled and completely surrounds the items shown in the Figure. The shroud has crystalline quartz windows heat sunk to the shroud walls which provides optical access to the apparatus. A picture taken through the optical window is shown in Figure 51. The picture presents an end-on view of the copper disc suspended from the fiber-thermocouple assembly. Below the suspended disc is the platform on top of the cooled copper rod upon which the disc is placed during depositions. The mass calibration of the fiber disc assembly is shown in Figure 52 where the added mass is plotted versus the frequency of oscillation. The calibration was accomplished with assorted pieces of wire whose mass per unit length was determined initially by an analytical balance.

3.4.2.2 <u>Experimental Procedures</u> - Initially the depositions were carried out in the following manner. The chamber was evacuated and the copper disc suspended from the fiber-thermocouple assembly was lowered onto the platform on top of the copper rod. The shroud inside the vacuum chamber surrounding the apparatus was cooled to liquid nitrogen temperature. Subsequently the copper rod was also cooled to liquid nitrogen temperature. When the thermocouple attached to the top of the rod indicated that liquid nitrogen temperature was reached, the temperature of the copper disc was
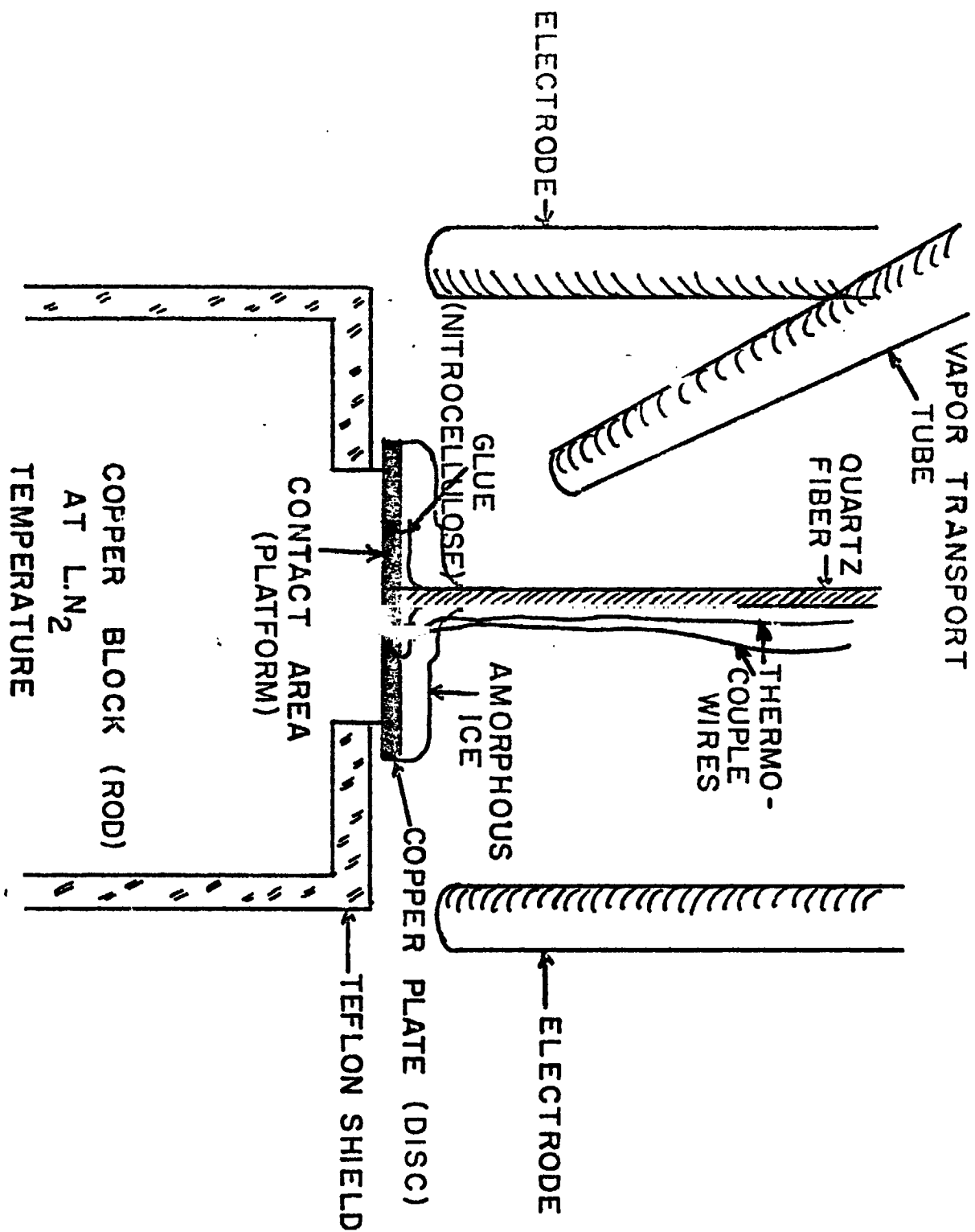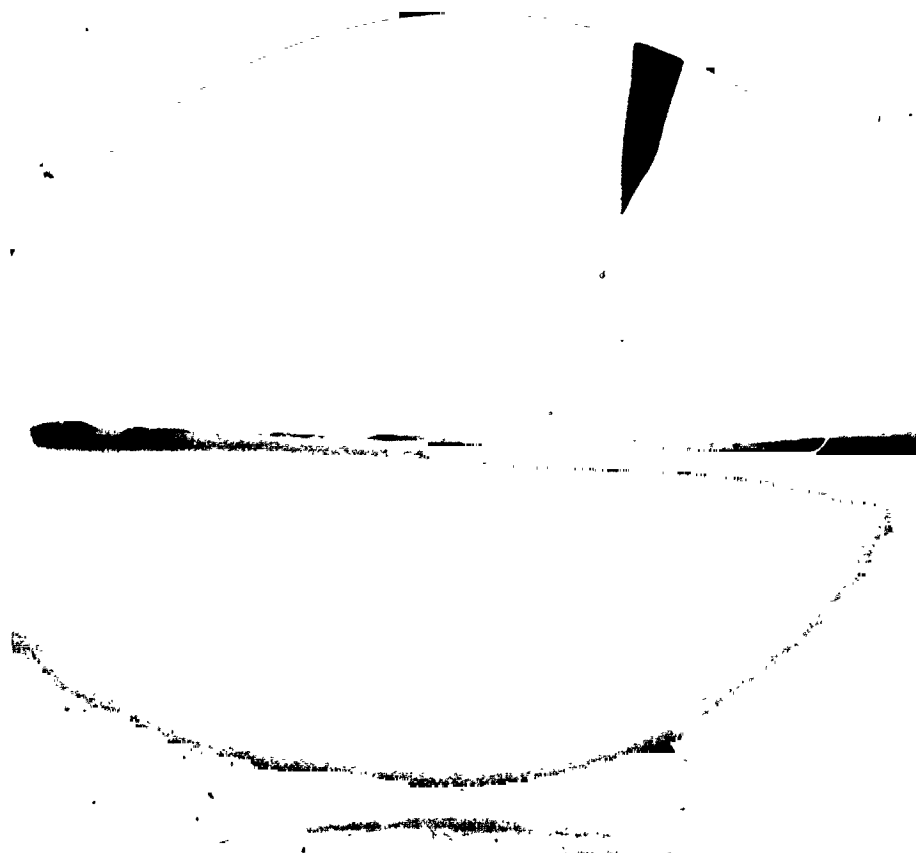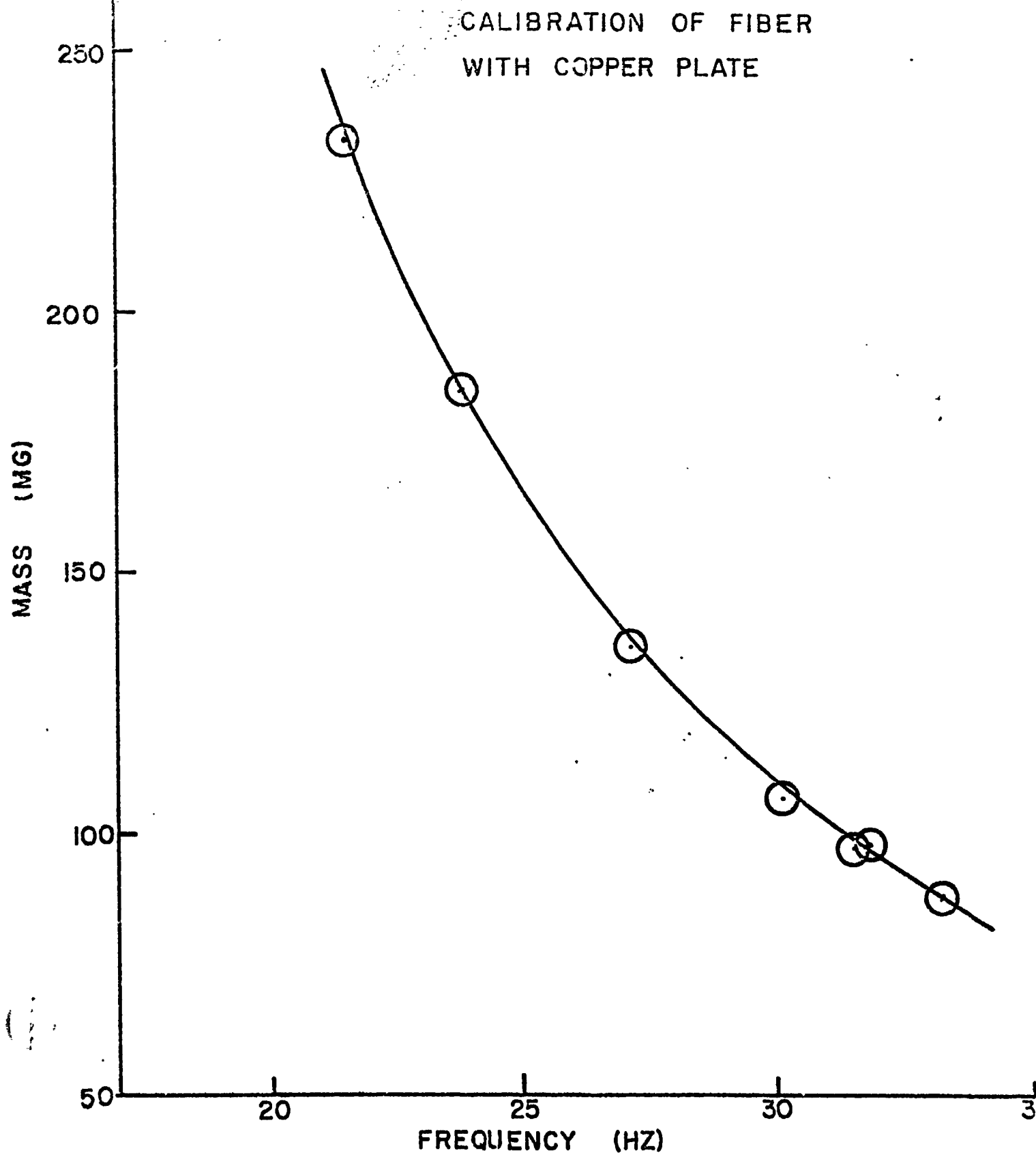
FIGURE 50. EXPERIMENTAL SETUP FOR VAPOR DEPOSITIONS

Figure 51 - Placement of Copper Disc on Cooled Platform

Figure 52
Calibration Curve for Fiber-Disc-
Thermocouple Assembly

CALIBRATION OF FIBER
WITH COPPER PLATE

monitored to ensure that good thermal contact with the copper disc and
the top of the rod was established. Originally the water vapor was controlled
by a bleed valve and transported through the vapor tube shown in Figure 50.
Unfortunately there was not sufficient control over the deposition rate,
and as a consequence, the result shown in Figure 53 was obtained. The ice
has angular edges and cannot be pronounced to be amorphous ice. After
many futile attempts, the blame was placed on too high a deposition rate.
The bleed valve was consequently opened only to the point where interference
colors could be seen slowly moving in the form of fringes across the copper.
Within several minutes the interference colors faded and no apparent ice
buildup was evident. After a period of absolutely no apparent progress
a sudden burst of activity occurred. Ripping across the surface dendritic
growth in the form of thin transparent "ribbons" propagated at incredible
speeds and raised themselves vertically still growing and extending. There-
after the surface looked like transparent grass. An example of the type
of crystalline growth that appeared is shown in Figure 54. It is believed
that this frantic activity grew out of a smooth, homogenous layer of
amorphous ice. What triggered the sudden activity which transformed the
smooth quiescent surface into a dendritic forest is not known, although
fluctuations in the vapor supply through the bleed valve and vapor tube may
have been responsible by creating a local temperature elevation which
could have initiated nucleation. How much amorphous ice was present at the
time just before the nucleation took place and whether or not this activity
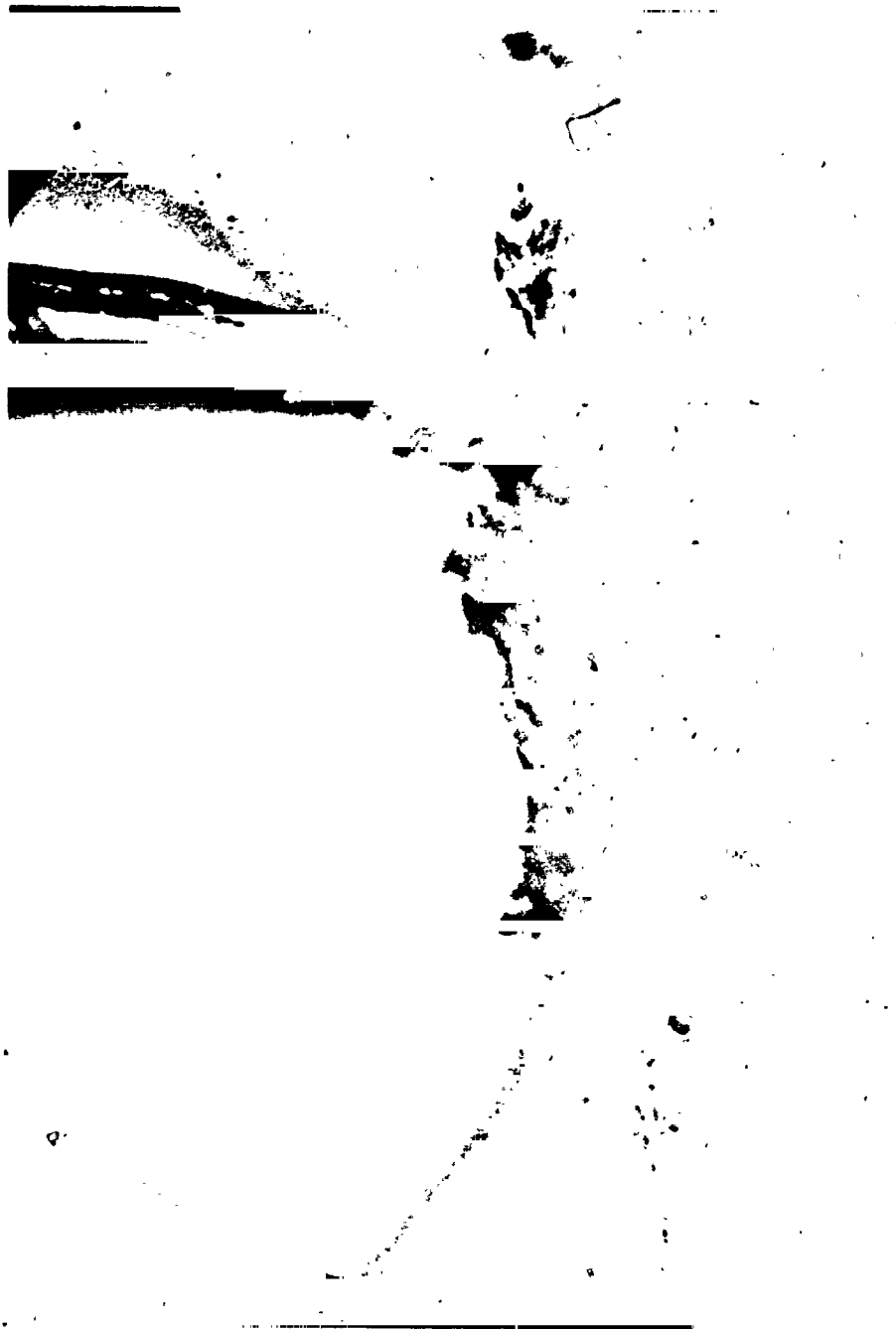has any relation to comet activity is an open question.

Figure 53 - Ice Deposit on Disc (non-amorphous)

Figure 54 - Crystals Resulting from Rapid Growth out of a Thin Deposit of Ice

As interesting as these observations may have been, it was the
aim of this study to observe the energy release from a thick layer of
amorphous ice. However, the many futile attempts provided the impetus
to try a different method of deposition. In this new mode of operation,
the vapor tube was removed. The ability to control the temperature of the
surrounding shroud prompted its use as a controlable vapor source. For a
first trial, the fiber and disc assembly was removed to allow the vapor
to deposit on the platform on top of the copper rod. As a vapor source
ice cubes were crushed and a few grams were placed against the chilled
shroud. After closing and evacuating the chamber the shroud and with it
the ice were cooled to liquid nitrogen temperature. As the next step the
copper rod was cooled to liquid nitrogen temperature. Next the shroud
was allowed to warm up and was maintained within a temperature range from
160 - 195°K. As a consequence water vapor leaves the ice on the shroud
and deposits on the coldest spot, namely the platform on top of the copper
rod. Again interference colors were seen and faded out within 10 minutes.
All through the deposition the chamber was continually pumped and the
ionization gauge indicated 10^{-5} torr or lower. After several hours absolutely
no ice buildup was apparent on the platform. The fine machining marks on
the face of the platform were clearly visible. In disgust, just to see
if any ice had been deposited at all, a rod was lowered to scratch the
surface of the platform in the hope of seeing at least a little white powder
as a sign of some ice being present. Surprisingly a sizable gash about
120 μm deep became visible where the rod had contacted the platform (see

Figure 55). Apparently a significant amount of ice had actually deposited but was so transparent and exhibited so little light scattering that it completely escaped optical detection!

Having established that the shroud technique was a viable means for producing a thick deposition of (hopefully) amorphous ice, the fiber disc assembly was reinstalled and the deposition was conducted onto the disc. In this arrangement another problem arose. Ice also formed on the quartz fiber and the thermocouple wires. This interfered with many of the mass measurements by stiffening the fiber but was eventually minimized by irradiating the quartz fiber and the thermocouple wires with the external xenon arc lamp. In order to demonstrate the faithful reproduction of surface features of the copper disc substrate, Figure 56 shows two stages during a particular deposition. Note how well the nitrocellulose terrace at the center of the disc is reproduced. One can also notice how the quartz fiber and the thermocouple wires become coated with ice.

After the deposition is stopped the shroud is cooled down again to liquid nitrogen temperature to prevent further deposition. The disc is then raised, and its thermal contact with the copper platform is interrupted. The fiber is set into oscillation to make mass measurements and photographs of the disc are taken in an edge-on position to determine the thickness and hence the volume of the deposition. In this way an estimate of the density can be made. A typical deposition is shown in Figure 57 in comparison to the disc prior to deposition. While the disc is off the platform, its temperature is monitored by the thermocouple as it is allowed to warm up,

Figure 55 - Smooth, Glassy Ice on Platform

Figure 5. - Top photo...

Bottom photograph was taken thro...

Figure 57 - Edge View of Disc with and
without a Deposit (11X)

so that an energy release in the ice deposit can be observed as a temperature increase beyond an ordinary temperature trend.

3.4.2.3 Experimental Results - The depositions can be separated into three types: water ice, water ice with ammonia, and water ice with methane.

3.4.2.3.1 Water Ice Deposition - The results of three different water ice depositions are shown in Figure 58. These are the original data of the disc temperature as taken from the temperature recording. The temperature is indicated at the left hand side of the recording. The time scale is 2.5 minutes/division. One can see that at the moment when the disc is lifted from the platform the disc temperature is 77°K. Due to radiative heat transfer from an opening at the top of the shroud and conductive heat transfer through the quartz fiber and the thermocouple wires, a temperature rise establishes itself. Suddenly, however, at a temperature of about 120°K an abrupt rise in the temperature by about 20°K occurs. After this sudden temperature increase the temperature decreases again. Without any doubt this behavior is indicative of an internal energy release in the ice, most likely the result of a phase transition from amorphous to cubic ice. According to the volume and mass estimates the density of the ice before and after the energy release was about $(0.9 \overset{+}{-} 0.1)$g cm^{-3}. The relatively large error assigned to this value stems mainly from the difficulties associated with the ice built-up on the quartz fiber. This density value agrees with those of a recent paper by Venkatesh, Rice, and Narten (Ref. 22) who report a density of 0.9 g cm^{-3} for amorphous ice deposited at liquid

(°K)

Deposition
Time: 9.7 hr

Deposition
Thickness:
0.36 mm

Deposition
Time: 4.5 hr

Deposition
Thickness:
0.45 mm

Deposition
Time: 5.2 hr

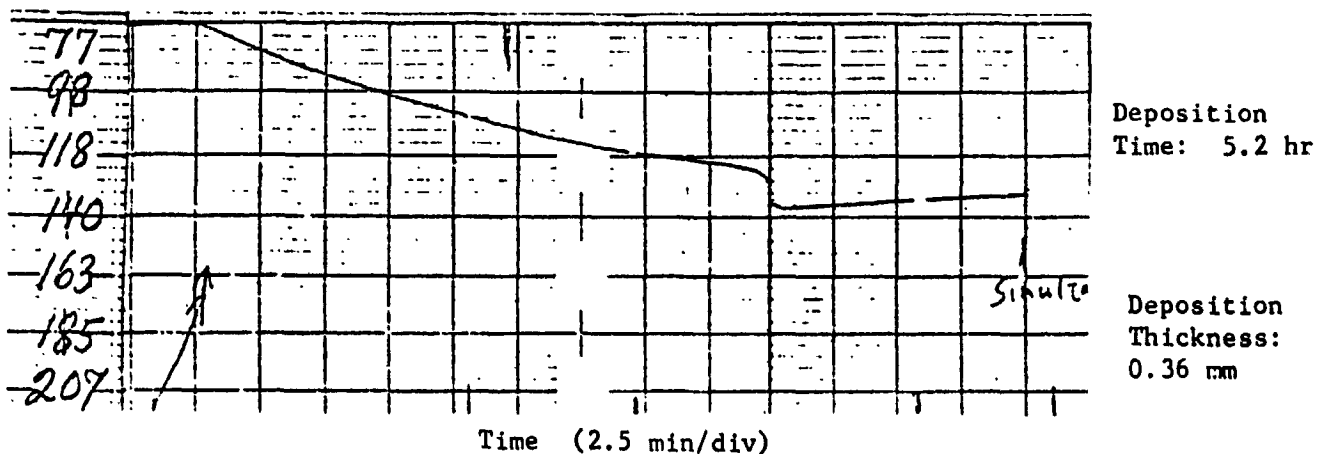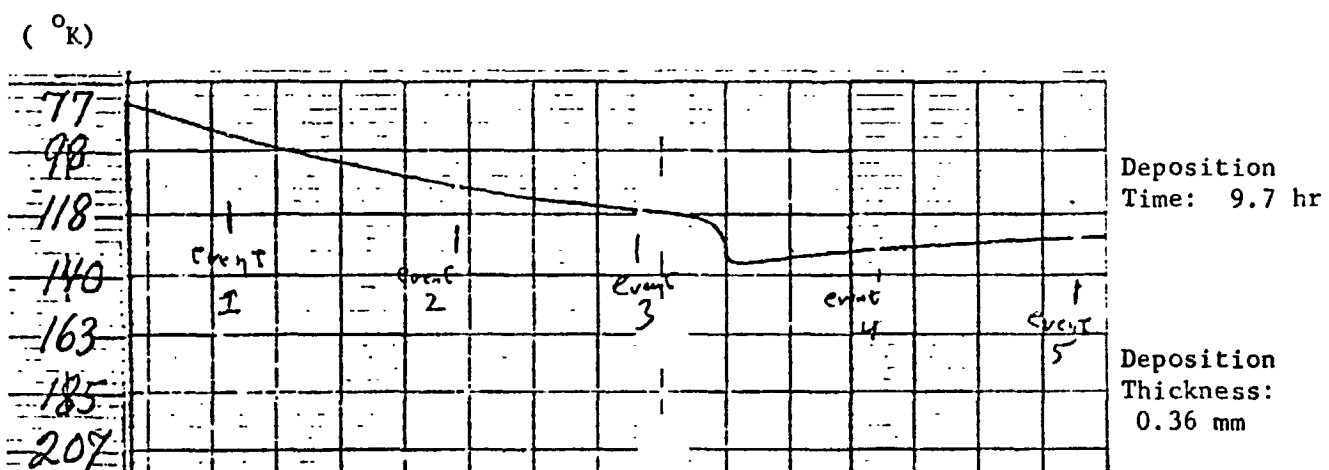Deposition
Thickness:
0.36 mm

Time (2.5 min/div)

Figure 58

Temperature History of Amorphous H_2O
Depositions During Warm-Up

nitrogen temperature, but found a density value of 1.2 g cm^{-3} when
the ice was formed at $10^{o}K$.

Note the consistency of all the three depositions.

3.4.2.3.2 <u>Water Ice and Ammonia Deposition</u> - This deposition was
conducted in a similar manner as the ones above. The vapor supply, however,
was provided by ice in the form of frozen ammonia water (30% NH_3). The
results of the warm-up curve from this run are shown in Figure 59. One
can notice that the initial warm-up is similar to the warm-up curves
shown in Figure 58. The energy release, however, is distinctly different.
An abrupt change appears at $110^{o}K$ and a continuous energy release occurs
for an extended period of time before cooling sets in and the temperature
approaches the steady state condition. The appearance of the ice was very
similar to the depositions without ammonia with perhaps a trace of
milkiness evident. The density estimate for this deposition resulted in
a value of (0.7 $\pm$ 0.1) g cm^{-3}. Once again, however, ice on the fiber
created difficulties for the mass determination.

3.4.2.3.3 <u>Water Ice and Methane Deposition</u> - Clathrates are formed
under certain temperatures and pressures. In order to assure the formation
of a clathrate a methane pressure of between 0.5 and 1 torr was maintained
while the ice was deposited. The resulting deposition is shown in Figure 60.
The appearance was that of unglazed,fine, white porcelain. No energy
release was evident during warm-up. Unfortunately no reliable density
measurement could be obtained for this particular run, due to a severe ice
built-up on the fiber and the thermocouple wires, as is evident in the
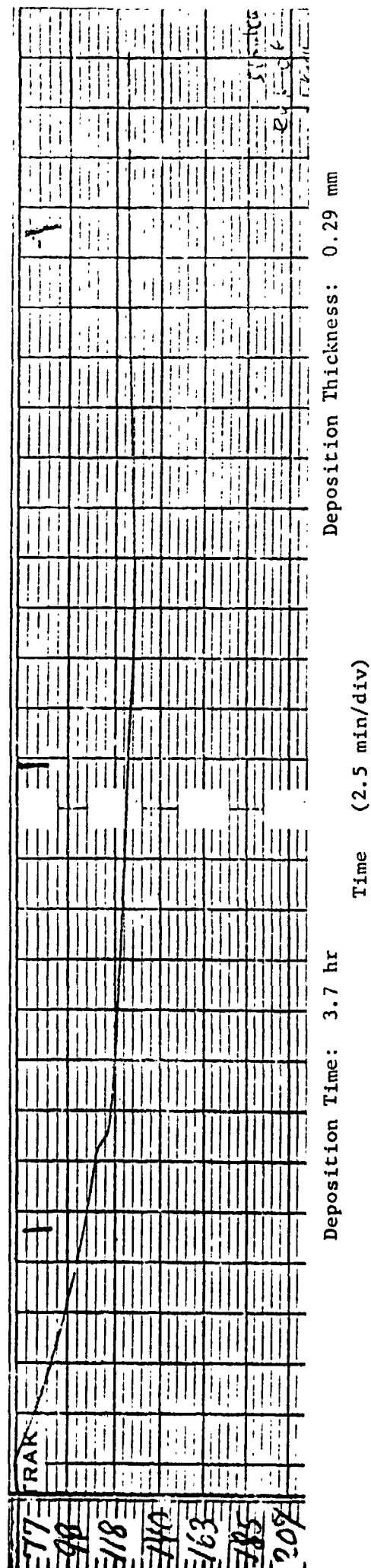
Deposition Time: 3.7 hr   Time   (2.5 min/div)   Deposition Thickness: 0.29 mm

Figure 59

Temperature History of NH_3 + H_2O
Deposition During Warm-Up

Figure 60 - Deposition of H_2O in the Presence of CH_4

photograph, Figure 60. It is interesting to note that there was no evidence of the formation nor the release of $100 \mu m$ size particles during the deposition phase or the subsequent warm-up period as has been reported by Delsemme (Ref. 3).

3.4.3 Concluding Remarks - The experiments reported above represent only a pilot investigation of properties of amorphous ices. The indications, however, are quite exciting. There is no doubt that energy is stored in the form of lattice disorder in the amorphous phase of water ice. It is somewhat of a surprise that the energy release was observed at $120^{\circ}K$ which is about $20^{\circ}K$ lower than is reported for the amorphous - cubic phase transition (Ref. 23). A convincing explanation for this discrepancy cannot be given at this time. However, in the rare articles available on the subject Dowell and Rinfret (Ref. 37) report a vitreous to cubic phase change at temperatures below $140^{\circ}K$. Their experiment, however, was performed at 5×10^{-3} torr. It is obvious that in this case the deposition took place in the presence of residual gases. Although the authors do not explain, one possibility is that impurities may have the effect of lowering the temperature where the phase transition takes place. Further evidence for this supposition may be seen in the ammonia run where a phase change apparently took place at $110^{\circ}K$, i.e $10^{\circ}K$ lower than without the ammonia. If this relationship can be confirmed by further experimentation, the impact on the comet model presented here is very profound. It would mean that comet activity can be initiated by this mechanism at much greater distances from the sun than was previously proposed. Furthermore it

demonstrates that the presence of other gases does not necessarily
prohibit the formation of an energy containing ice. Although at liquid
nitrogen temperatures a mixture of water with methane will always form a
clathrate with the available methane, this does not mean that other gases
will also form clathrates at this temperature. In fact, tne CO_2 clathrate
is not even stable at temperatures below 120°K (Ref. 32). Furthermore a
serious question can be raised in respect to the formation of clathrates
at very low temperatures (in the order of 10°K). Most likely there is
not sufficient surface mobility at these temperatures to provide the
activation energy for the formation of a crystalline lattice structure.
Therefore, the amorphous lattice is the one most likely to be generated
during a deposition at these temperatures. No claim is made that clathrates
with certain gases cannot form during the history of a comet when
temperature conditions are appropriate. It is only suggested that a
significant amount of the cometary ices, particularly those near the
surface which have accreted during the colder periods of the comet development,
are in the form of an amorphous ice, and that energy released during the
warming of these ices provides an internal energy source for comet activity.

Obviously the full development of the ideas presented in this section
on amorphous ice can only be realized when more experimental information
becomes available.

4.   ADDITIONAL APPLICATIONS - Ice Particles in Cirrus Clouds

The study of ice particles in this report is mainly concerned with
ice in space especially with applications to comets. However, the basic

physical insights which have been obtained during the course of this study could readily be applied to illuminate a long standing problem in cloud physics. The following study pertains to the interaction of cirrus ice particles with their environment and theoretically demonstrates a means by which a modification of the evaporation coefficient results in a cloud seeding potential.

4.1 <u>Introduction</u> - Numerous experiments have been conducted which show that ice particles from cirrus clouds can fall great distances in the earth's atmosphere even under subsaturated conditions (Ref. 33). This is of some importance to weather prediction since these falling ice particles can act as nucleation centers for lower supersaturated strata. A number of calculations using standard aerodynamic and meteorological equations to express fall velocities and energy and mass transport have failed to explain the observations (Ref. 33 and 34). In this report two terms which are usually neglected are closely scrutinized, namely the radiative heat transfer between the ice particle and its surrounding and the sublimation process as expressed by the evaporation coefficient. The conditions under which these contributions become important have been determined.

4.2 <u>Theory</u> - The behavior of falling ice particles is governed by the conservation of energy and mass. Accordingly

$$P_h + P_s + P_{rad} + P_{st} = 0 \qquad (24)$$

with the convention that these terms are positive when power is delivered to the ice particle. Here P_h represents the power delivered to the ice particle by diffusive heat transfer, P_s represents the power delivered (>0)

or removed (<0) by condensation or sublimation, P_{rad} is the net power transferred by radiation, and P_{st} pertains to the energy stored in the ice particle and released by a temperature change ($\dot{T}<0$). The conservation of mass requires that the rate of growth, $d\ell/dt$, of a surface element of the ice particle is proportional to the net molecular flux, j_m. Hence

$$\frac{d\ell}{dt} = \frac{j_m}{\rho} \qquad (25)$$

where ρ is the density of the active volume element of the ice particle.

The first term, P_h, in equation (24) can be expressed in the form

$$P_h/A = \langle j_h \rangle_s = \chi \langle gradT \rangle_s \qquad (26)$$

where A is the surface area of the ice particle, $\langle j_h \rangle_s$ is the heat flux at the surface, averaged over the total surface, χ is the thermal conductivity of air, and $\langle gradT \rangle_s$ is the thermal gradient in the air at the surface, averaged over the total particle surface.

The second term in the equation (24) can be written as

$$P_s/A = H \langle j_m \rangle_s = HD \langle gradc \rangle_s . \qquad (27)$$

Here H is the heat of sublimation, D is the diffusion constant of water vapor in air, $\langle j_m \rangle_s$ is the net molecular flux at the surface (see equation (25)) averaged over the total particle surface, and $\langle gradc \rangle_s$ is the averaged concentration gradient of water vapor at the particle surface.

The third term in equation (24), P_{rad} can be expressed as

$$P_{rad}/A = \int_0^\infty \left[\tfrac{1}{2}S(\lambda)\Gamma_1(\lambda) + \tfrac{1}{2}\{F(\lambda,T_e)+S'(\lambda)\}\Gamma_2(\lambda) - F(\lambda,T_s)\right] Q(\lambda,r',n^*)d\lambda \qquad (28)$$

Here $S(\lambda)$ is the radiation from the sun, $\Gamma_1(\lambda)$ is a filter factor which accounts for the attenuation of the sunlight on its way to the ice particle,

$F(\lambda, T_e)$ is the black body radiation for an earth surface temperature, T_e, $S'(\lambda)$ is the reflected radiation from the surface of the earth, while $\Gamma_2(\lambda)$ is the filter factor which tells how much of the radiation from the surface of the earth reaches the ice particle. This expression can be appropriately modified for a cloud cover between the cirrus level and the earth's surface. The term $F(\lambda, T_s)$ pertains to the black body radiation of surface temperature, T_s, of the ice particle. $Q(\lambda, r'n*)$, is the absorption and emission efficiency of the particle as a function of wavelength, λ, size factor, r', and complex index of refraction, $n*$. The explicit expressiones for the filter functions $\Gamma_1(\lambda)$ and $\Gamma_2(\lambda)$ and the absorption efficiency Q will not be given in this report (Ref. 35 and 16).

Finally, the last term in equation (24) can be presented in the form

$$P_{st}/A = - \frac{M}{A} \cdot c_{ice} \cdot \dot{T}_{ice} \qquad (29)$$

where M is the mass of the ice particle, c_{ice} is the specific heat of ice, and $\dot{T}_{ice}$ is the time derivative of a characteristic temperature of the ice particle. Assuming that for small ice particles internal temperature gradients can be neglected, $\dot{T}_{ice}$ can be replaced by the time derivative of the surface temperature.

$$\dot{T}_{ice} \approx \dot{T}_s \qquad (30)$$

The heat and mass transport in the vicinity of the ice particle is described by two basic differential equations. The diffusive heat transfer follows the equation

$$\dot{T} = \lambda \nabla^2 T \qquad (31)$$

where T is the temperature of the air and λ is the thermal diffusivity.
The diffusion of water vapor in the surrounding of the ice particle can
be described by the water vapor concentration, c, in the relation

$$\dot{c} = D \nabla^2 c \qquad (32)$$

The two equations (31) and (32), require the solution of a boundary
condition problem which is unattainable due to the complicated nature
of the processes involved. Nevertheless one and only one solution of
the problem exists and the solution of these two equations can be shown
to be closely related.

If T_a and c_a are the air temperature and water vapor concentration
of the surrounding air, and T_s and c_s are the surface temperature and
surface concentration of the water vapor, one can introduce into equations
(31) and (32) dimensionless variables T* and c* which have the effect that
the boundary conditions of both equations match. With

$$T^* = \frac{T - T_s}{T_a - T_s} \qquad (33)$$

$$c^* = \frac{c - c_s}{c_a - c_s} \qquad (34)$$

these equations become

$$\dot{T}^* = \lambda \nabla^2 T^* \qquad (35)$$

$$\dot{c}^* = D \nabla^2 c^* \qquad (36)$$

The diffusion coefficient, D, and the thermal diffusivity, λ, for water
vapor in air not only have the same dimensions but are also close in

their numerical value, as shown in Table 2. One can try to assess the influence of the difference of about 10% between the diffusion constant and the thermal diffusivity on the solution of equation (31) and (32). One can argue that the difference of the solution is largest when the Reynold's number is small, i. e. for laminar flow. But as the Reynold's number increases and the flow becomes turbulent the mixing action beyond the Prandtl-layer and the decreasing thickness of this layer will both cooperate to wipe out the difference between the two solutions.

Consequently, one can conclude that whatever the solutions of equations (35) and (36) may be, they are virtually identical. This leads to

$$\langle \mathrm{grad} T^* \rangle_s = \langle \mathrm{grad} c^* \rangle_s \geqslant 0 \qquad (37)$$

for

$$D/\lambda \approx 1 \qquad (38)$$

The definition of the Nusselt number, Nu, implies that

$$\langle \mathrm{grad} T^* \rangle_s = \frac{Nu}{\ell} \qquad (39)$$

where ℓ is a characteristic particle dimension. Therefore equations (26) and (27) become

$$P_h/A = \langle j_h \rangle_s = \chi (T_a - T_s) \langle \mathrm{grad} T^* \rangle_s \qquad (40)$$

and

$$P_s/A = H \langle j_m \rangle_s = HD(c_a - c_s) \langle \mathrm{grad} c^* \rangle_s \qquad (41)$$

Using the relation

$$\lambda c_p \rho = \chi \qquad (42)$$

where c_p is the specific heat of air at constant pressure and ρ is the density of air, equation (24) can be written in the form

$$c_p(T_a - T_s) + H \frac{D}{\lambda} (c_a - \theta_s) = - \frac{(P_{rad} + P_{st}) \ell}{A \lambda Nu} \qquad (43)$$

Table 2. Diffusion Coefficient and Thermal Diffusivity as a
Function of Altitude for a Temperature Profile

$T(h) = 303-6.49h$ $[^{o}K]$ h in $[km]$

h $[km]$	D $[cm^2sec^{-1}]$	λ $[cm^2sec^{-1}]$	D/λ
4	0.351	0.317	1.105
5	0.380	0.343	1.106
6	0.409	0.369	1.108
7	0.444	0.400	1.110
8	0.483	0.434	1.112
9	0.524	0.470	1.114
10	0.574	0.514	1.116

For a free falling ice particle the Nusselt number, Nu, is related to the Reynold's number, Re, by the equation

$$Nu = 0.37(Re)^{0.6} \tag{44}$$

The Reynold's number $Re(h,\ell)$ and the relative fall velocity $v(h,\ell)$ can be determined as a function of altitude, h, and characteristic particle dimension, ℓ, by the relations

$$C_D v^2 = \frac{4}{3} g \frac{\rho_{ice}}{\rho_{air}} \ell \tag{45}$$

$$Re = \frac{v \ell}{\nu} \tag{46}$$

and the empirical relation as found, for instance, in the AIP handbook

$$C_D = f(Re) \tag{47}$$

In those equations C_D is the drag coefficient, g is the gravitational acceleration, and ν is the kinematic viscosity of the air. For an atmosphere with a vertical velocity, v_v, the total particle velocity, v_t, becomes

$$v_t = v + v_v \tag{48}$$

Finally, the change in particle size can be expressed as

$$\frac{d\ell}{dt} = \frac{DNu}{\rho_{ice}} (c_a - c_s) \tag{49}$$

The system of equations (43) through (49) has only two unknowns: the surface temperature of the free falling ice particle, T_s, and the surface concentration, c_s. All the other terms are explicit functions of T_s. The relation between the surface concentration, c_s, and the surface temperature which is implicitly contained in the solutions of equations (35) and (36)

was lost when these two equations were used to form equation (43).

This relation will be developed next. For this purpose c_a and c_s are written as the product of a relative humidity and a saturation concentration, $C(T)$:

$$c_a = H_a C(T_a) \tag{50}$$

$$c_s = H_s C(T_s) \tag{51}$$

The flux rate ϕ in $[g \ cm^{-2} \ sec^{-1}]$ at which mass is leaving the surface of the ice particle is given by equations (26) and (27).

The mass flux rate, ψ, at which the water molecules condense on the surface of the ice particle is given by

$$\psi = H_s \phi \tag{52}$$

Consequently the total rate of mass transport is given by

$$\psi - \phi = \phi (H_s - 1) \tag{53}$$

The term $(\psi - \phi)$ is equivalent to the rate, $\langle j_m \rangle_s$, at which mass diffuses away from the surface. Therefore according to equations (39), (41) and (51) one obtains

$$\propto \phi_{th} (H_s - 1) = \frac{DNu}{\ell} \left[c_a - H_s C(T_s) \right] \tag{54}$$

or

$$H_s = \frac{c_0 + c_a}{c_0 + C(T_s)} \tag{55}$$

with

$$c_0 = \frac{\propto \phi_{th} \ell}{DNu} \ [g \ cm^{-3}] \tag{56}$$

Equation (55) relates the surface humidity to the water vapor concentration of the air, c_a, the saturation concentration $C(T_s)$ and a dynamic concentration c_o which is a combination of water vapor generation and transport terms. Accordingly $H_s=1$ for $c_a=C(T_s)$ as expected. For $c_a \neq C(T_s)$, however, the surface humidity H_s differs from unity, the deviation depending upon the dynamic concentration c_o. When the vapor transport is the bottleneck, i.e. if

$$c_o \gg c_a, \ C(T_s) \text{ then } H_s \approx 1 \qquad (57)$$

If the transport capability exceeds the vapor generation, i.e. if

$$c_o \ll c_a, \ C(T_s) \text{ then } c_a \approx c_s \qquad (58)$$

Equation (48) shows that the evaporation coefficient, α, influences directly the dynamic concentration c_o. Its influence is reciprocal to that of the transport terms, D and Nu.

The system of equations, developed above, constitutes a description of the interactions of a free falling ice particle with its surroundings which are characterized by the temperature and humidity profile, the vertical components of the air velocity, and by the radiational energy sources. If these parameters are given, the fate of a falling ice particle can be readily computed.

4.3 <u>Computations and Results</u> - The system of equations given in the previous section has been implemented into a computer program where the temperature and humidity data of Braham (Ref. 33) have been used as input. His observations suggest that ice particles can fall considerable distances in subsaturated air. Previous calculations have suggested that

under his described conditions the ice particles would never reach the
collection level. These treatments, however, have lacked completeness.
In the present calculation the parameters are optimized to give falling
ice particles the greatest chance of survival to reach the collection
level, which makes this a best case analysis. Therefore spherical ice
particles of maximum density (0.92 g cm^{-3}) have been chosen for the
calculations. This has also the obvious advantage that the absorption
efficiencies for the radiational term can be calculated with a minimum
of computational effort (r'=r, ℓ=2r).

As a typical case ice spheres with a radius of 100 μm are released
at a height of 9.14 km as a starting point. In Figure 61 the radius is
shown as a function of altitude under several radiational surroundings
and for a number of air humidities, H_a. The curves which all start at
the same point either end at r=0 (death by sublimation) or end when the
particle melts. For the purpose of the present investigation a simplified
treatment of the radiational surroun ng seems justified. In this
treatment the ice particle is interacting with a black body radiation of
wall temperature, T_W. The impact of the radiational energy exchange on
the particle descent can then be readily assessed: the maximum influence
of the radiational term to increase the lifetime of the ice particle
is reached when the particle radiates into a surrounding at absolute zero.

Even with those optimizations one can note from the computational
results in Figure 61 that for a humidity of 27 percent as quoted by
Braham an ice particle of 100 μm radius is not able to reach the collection
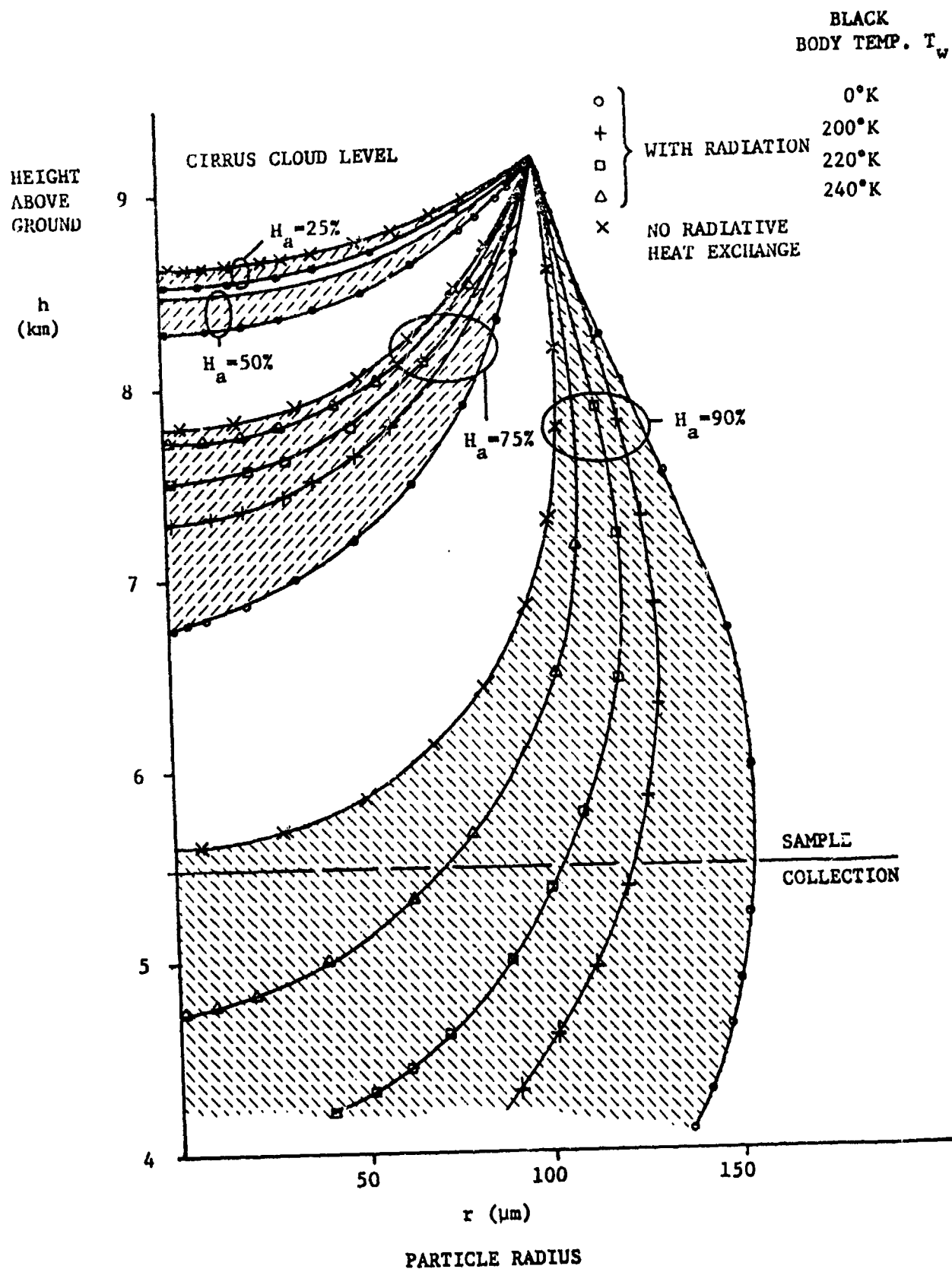
Figure 61.   Free Fall of Spherical Ice Particles in the Atmosphere
              for Different Humidities H_a and Radiation Backgrounds.
              Starting Height: 9.14 km, Starting Radius: 100 μm

level unless the humidity during these measurements was considerably

higher than the quoted value. The influence of the radiation term

becomes clearly increasingly significant as the concentration difference

between the surface and the air decreases. This concentration difference

becomes small only under two circumstances:

1) The humidity of the air is high.

2) The evaporation coefficient,α, is sufficiently small as can be concluded from equations (56) and (58).

The results in Figure 61 have been calculated using the data obtained

in section (3.2.2.1.4) but α is not small enough to sufficiently reduce

the concentration differential which is the prerequisite for large fall

distances. Even when other values for α, typically around Delaney's

value (Ref. 36) of 0.014, are used, neglecting even the measured strong

temperature dependence of α, the results do not begin to be affected

unless α drops below 10^{-3}.

Since down drafts have an influence on the particle motion the

fate of ice particles has been calculated for different down draft

velocities. (See equation (48)). Although it is realized that down

drafts upset the temperature profile the calculations were carried out

for lack of information with the same temperature profile as was used

in the previous calculations and with a constant value for the relative

humidity of $H_a = 27\%$ as reported by Braham. As before, the calculations

were optimized in favor of a large particle lifetime by using spherical

ice particles of density 0.92 g cm^{-3} and having them radiate into a

black body environment at absolute zero. The results of these calculations

are shown in Table 3. For a number of down drafts the height is

calculated where ice particles which start out at a cirrus cloud level

of 9.14 km with a radius of $100 \mu m$ have shrunk to a radius of $20 \mu m$ and

$10 \mu m$. In Table 3 the altitudes close to the collection level of 5.5 km

have been underlined, corresponding to down drafts of 3.5 msec^{-1} and

2.75 msec^{-1}. The radii, $20 \mu m$ and $10 \mu m$ have been slected for these

calculations because the majority of ice particles collected during

Braham's experiment fell into this size range. One can therefore conclude

that a down draft of about

$$v_v = 3 \text{ msec}^{-1} \qquad (59)$$

is required to insure the existence of ice particles with radii in the

range between $10 \mu m$ and $20 \mu m$ at the collection level. The existence

of such a severe down draft over the total path of the falling ice particle

seems unlikely from Braham's description of the weather situation in

particular, since similar results were obtained at a different date.

Furthermore the temperature profile measured by the sample collecting

airplane during the experiment also shows no indication of the existence

of such a down draft.

4.4 <u>Conclusion</u> - In order to explain Braham's collection data one

is left with only two possibilities: either the reporte humidity is

totally erroneous or the evaporation coefficient for the collected cirrus

ice particles is considerably less than that measured for pure ice.

The implication in the second case is that the surfaces of these

cirrus ice particles were modified by environmental factors which reduced

Table 3

Altitude as a function of down draft, v_v, reached by free falling spherical ice particles, of density 0.92 g cm^{-3} when their radius has decreased to 20 μm and 10 μm from a radius of 100 μm at a height of 9.14 km. The humidity is 27% and the temperature profile is $T(h) = 302-6.49$ h $[^\circ K]$, h in $[km]$.

DOWN DRAFT	ALTITUDE IN km FOR PARTICLE RADIUS	
v_v msec^{-1}	20 μm	10 μm
1.0	7.3	7.0
2.7	6.0	5.5
2.9	5.9	5.4
3.0	5.8	5.4
3.7	5.5	5.0
5.0	4.9	4.3
10.0	3.4	2.6

the sublimation rate. Such a possibility seems not too far fetched when one realizes that just one monolayer of a sublimation impeding substance on the ice particle surface can have a pronounced effect. Due to the seeding potential of cirrus ice crystals, the effect of natural, artificial and pollution caused substances on the evaporation coefficient should be throughly investigated. The implications for weather prediction, wheather modification and possible climatic changes cannot be ignored.

5. ACKNOWLEDGMENTS

6.   REFERENCES

1.   Cohen, M., _Publications of the Astronomical Society of the Pacific_, V. 87, p. 500, 1975.

2.   Whipple, F. L., _Astrophys. J._, V. 111, p. 375, 1950.

3.   Delsemme, A. H., and Wenger, A., _Plant. and Space Sci._, V, 18, p. 709, 1970.

4.   Rupprecht, G., and Patashnick, H., "The Evaporation Coefficient of Water Ice", (To be published).

5.   Patashnick, H., and Rupprecht, G., _Astrophys. J._, V. 197, p. L79, 1975.

6.   Patashnick, H., and Rupprecht, G., _Icarus_, (in print).

7.   Patashnick, H., Rupprecht, G., and Schuerman, D. W., _Nature_, V. 250, p. 313, 1974.

8.   Rupprecht, G., and Patashnick, H., "Free Falling Ice Particles in the Earth's Atmosphere", (to be published).

9.   Patashnick, H., and Rupprecht, G., "Sublimation of Ice Particles in Space", Skylab Program Payload Integration Technical Report, ED-2002-1654, 1973.

10.   Patashnick, H., and Hemenway, C. L., _Rev. Sci. Inst._, V. 40, p. 1008, 1969.

11.   Davy, J. G., and Somorjai, G. A., _J. Chem. Phys._, V. 55, p. 3624, 1971.

12.   Mason, B. J., and Maybank, J , _Quart. J. R. Met. Soc._, V. 86, p. 176, 1960.

13.   Cheng, R. J., _Science_, V. 170, p. 1395, 1970.

14.   Irvine, W. M., and Pollack, J. B., _Icarus_, V. 8, p. 324, 1968.

15.   Bertie, J. E., Labbe, H. J., and Whalley, E., _J. Chem. Phys._, V. 50, p. 4501, 1969.

16.   van de Hulst, H. C., _Light Scattering by Small Particles_, (New York, Wiley), 1957.

17.   Plass, G. N., _Appl. Optics_, V. 5, p. 279, 1966.

18. Rupprecht, G., Phys. Rev. Letters, V. 12, p. 580, 1964.

19. Delsemme, A. H., and Miller, D. C., Planet, Space Sci., V. 19, p. 1229, 1971.

20. Jenkins, E. B., and Wingert, D. W., Astrophys. J., V. 174, p. 697, 1972.

21. Code, A. D., Houck, T. E., and Lillie, C. F., The Scientific Results from the Orbiting Astronomical Observatory (OAO-2), NASA SP-310, p. 109, 1972.

22. Venkatesh, C. G., Rice, S. A., and Narten, A. H., Science, V. 186, p. 927, 1974.

23. Ghormley, F. A., J. Chem. Phys., V. 46, p. 1321, 1966.

24. McMillan, F. A., and Los, S. C., Nature, V. 206, p. 806, 1965.

25. Delsemme, A. H., and Wenger, A., Science, V. 167, p. 44, 1970.

26. Whitney, C., Astrophys. J., V. 122, p. 190, 1955.

27. Pittich, E. M., "Splitting and Sudden Outbursts of Comets as Indicators of Nongravitational Effects", (Forty-fifth IAU Symposium, Leningrad), p. 283, (Reidel, Dordrecht), 1972.

28. Watson, K., and Murray, B. C., and Brown, H., Icarus, V. 1, p. 317, 1963.

29. Sommerfeld, A., Partial Differential Equations, p. 68, (Academic Press, New York), 1949.

30. Brydges, W. T., and Kozlowski, T. R., Corning Glass Works, Corning, New York, (private communication) 1974.

31. Donn, B., and Urey, H. C., Astrophys. J., V. 123, p. 339, 1956.

32. Miller, S. L., and Smythe, W. D., Science, V. 170, p. 531, 1970.

33. Braham, R. R., J. Appl. Meteorol., V. 6, p. 1053, 1967.

34. Hall, W. D., and Pruppacher, H. R., "A Theoretical and Wind Tunnel Study on the Survival of Ice Crystals Falling from Cirrus Clouds in Subsaturated Air", Conference on Cloud Physics, Tucson, Arizona, 1974.

35. Kundratlev, K., "Radiation Characteristics of the Atmosphere and the Earth's Surface", Gidrometerologicheskoe Press, Leningrad, 1969.

36. Delaney, L. J., Houston, R. W., and Eagleton, L. C., _Chem. Engr. Sci._, V. 19, p. 105, 1964.

37. Dowell, L. C., and Rinfret, A. P., _Nature_, V. 188, p. 1144, 1960.